

PhD Thesis

**Fluctuations and non-equilibrium  
phenomena in strongly-correlated ultracold  
atoms**

Kazuma Nagao

*Yukawa Institute for Theoretical Physics,  
Kyoto University*

January, 2019

© Copyright by  
Kazuma Nagao  
2019

# Contents

|          |   |           |
|----------|---|-----------|
| <b>1</b> | <b>Introduction</b>   | <b>8</b>  |
| 1.1      | Backgrounds . . . . .   | 8         |
| 1.2      | Motivation . . . . .  | 10        |
| 1.3      | Outline of this thesis . . . . .  | 11        |
| <b>2</b> | <b>Ultracold Bose gases in optical lattices</b>                         | <b>13</b> |
| 2.1      | Optical-lattice potentials . . . . .                                    | 13        |
| 2.2      | Bose–Hubbard models . . . . .   | 14        |
| 2.3      | Superfluid-Mott-insulator quantum phase transitions . . . . .           | 16        |
| 2.3.1    | Mean-field theory of the superfluid-Mott-insulator transition . . . . . | 18        |
| 2.3.2    | Field-theoretical description of the quantum phase transition . . . . . | 19        |
| 2.4      | Higgs and Nambu–Goldstone modes . . . . .                               | 21        |
| 2.5      | Hilbert-space truncation and effective pseudospin-1 models . . . . .    | 23        |
| 2.5.1    | Reduced Hilbert space in strongly-correlated regimes . . . . .          | 24        |
| 2.5.2    | Effective pseudospin-1 model at a high-filling limit . . . . .          | 25        |
| 2.5.3    | Effective pseudospin-1 model at low-filling rates . . . . .             | 26        |
| 2.5.4    | Gutzwiller’s variational ansatz in the reduced Hilbert space . . . . .  | 26        |
| 2.5.5    | Elementary excitations around the Gutzwiller’s wave function . . . . .  | 28        |
| <b>3</b> | <b>Phase space methods for quantum dynamics</b>                         | <b>32</b> |
| 3.1      | Introduction . . . . .  | 32        |
| 3.2      | Wigner representation of Bose fields . . . . .                          | 35        |
| 3.2.1    | Coherent-state phase space representation . . . . .                     | 35        |
| 3.2.2    | Weyl symbols and Weyl ordering . . . . .                                | 36        |
| 3.2.3    | Moyal products and Bopp operators . . . . .                             | 38        |
| 3.2.4    | Displacement operator expansion . . . . .                               | 39        |
| 3.2.5    | Wigner functions . . . . .  | 42        |

|          |  |           |
|----------|--|-----------|
| 3.3      | Quantum dynamics in the coherent-state phase space . . . . .                   | 45        |
| 3.3.1    | Truncated-Wigner approximation . . . . .                                       | 46        |
| 3.3.2    | Semiclassical approximation in phase-space path integrals . . . . .            | 47        |
| <b>4</b> | <b>Response of the Higgs mode in a three dimensional optical lattice</b>       | <b>51</b> |
| 4.1      | Time-dependent external perturbations and linear responses . . . . .           | 51        |
| 4.1.1    | Modulations of the kinetic energy . . . . .                                    | 52        |
| 4.1.2    | Modulations of the onsite-interaction energy . . . . .                         | 52        |
| 4.2      | Interactions between collective modes . . . . .                                | 53        |
| 4.2.1    | Fluctuations from the mean-field ground state . . . . .                        | 54        |
| 4.2.2    | Holstein–Primakoff expansion . . . . .   | 55        |
| 4.2.3    | Bogoliubov transformation . . . . .  | 57        |
| 4.2.4    | Normal ordering . . . . .  | 59        |
| 4.3      | Linear response analysis . . . . .   | 61        |
| 4.3.1    | Response functions . . . . .   | 61        |
| 4.3.2    | Imaginary-time Green’s functions . . . . .                                     | 62        |
| 4.3.3    | Self-energy functions . . . . .  | 64        |
| 4.4      | Results . . . . .  | 68        |
| 4.4.1    | Response functions in the uniform system . . . . .                             | 68        |
| 4.4.2    | Effects of a trapping potential . . . . .                                      | 71        |
| 4.4.3    | Response functions at $R = R_{TF}$ . . . . .                                   | 72        |
| 4.4.4    | Responses around the trapping center . . . . .                                 | 73        |
| 4.5      | Summary of this chapter . . . . .  | 75        |
| <b>5</b> | <b>Semiclassical quench dynamics of Bose gases in optical lattices</b>         | <b>76</b> |
| 5.1      | Semiclassical dynamics of the Bose–Hubbard model . . . . .                     | 76        |
| 5.2      | Redistribution of the kinetic and interaction energies . . . . .               | 77        |
| 5.2.1    | Experimental setup . . . . .   | 77        |
| 5.2.2    | Application of TWA to the quench experiment . . . . .                          | 78        |
| 5.2.3    | TWA versus experimental results . . . . .                                      | 82        |
| 5.3      | Spatial-correlation spreading after a sudden quench . . . . .                  | 83        |
| 5.3.1    | Sudden quench from a coherent state . . . . .                                  | 84        |
| 5.3.2    | Quench from a Mott-insulator state across a quantum phase transition . . . . . | 89        |
| 5.4      | Summary of this chapter . . . . .  | 93        |
| <b>6</b> | <b>Conclusions and outlooks</b>  | <b>94</b> |

---

|          |   |           |
|----------|---|-----------|
| <b>A</b> | <b>Energy absorption due to the onsite-interaction strength modulations</b> | <b>97</b> |
| <b>B</b> | <b>Coefficients in the effective model</b>                                  | <b>99</b> |

# Abstract

A system of ultracold atoms in an optical lattice has offered a promising analog-quantum simulator for investigating quantum many-body systems encountered in condensed matter physics. The high-controllability and unique experimental tools allow one to detect various dynamical properties of many-body systems with high accuracy. For instance, the lattice-amplitude modulation technique and the quantum-gas microscopy can be used to perform a high-sensitive spectroscopy of low-energy excitations of strongly-interacting systems and characterize the collective behaviors within a linear-response regime. Moreover, the ultracold-gas quantum simulator has a lot of potential to gain access to far-from-equilibrium quantum many-body dynamics, which is difficult to access by currently-available numerical techniques. Especially, particular attention has been devoted to quantum quench dynamics, and several intriguing non-equilibrium phenomena have been observed, such as relaxation dynamics of local quantities or effective light-cone dynamics of spatial correlation functions in Bose gases trapped by an optical lattice.

In this thesis, motivated by such experimental developments, we analyze near- and far-from-equilibrium dynamics of ultracold Bose gases in optical lattices. First, we examine the experimental visibility of the Higgs or amplitude mode of strongly-interacting superfluid Bose gases near the Mott-insulator transition. This work is motivated by an experiment at the Max-Planck institute associated with the detection of the Higgs mode in a two-dimensional optical lattice. Although this experiment has partially captured a characteristic onset of the Higgs mode, a well-defined resonance peak of this mode has not been detected. Moreover, several theoretical calculations stimulated by this experiment have argued that the Higgs mode at two dimensions strongly attenuates due to the combined effects of the quantum and thermal fluctuations and the spatial inhomogeneity of the trapping potential. In this sense, the existence of a stable Higgs mode in the cold-atomic systems remains to be an open issue. In this thesis, aiming to detect a visible Higgs mode in experiments, we study responses of the Higgs mode in a three-dimensional optical lattice, where the fluctuations are relatively small compared with two-dimensional systems. Combing the effective pseudospin-1 mapping of the Bose–Hubbard model and the field-theoretical linear-response theory, we calculate some response functions, which can be directly measured in experiments, taking

into account a leading-order quantum and thermal fluctuation correction. It is shown that if the system is uniform, the Higgs mode can exist as a sharp resonance peak even at typical experimental temperatures. Furthermore, we study the non-uniform trap effect on the uniform response functions at unit filling within the local-density approximation. We suggest that if we partially modulate condensates around the trap center, at which the atomic density is tuned to unity, the Higgs mode can be detected as a sharp resonance even at typical temperatures.

Next, motivated by a recent experiment at Kyoto University, we analyze far-from equilibrium dynamics of Bose gases in a cubic optical lattice. In the experiment, redistribution dynamics of the kinetic and onsite-interaction energies has been observed after a sudden quantum quench from a singly-occupied Mott-insulator state into a weakly-interacting regime. Although some fundamental results have been reported, any quantitative approach that can recover the experimental results at three dimensions has not been established thus far. In this thesis, aiming to simulate the redistribution dynamics quantitatively, we employ the truncated-Wigner approximation (TWA), which systematically yields a leading-order correction due to fluctuations to the mean-field dynamics. It is demonstrated that the TWA results coincide well with the experimental data with no fitting parameter.

As a further application of the TWA, we also study spatial spreading of equal-time correlations in the two-dimensional Bose–Hubbard model. So far, the correlation spreading has been studied especially in one-dimensional systems due to the simplicity. Recently, there are several experimental and theoretical progresses associated with the correlation spreading in two-dimensional systems. However, the quantitative properties are less understood compared with the one-dimensional cases due to the limitation of quantitative computational tools. In this thesis, for the two-dimensional Bose–Hubbard model at a large filling factor, we analyze the time evolution of a density-density correlation function at equal time by starting with either a coherent state or a Mott-insulator state. We find that when the system is initially prepared in a coherent state, a mean propagation velocity of a wave packet in the correlation function strongly depends on the final interaction. In contrast, when the system is initially in a Mott-insulator state, a wave packet in the correlation function propagates with a nearly constant velocity with respect to the final interaction.

# Acknowledgement

First of all, I would like to express my appreciation to my research advisor, Prof. Ippei Danshita for supervising my research activities, suggesting many ideas and projects, encouraging me, and offering many opportunities to visit abroad during my five-years graduate course in Yukawa Institute for Theoretical Physics (YITP). I also wish to express my gratitude to Prof. Keisuke Totsuka for supervising my graduated student life at YITP during five years and giving a lot of advice on writing of this thesis. Without their supports and advice, this thesis could not be finished.

I would like to thank Prof. Yoshiro Takahashi for collaborating with several projects, offering a research assistant position and financial supports, and fruitful discussions about experiments of cold atoms. I would also like to thank Prof. Anatoli Polkovnikov for giving opportunities to visit his group at Boston University, suggesting joint projects associated with the truncated-Wigner approximation, encouraging me, and many helpful discussions and comments on my studies. Furthermore, I am grateful to my collaborators of various research projects in Japan. Especially, I would like to thank Prof. Yosuke Takasu, Dr. Masaya Kunimi, Dr. Shimpei Goto, Prof. Kenichi Kasamatsu, and Mr. Yusuke Ozaki for the collaborations, sharing unpublished data, and making fruitful discussions. These great experiences were really helpful to improve my research skills and complete this thesis.

I would like to thank Prof. Shunji Tsuchiya, Prof. Muneto Nitta, Prof. Tetsuro Nikuni, Prof. Carlos Sá de Melo, Prof. Ludwig Mathey, Prof. Shuta Nakajima, Prof. Daisuke Yamamoto, Dr. Kazuya Fujimoto, Dr. Adam Sajna, Dr. Shainen Davidson, Dr. Dries Sels, and Mr. Jonathan Wertz for fruitful discussions and useful comments on my studies. I would also like to thank Prof. Masatoshi Sato, Prof. Ken Shiozaki, and postdoctoral members of the Condensed-Matter-Physics Group at YITP for asking useful questions and comments in my talks at the weekly seminar. I also thank current and past YITP members, especially, Dr. Koudai Sugimoto, Dr. Kiyoshi Kanazawa, Dr. Kazuya Shinjo, Dr. Tomohiko Sano, Dr. Satoshi Takada, Dr. Takumi Ohta, Dr. Hidekazu Tsukiji, Mr. Kazuhiko Tanimoto, Mr. Yukihisa Imamura, Mr. Yuki Kamiya, and Mr. Takumi Bessho for making my student life enjoyable. Finally, I am grateful to my parents and my little brother.

# Publication List

This thesis is based on the following two publications:

1. Kazuma Nagao, Masaya Kunimi, Yosuke Takasu, Yoshiro Takahashi, and Ippei Danshita, *Semiclassical quench dynamics of Bose gases in optical lattices*, to be published in Physical Review A.
2. Kazuma Nagao, Yoshiro Takahashi, and Ippei Danshita, *Response of the Higgs amplitude mode of superfluid Bose gases in a three-dimensional optical lattice*, Physical Review A **97**, 043628 (2018).

The following papers are not included in this thesis:

1. Kazuma Nagao, Yosuke Takasu, Yoshiro Takahashi, and Ippei Danshita, in preparation, to be submitted in 2019.
2. Yosuke Takasu, Tomoya Yagami, Hiroto Asaka, Yoshiaki Fukushima, Kazuma Nagao, Shimpei Goto, Ippei Danshita, and Yoshiro Takahashi, in preparation, to be submitted in 2019.
3. Kazuma Nagao and Ippei Danshita, *Damping of the Higgs and Nambu–Goldstone modes of superfluid Bose gases at finite temperatures*, Progress of Theoretical and Experimental Physics **2016**, 063I01 (2016).

# Chapter 1

## Introduction

### 1.1 Backgrounds

A system of ultracold atoms in an optical lattice has offered a promising analog quantum simulator for studying quantum many-body systems encountered in condensed matter physics [1–7]. Loading degenerate Bose or Fermi atoms into optical-lattice potentials with a sufficient depth, a large variety of clean Hubbard-type models is successfully realized within the tight-binding approximation [1–7]. For instance, degenerate rubidium atoms ( $^{87}\text{Rb}$ ) tightly trapped by a cubic optical lattice are described by the three-dimensional (3D) Bose–Hubbard model [1, 2]. One of the most important properties of such an artificial system is the high controllability of the microscopic parameters for particles: the interactions (over the hopping amplitude) between atoms can be controlled from weakly to strongly interacting regimes through tuning the laser intensity of lattice [1, 2] or utilizing the Feshbach resonance [8]. So far, the performance of the ultracold-gas quantum simulator has been validated by direct comparisons with quasi-exact numerical simulations on classical computers [9–13] and has attracted a lot of attention from both of theoretical and experimental research areas.

In addition to the advantageous feature of the system itself, there are various detection techniques of quantum many-body states of an ensemble of cold atoms, such as the time-of-flight imaging and the quantum-gas microscopy [2, 6, 7, 14]. Especially, these techniques can be combined with some spectroscopic methods to identify low-energy excitations or spectral functions near equilibrium. The time-of-flight imaging has been used to characterize excitation spectra of degenerate gases combining with the radio-frequency spectroscopy [15], lattice shaking technique [16, 17], and standard Bragg spectroscopy [18]. More recently, the quantum-gas microscopy has been applied to detect an energy absorption after a lattice-amplitude modulation in strongly-interacting bosons in a two-dimensional (2D) lattice [19]. The microscope technique allows one to measure a temperature increase caused by the lattice modulations with high sensitivity. Thanks

to this advantage, the experiment [19] has been able to achieve a linear-response regime in which the modulation amplitude is much smaller compared with the previous studies [16, 17]. In the experiment [19], Endres and coworkers have utilized this spectroscopy for exploring the Higgs mode, which is a characteristic excitation mode in the strongly-interacting superfluid state close to the quantum phase transition, and obtained some prominent results of the spectral properties.

The ultracold-gas system is suited to studying real-time dynamics of quantum systems because it is decoupled with an external environment and has a relatively long relaxation time compared with the solid-state systems [20]. Thus, the system has a lot of potential to gain access to far-from-equilibrium quantum many-body dynamics [21, 22], which is in general impossible to simulate with currently available numerical methods on classical computers due to the exponential growth of the Hilbert-space dimension with system size and the minus-sign problem in quantum Monte Carlo simulations. Remarkably, the direct comparison with numerical simulations by the time-dependent density matrix renormalization group (t-DMRG) at one dimension (1D) in Ref. [11] has demonstrated that the quantum simulator can provide accurate data even in a long-time region, where the t-DMRG fails. This result has strongly stimulated developing new numerical methods for long-time dynamics instead of the previous t-DMRG approach, such as the density-matrix truncation (DMT) theory [23] and the time-dependent variational principle (TDVP) based on the matrix product state (MPS) [24].

Among diverse quantum many-body dynamics, particular attention has been devoted to quantum quench dynamics, which arises after a sudden and substantial change of parameters in the Hamiltonian [11, 12, 21, 22, 25–32]. In Ref. [11], Trotzky and coworkers have investigated relaxation dynamics of Bose gases in a 1D optical lattice starting from a simple density pattern and detected that the local density relaxes into a steady value within an experimental timescale. In Ref. [12], Cheneau and coworkers have observed an effective light-cone dynamics of an equal-time correlation function in a 1D optical lattice and demonstrated that in the strongly interacting region the propagation speed is bounded by the maximum group velocity of particle-hole excitations. In recent years, some experimental groups have explored far-from-equilibrium dynamics of high-dimensional Bose–Hubbard systems quenched from typical quantum states [33–36]. The Max-Planck institute group has explored the Kibble–Zurek dynamics after a finite-time quench across the quantum phase transition from the Mott-insulator (disorder) to superfluid (order) phases in the one-, two-, and, three-dimensional Bose–Hubbard models [33, 34]. On the other hand, the experimental group of Kyoto University has observed redistribution dynamics of kinetic and onsite-interaction energies of Bose gases in a cubic optical lattice after a rapid quench of the lattice depth from a strongly-interacting singly-occupied Mott insulator state into a weakly-interacting parameter region [35, 36].

## 1.2 Motivation

Motivated by these experimental developments and prominent results, in this thesis, we present theoretical analyses of near- and far-from-equilibrium dynamics of ultracold Bose gases in optical lattices. In the first part of this thesis, motivated by the experiment [19] in the Max-Planck institute, we examine the stability and detectability (or visibility) of the Higgs mode in the ultracold-gas systems. Theoretical calculations [37–45] stimulated by the same experiment have claimed that the Higgs mode at two dimensions strongly attenuates due to the combined effects of the quantum and thermal fluctuations and the spatial inhomogeneity of the trapping potential. Indeed, in Ref. [19], the measured response, which is a function of the modulation frequency of the lattice depth, exhibits a broad continuum above a threshold frequency rather than a sharp peak although the frequency coincides well with the Higgs gap, which is calculated theoretically. In this sense, the existence of a stable Higgs mode in the cold-atomic systems remains to be an open issue. This thesis presents another way towards a stable Higgs mode: if we consider a 3D optical lattice rather than 2D and perturb a partial condensate around the center of the trap, at which the density is tuned to unity as in Ref. [19], we can observe a sufficiently-stable Higgs mode in the corresponding response function even at typical temperatures of experiments. Our theoretical approach, which is a generalization of a finite-temperature Green’s function theory developed by the current author and Danshita previously [46], deals with quantum and thermal fluctuation effects within a leading 1-loop order. Combined with this field-theoretical method and the local density approximation, we study non-uniform confinement effects on uniform response functions. Furthermore, to discuss responses of the Higgs mode, we formulate linear-response functions to two external perturbations, i.e., the standard lattice-amplitude modulation and an onsite-interaction intensity modulation, respectively. In particular, the latter scheme is first considered by our work in the context of exploring the Higgs mode.

In the second part, motivated by the experiment [36] at Kyoto University, we investigate far-from-equilibrium quantum-quench dynamics of Bose gases in higher-dimensional optical lattices than 1D. Takasu and coworkers reported that the kinetic and interaction energies evolve into (transient) steady values for an early time immediately after ending of the ramp-down process of the lattice depth from the Mott-insulator state. Moreover, the experimental results have remarkably shown that the sum of these energies conserves at early times reflecting the isolation of the atomic ensemble. An immediate usage of such fundamental results is to examine or develop numerical methods for computing quantum many-body dynamics by taking them as an accurate reference. Nevertheless, any quantitative approach that can recover the experimental results at three dimensions has not been established thus far. In this thesis, aiming to simulate the

energy-redistribution dynamics quantitatively, we adopt a semiclassical approximation formulated by a phase-space representation of quantum systems, namely, the truncated-Wigner approximation (TWA), which systematically provides a leading-order correction of fluctuations to the mean-field dynamics [47–49]. This method is formulated from a quantum-to-classical mapping that computing the quantum average of an operator is replaced with a classical problem, where we solve Gross–Pitaevskii equations of classical Bose fields with *random* initial conditions sampled from an initial Wigner function (some advantages of this method will be explained in a later chapter). In this thesis, generalizing the previous TWA techniques [27,50,51] developed for quantum quenches starting from a largely-occupied Mott-insulator state, we numerically simulate the redistribution dynamics of the kinetic and interaction energies in the 3D system starting from a singly-occupied insulator state. Comparing the semiclassical and experimental results directly, it is demonstrated that the TWA lines agree well with the experimental data with no fitting parameter.

As a further application of the TWA, we also study spreading dynamics of non-local correlation functions after a sudden quench in Bose gases trapped by a 2D optical lattice. This application is motivated by experimental and theoretical works in ultracold neutral atoms, trapped ions, and interacting spin systems [12,52–59]. Thus far, the correlation spreading and the relationship with the Lieb–Robinson bound [60], which gives an upper bound of information propagation over space, have been studied with focusing on the 1D systems. At a viewpoint from the theoretical side, this is due to the limitation of currently-available tools to simulate dynamics of non-local correlations. More recently, spreading of spatial correlations at two dimensions has been explored by some works [35,36,61–63], whereas their quantitative properties are, however, less understood compared with the 1D case. In this thesis, within the semiclassical regime of the 2D Bose–Hubbard model, we analyze the time evolution of a density-density correlation function at equal time by starting with either a coherent state or a Mott-insulator state. We find that when the system is initially prepared in a coherent state, a mean propagation velocity of a wave packet in the correlation function strongly depends on the final interaction. In contrast, when the system is initially in a Mott-insulator state, a wave packet in the correlation function propagates with a nearly constant velocity with respect to the final interaction.

### 1.3 Outline of this thesis

This thesis is organized as follows: In Chap. 2, we review ultracold Bose gases trapped by optical lattice potentials. There, we derive the single-band Bose–Hubbard model within the tight-binding approximation. After that, we summarize the ground state properties of the Bose–Hubbard model with focusing on the superfluid-Mott-insulator quantum phase transitions. In addition, we discuss

collective excitations of the strongly-correlated superfluid near the transition. In the final part of this chapter, we introduce an effective pseudospin-1 mapping of the Bose–Hubbard model allowing us to characterize low-energy properties in the strongly-correlated regime. This approach is used in Chap. 4 to analyze the response functions combining with the field-theoretical linear-response theory and the local-density approximation.

In Chap. 3, we review the phase-space method for representing quantum systems using a classical phase-space language. There, we especially focus on the coherent-state Wigner representation of Bose fields. The fundamental ingredients building up the Wigner representation, i.e., the Wigner function and the Weyl symbol, are introduced to rewrite the quantum average of an arbitrary operator into an entirely classical form. The coherent-state phase-space representation of dynamics of Bose fields is formulated in terms of the time-dependent Wigner function. From this representation, we derive the TWA as a semiclassical approximation of the time evolution of the Wigner function. There, we also illustrate the schematic picture and advantages of the TWA. Furthermore, we review another approach to derive the TWA starting from a phase-space path-integral representation of quantum dynamics.

In Chap. 4, which is based on Ref. [64], we study responses of the Higgs modes to temporal modulations of the lattice amplitude and the onsite-interaction intensity in the cubic optical lattice. We analyze the linear-response functions using the effective pseudospin-1 model at high and unit fillings and the finite-temperature Green’s function perturbation theory. It is shown that when the density of the system is assumed to be uniform, we can observe a well-defined Higgs-type resonance peak in the the response functions even at typical temperatures. Furthermore, we calculate non-uniform trap effects on the response functions within the local density approximation and discuss the robustness of the resonance peak against the non-uniformity. There, we argue that if we perturb the condensate over a partial radius around the center of the trap, at which the density is tuned to unity, the resonance peak still survives at typical temperatures.

In Chap. 5, which is based on Ref. [65], we investigate far-from-equilibrium dynamics of Bose gases in optical lattices after sudden quantum quenches. Using the TWA, we numerically simulate the redistribution dynamics of the kinetic and onsite-interaction energies after a sudden quench from a singly-occupied Mott insulator state in a 3D optical lattice. Our results reveal that the TWA lines agree well with the experimental data without any fitting parameter. Furthermore, we analyze correlation spreading dynamics after a sudden quench in a 2D optical lattice. Especially we focus on the initial state dependence of the behavior of the correlation spreading.

In Chapter 6, we conclude this thesis and present outlooks to future subjects. Appendices A and B offer supplemental information for the main part.

# Chapter 2

## Ultracold Bose gases in optical lattices

In this chapter, we review fundamental properties of ultracold Bose gases tightly trapped by optical lattice potentials. In Sec. 2.1, we briefly describe the optical-dipole potentials for trapping neutral atoms and show how to generate optical lattice potentials in laboratories. In Sec. 2.2, we derive the single-band Bose–Hubbard model within the tight-binding approximation. In Sec. 2.3, we review the superfluid–Mott-insulator quantum phase transition of the ground state of the Bose–Hubbard model. In Sec. 2.4, we discuss collective excitation modes of the superfluid order parameter near the Mott-insulator transition. In Sec. 2.5, we formulate an effective-model description in a strongly-correlated regime by using a local Hilbert space truncation. This theoretical technique is used in Chap. 4 to analyze dynamical properties of strongly-correlated bosons in the vicinity of the superfluid–Mott-insulator transition.

### 2.1 Optical-lattice potentials

The spatially-periodic optical-lattice potential is a key ingredient to realize various Hubbard-type models in ultracold-gas experiments. The optical lattice is generated by standing-wave lasers far detuned from an atomic resonance in order to confine neutral atoms inside a lattice geometry of interest without optical dissipations [1]. When an atom is put in the presence of an oscillating (off-resonant) laser field  $\mathbf{E}(\mathbf{r}, t)$  with an angular frequency  $\omega_L$ , and it is detuned sufficiently far from an atomic resonance, then, a conservative force acts on the atom effectively, which is described by a laser-induced dipole potential [66–68]:

$$V_{\text{ind}}(\mathbf{r}) = -\frac{1}{2} \text{Re} [\alpha(\omega_L)] \overline{|\mathbf{E}(\mathbf{r}, t)|^2}, \quad (2.1)$$

where  $\alpha(\omega_L)$  is referred to as the complex AC polarizability and the overline indicates a time average. The induced potential can be regarded as an effective shift of atomic levels due to laser-induced virtual transitions between unperturbed atomic states, i.e., the AC Stark effect [66, 67].

The strength and sign of Eq. (2.1) depend on the laser intensity and frequency  $\omega_L$ .

As a simple example of the standing wave lasers, let us consider a superimposing pair of two counter-propagating lasers with the same wavelength  $\lambda_{\text{lat}}$  along  $x$ -direction

$$\mathbf{E}(x, t) = \hat{\mathbf{e}} E_0 \cos(k_{\text{lat}} x) \left[ e^{-i\omega_L t} + \text{c.c.} \right]. \quad (2.2)$$

Here,  $k_{\text{lat}} = 2\pi/\lambda_{\text{lat}}$  is the wave number and  $\hat{\mathbf{e}}$  denotes a unit vector oriented to the polarized direction. According to Eq. (2.1), in the presence of this laser field, atoms are trapped by a one-dimensional lattice potential as

$$V_{\text{lat}}^{\text{1D}}(x) = V_0 \cos^2(k_{\text{lat}} x). \quad (2.3)$$

The lattice depth  $V_0$  can be controlled by tuning the laser intensity  $I \sim E_0^2$ . The lattice spacing between two potential minima,  $d_{\text{lat}}$ , is determined from the wavelength such that  $d_{\text{lat}} = \lambda_{\text{lat}}/2$ . It is convenient to measure the lattice depth  $V_0$  with a unit of the recoil energy  $E_R$ , which is given by

$$E_R = \frac{\hbar^2 k_{\text{lat}}^2}{2m} = \frac{\hbar^2 \pi^2}{2m d_{\text{lat}}^2}. \quad (2.4)$$

Hence, the optical lattice potentials are conventionally written as

$$V_{\text{lat}}^{\text{1D}}(x) = s E_R \cos^2(k_{\text{lat}} x), \quad (2.5)$$

where  $s = V_0/E_R$ . The recoil energy implies an acquired energy of an atom after absorbing or emitting a photon with momentum  $\hbar k_{\text{lat}}$  from the laser field.

Inserting some orthogonal laser beams, we can also engineer a two-dimensional square or three-dimensional cubic optical lattice:

$$V_{\text{lat}}^{\text{2D}}(x, y) = s E_R \left[ \cos^2(k_{\text{lat}} x) + \cos^2(k_{\text{lat}} y) \right], \quad (2.6)$$

$$V_{\text{lat}}^{\text{3D}}(x, y, z) = s E_R \left[ \cos^2(k_{\text{lat}} x) + \cos^2(k_{\text{lat}} y) + \cos^2(k_{\text{lat}} z) \right]. \quad (2.7)$$

Furthermore, it is possible to realize various types of optical-lattice potential with a non-trivial geometry in ultracold-gas experiments. The examples established thus far include the double-well superlattice [69], checkerboard geometry [70], honeycomb (or hexagonal) lattice [71], triangular lattice [72, 73], Kagome lattice [74], and Lieb lattice [75]. For reviews, see Refs. [4, 5, 7].

## 2.2 Bose–Hubbard models

Let us consider an ultracold gas of spinless Bose atoms with an atomic mass  $m$  in the presence of a cubic optical lattice

$$V_{\text{lat}}(\mathbf{r}) = s E_R \left[ \sin^2(k_{\text{lat}} x) + \sin^2(k_{\text{lat}} y) + \sin^2(k_{\text{lat}} z) \right]. \quad (2.8)$$

This system is described by the following second-quantized Hamiltonian [1]:

$$\hat{H}_b = \int d\mathbf{r} \hat{\psi}^\dagger(\mathbf{r}) \left[ -\frac{\hbar^2 \nabla^2}{2m} + V_{\text{lat}}(\mathbf{r}) \right] \hat{\psi}(\mathbf{r}) + \frac{g}{2} \int d\mathbf{r} \hat{\psi}^\dagger(\mathbf{r}) \hat{\psi}^\dagger(\mathbf{r}) \hat{\psi}(\mathbf{r}) \hat{\psi}(\mathbf{r}), \quad (2.9)$$

where  $g = 4\pi\hbar^2 a_s/m$  and  $a_s$  are the coupling constant and  $s$ -wave scattering length, respectively. The boson annihilation and creation operators  $\hat{\psi}(\mathbf{r})$  and  $\hat{\psi}^\dagger(\mathbf{r})$  satisfy the canonical commutation relations:

$$[\hat{\psi}(\mathbf{r}), \hat{\psi}^\dagger(\mathbf{r}')] = \delta(\mathbf{r} - \mathbf{r}'), \quad [\hat{\psi}(\mathbf{r}), \hat{\psi}(\mathbf{r}')] = [\hat{\psi}^\dagger(\mathbf{r}), \hat{\psi}^\dagger(\mathbf{r}')] = 0. \quad (2.10)$$

When the lattice potential is sufficiently deep, the lowest-lying first band is most dominant and the higher-band contributions are negligible because the energy gap of the first and second bands is much larger than the thermal and mean-field interaction energies per atom [76]. Therefore, it is allowed to expand the Bose field operator with respect to the lowest-band Wannier basis:

$$\hat{\psi}(\mathbf{r}) = \sum_i \hat{a}_i w_0(\mathbf{r} - \mathbf{R}_i), \quad \hat{\psi}^\dagger(\mathbf{r}) = \sum_i \hat{a}_i^\dagger w_0^*(\mathbf{r} - \mathbf{R}_i), \quad (2.11)$$

where  $i = (i_x, i_y, i_z)$  is an integer-valued vector and  $\mathbf{R}_i = d_{\text{lat}}(i_x, i_y, i_z)$  indicates the lattice minima. The function  $w_0(\mathbf{r} - \mathbf{R}_i)$  is the lowest-band Wannier function, which is supposed to be localized around  $\mathbf{r} = \mathbf{R}_i$ . The new canonical operators  $\hat{a}_i$  and  $\hat{a}_i^\dagger$  are introduced so that

$$[\hat{a}_i, \hat{a}_j^\dagger] = \delta_{i,j}, \quad [\hat{a}_i, \hat{a}_j] = [\hat{a}_i^\dagger, \hat{a}_j^\dagger] = 0. \quad (2.12)$$

The lattice operator  $\hat{a}_i$  annihilates a boson localized around  $i$ -th site.

Substituting Eq. (2.11) into Eq. (2.9) and making the tight-binding approximation, we obtain the single-band Bose–Hubbard model [1, 77],

$$\hat{H}_b \approx \hat{H}_{\text{BH}} = -J \sum_{\langle i,j \rangle} (\hat{a}_i^\dagger \hat{a}_j + \text{h.c.}) + \frac{U}{2} \sum_i \hat{a}_i^\dagger \hat{a}_i^\dagger \hat{a}_i \hat{a}_i, \quad (2.13)$$

where the bracket symbol  $\langle i, j \rangle$  implies a nearest neighbor pair. In this representation, the first term means the kinetic energy associated with hopping of atoms from site to site. The second term gives the energy increase when some atoms come into a same site. These energies are characterized by the hopping amplitude  $J$  and the onsite-interaction intensity  $U$ . They are described by the localized Wannier functions such that

$$J = - \int d\mathbf{r} w_0^*(\mathbf{r} - \mathbf{R}_i) \left[ -\frac{\hbar^2 \nabla^2}{2m} + V_{\text{lat}}(\mathbf{r}) \right] w_0(\mathbf{r} - \mathbf{R}_j), \quad (2.14)$$

$$U = g \int d\mathbf{r} |w_0(\mathbf{r})|^4, \quad (2.15)$$

where  $|i - j| = 1$ . No offset term per each site is assumed to arise from Eq. (2.14) at  $i = j$ . In experiments, the dimensionless ratio  $J/U$  is tunable though changing the optical-lattice depth or using the Feshbach resonance [1, 2, 4, 8].

To illustrate the dependence of  $J$  and  $U$  on the lattice depth, here we extract approximate results of them from Ref. [4]. At three dimensions and for a deep-lattice limit  $s \gg 1$ , they approximately behave like

$$J \sim \frac{4}{\sqrt{\pi}} s^{3/4} \exp(-2\sqrt{s}) E_R, \quad (2.16)$$

$$U \sim \frac{8}{\pi} \frac{a_s}{d_{\text{lat}}} A_I^3 s^{3B_I} E_R, \quad (2.17)$$

where  $(A_I, B_I) = (\sqrt{\pi/2}, 1/4)$ . As  $s$  increases, the hopping amplitude decreases exponentially because it characterizes a tunneling property between adjacent sites. In contrast, the interaction intensity algebraically grows with  $s$ .

In typical setups of cold-atomic experiments, there is also a non-uniform external potential to confine the atoms. If effects of the confinement cannot be neglected, we have to insert an additional term into Eq. (2.13). Indeed, in the existence of a non-uniform trapping potential  $V_{\text{trap}}(\mathbf{r})$ , which varies slowly over space, the Bose–Hubbard model acquires a local offset energy [1]:

$$\hat{H}_{\text{trap}} = \sum_i \epsilon_i \hat{a}_i^\dagger \hat{a}_i, \quad (2.18)$$

where the one-body offset  $\epsilon_i$  is given by

$$\epsilon_i = \int d\mathbf{r} V_{\text{trap}}(\mathbf{r}) |w_0(\mathbf{r} - \mathbf{R}_i)|^2 \approx V_{\text{trap}}(\mathbf{R}_i). \quad (2.19)$$

Trapping effects are important when we discuss the stability of the Higgs mode corresponding to experimental systems. The details will be presented in Chap. 4

Here it is convenient to introduce the grand canonical representation of the Bose–Hubbard model:

$$\hat{\mathcal{H}}_{\text{BH}} = -J \sum_{\langle i,j \rangle} (\hat{a}_i^\dagger \hat{a}_j + \text{h.c.}) + \frac{U}{2} \sum_i \hat{a}_i^\dagger \hat{a}_i^\dagger \hat{a}_i \hat{a}_i - \mu \sum_i \hat{a}_i^\dagger \hat{a}_i. \quad (2.20)$$

For the cold-atomic systems, the chemical potential  $\mu$  is generally dependent on the site due to the trapping potential. Such a non-uniform effect is given by the offset energy  $\epsilon_i$ .

## 2.3 Superfluid-Mott-insulator quantum phase transitions

The Bose–Hubbard model has two different ground states (so called *quantum phases*) depending on the dimensionless local interaction  $U/J$  and the mean occupation per site [77]. When the density is incommensurate, the bosons can form a superfluid phase at zero temperature for any local

interaction. In contrast, when the density is commensurate and the interaction becomes greater than a threshold value, the ground state undergoes a phase transition into a Mott-insulator phase at zero temperature. Such a zero-temperature transition, which is essentially driven by quantum fluctuations stemming from a competition between two non-commutative parts in  $\hat{H}_{\text{BH}}$ , i.e., the kinetic and interaction energies, is called *quantum phase transitions* [80]. The quantum phase transition should be contrasted with conventional classical phase transitions, which are induced by thermal fluctuations.

When the spatial dimension is greater than one ( $d > 1$ ), the superfluid state exhibits a long-range order while the insulator state is disordered [77]. Then, the transition is regarded as a second-order transition [77, 79–82]. The phases are distinguished by a local complex number (order parameter) associated with spontaneous breaking of U(1) symmetry. On the other hand, at one dimension ( $d = 1$ ), there is no phase transition with continuous-symmetry breaking even at zero temperature (the Mermin–Wagner–Coleman theorem [83, 84]) because long-range orders are melted by strong quantum fluctuations. Nevertheless, the one-dimensional ground state can exhibit a *topological* phase transition without symmetry breaking, which is referred to as the Berezinskii–Kosterlitz–Thouless transition [85–89].

The Mott-insulator state is incompressible and has two gapped elementary excitations, i.e., the particle and hole excitations [77]. Both of these energy gaps vanish at the phase transition point. On the other hand, the superfluid state is compressible and has a gapless excitation. For  $d > 1$  this excitation is nothing but the Nambu–Goldstone (NG) mode. In contrast, at  $d = 1$ , the gapless excitation, which is related with the quasi-long range order, is universally described by the Tomonaga–Luttinger liquid theory [89].

The superfluid-Mott-insulator transition is characterized by the behaviors of the energy gap  $\Delta$  and correlation length  $\xi$  [80]. Approaching the transition point, the energy gap vanishes and the correlation length diverges as

$$\Delta \sim J|w - w_c|^{\nu z_{\text{dyn}}}, \quad \xi^{-1} \sim d_{\text{lat}}^{-1}|w - w_c|^\nu, \quad (2.21)$$

where  $w$  is a dimensionless parameter and  $w_c$  indicates the transition point. The so called critical exponents  $\nu$  and  $z_{\text{dyn}}$  are usually independent of the microscopic detail of the lattice system [80]. In the vicinity of the transition point, associated with the divergence of the time and length scales, some important physical quantities, e.g., correlation functions of the ground state, obtain a scaling form described by a set of such *universal* critical exponents. The superfluid-Mott-insulator transition belongs to the universality class of the critical phenomena of the  $(d + 1)$ -dimensional classical XY model [77]. In particular, the dynamical exponent  $z_{\text{dyn}}$  is predicted as  $z_{\text{dyn}} = 1$ . We can also induce a similar superfluid-insulator transition by varying the mean occupancy or chemi-

cal potential [77]. Then, the transition is described by the universality class of the dilute Bose-gas transition, and the dynamical exponent is not unity, but  $z_{\text{dyn}} = 2$  [80].

The superfluid-Mott-insulator transition of the Bose–Hubbard model has been observed experimentally in ultracold  $^{87}\text{Rb}$  atoms in a 3D optical lattice [2]. In the experiment, interference patterns of expanding gases released from external potentials were imaged by using the time-of-flight technique at different optical-lattice depths. The experimental results clearly detected a characteristic onset of the quantum phase transition, i.e., losing or restoring of phase coherence in the interference patterns.

### 2.3.1 Mean-field theory of the superfluid-Mott-insulator transition

Mean-field calculations are helpful to roughly imagine the ground state properties of the Bose–Hubbard model. The superfluid-Mott-insulator transition can be described within several mean-field treatments such as the site-decoupling mean-field approach [79] and the Gutzwiller’s variational ansatz [26, 90–92]. It should be stressed that the phase transition into the Mott-insulator state cannot be captured within the standard Bogoliubov approximation [79].

According to Ref. [79], let us determine the phase boundary using the site-decoupling mean-field approximation. In this scheme, we need to approximate the (non-local) kinetic-energy operator in the Bose–Hubbard model as a local operator such that

$$\hat{a}_i^\dagger \hat{a}_j = \psi(\hat{a}_i^\dagger + \hat{a}_i) - \psi^2, \quad (2.22)$$

where  $\psi$  is a mean field,  $\psi = \langle \hat{a}_i \rangle$ , and it is assumed to be real. Performing this approximation, computing the ground state energy, and making the Ginzburg–Landau expansion, we obtain the value of the chemical potential at the phase boundary, which is a function of  $zJ/U$  and the filling factor  $n_0$  of the Mott-insulator phase:

$$\mu_{\pm} = \frac{1}{2}(2n_0 - 1 - Jz/U) \pm \frac{1}{2} \sqrt{1 - 2(Jz/U)(2n_0 + 1) + (Jz/U)^2}, \quad (2.23)$$

where  $z = 2d$  is the coordination number. The subscript  $\pm$  indicates the upper and lower lines of the Mott-insulator regimes. In Fig. 2.1, we draw Eq. (2.23) in the  $zJ$ - $\mu$  plane. The phase boundary has a lobe-like shape, which surrounds the regimes of the Mott-insulator state. It should be noted that each tip of the Mott lobes corresponds to a commensurate density. Equating  $\mu_+$  and  $\mu_-$ , we obtain the critical value of the commensurate phase transition at the tips:

$$\left(\frac{U}{zJ}\right)_c = 2n_0 + 1 + \sqrt{(2n_0 + 1)^2 - 1} = (\sqrt{n_0 + 1} + \sqrt{n_0})^2. \quad (2.24)$$

As we will see in Sec. 2.5.4, the entirely same result can be derived from the Gutzwiller’s approach.

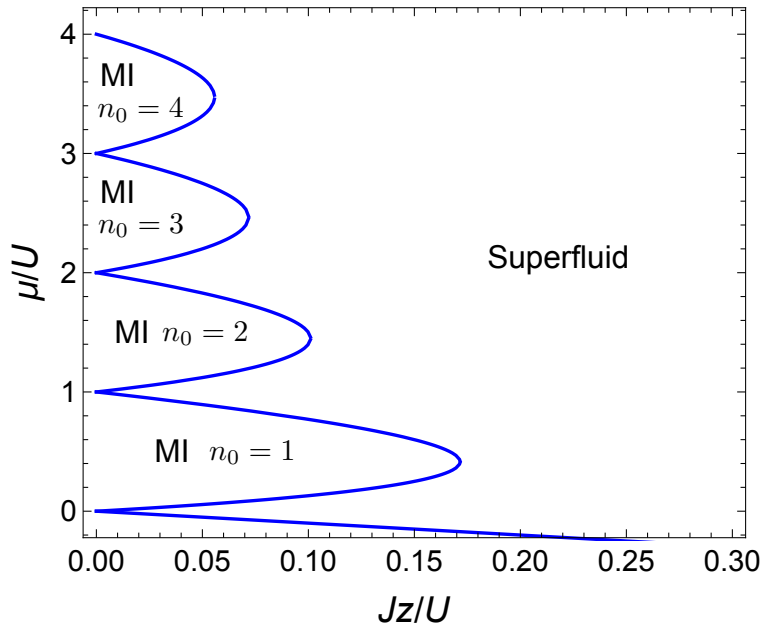


Figure 2.1: Mean-field phase diagram of the Bose–Hubbard model at zero temperature. The vertical axis is the chemical potential and the horizontal axis is the tunneling amplitude. The blue-solid line indicates the phase boundary derived from the site-decoupling mean-field approximation (see also Ref. [79]). Each “lobe” corresponds to a Mott-insulator regime with occupation  $n_0$ .

For more quantitative results beyond the mean-field treatments, it is needed to deal with quantum fluctuation effects relying on more technical and complicated non-perturbative methods. The correct phase boundary has been computed by some quasi-exact numerical techniques at  $n_0 = 1$ , e.g., quantum Monte-Carlo (QMC) simulations for  $d = 2$  [82] and  $d = 3$  [81], and a density matrix renormalization group (DMRG) approach for  $d = 1$  [93]. For higher-filling rates, quantitative determinations of the phase boundary are also possible by applying the strong-coupling expansion [78].

### 2.3.2 Field-theoretical description of the quantum phase transition

In Sec. 2.4, we will review the Higgs mode of superfluid Bose gases near the quantum phase transition. For the purpose, let us here introduce a field-theoretical description of the transition [80, 94]. Our starting point is a grand-canonical partition function of the Bose–Hubbard model (2.20), which is written as a coherent-state path-integral form [80, 94]:

$$\Xi = \int \mathcal{D}a^* \mathcal{D}a e^{-S_{\text{BH}}[a^*, a]}. \quad (2.25)$$

The weight function of the path integral is characterized by the Euclidean action for the Bose–Hubbard model,

$$S_{\text{BH}}[a^*, a] = \int_{-\beta/2}^{\beta/2} d\tau \sum_i \left\{ a_i^*(\tau) \left( \frac{\partial}{\partial \tau} - \mu \right) a_i(\tau) + \frac{U}{2} a_i^*(\tau) a_i^*(\tau) a_i(\tau) a_i(\tau) \right\} - J \int_{-\beta/2}^{\beta/2} d\tau \sum_{\langle i,j \rangle} \left\{ a_i^*(\tau) a_j(\tau) + a_j^*(\tau) a_i(\tau) \right\}. \quad (2.26)$$

The complex field  $a_i(\tau)$  depends on the imaginary time  $\tau \in [-\beta/2, \beta/2]$  and represents the fluctuations of the lattice Bose field. Moreover,  $\beta = (k_{\text{B}}T)^{-1}$  denotes the inverse temperature. Throughout this subsection, we set  $\hbar = 1$  for simplicity.

Suppose that the system is in a superfluid phase near the Mott-insulator transition. Let us derive an effective action characterizing the low-energy collective behaviors of the superfluid phase (for details, see Ref. [94]). As a first step, we take a Hubbard–Stratonovich transformation with a complex axillary field  $\Psi_i$ , which corresponds to the superfluid order parameter. Then, we integrate out the original Bose fields and define the action of the remaining axillary fields:

$$\Xi = \int \mathcal{D}a^* \mathcal{D}a \mathcal{D}\Psi^* \mathcal{D}\Psi e^{-S_{\text{BH}}[a^*, a, \Psi^*, \Psi^*]} = \int \mathcal{D}\Psi^* \mathcal{D}\Psi e^{-\tilde{S}[\Psi^*, \Psi^*]}, \quad (2.27)$$

where  $\tilde{S}[\Psi^*, \Psi^*]$  is in general a complicated functional of the arguments. Performing an expansion of  $\tilde{S}[\Psi^*, \Psi^*]$  with respect to  $\Psi_i$  up to the fourth order and taking a continuous limit, we obtain

$$\Xi \approx \int \mathcal{D}\psi^* \mathcal{D}\psi e^{-S_{\text{eff}}[\psi^*, \psi]}, \quad (2.28)$$

where  $\psi(\tau, \mathbf{x})$  is a rescaled field introduced as  $\psi = \Psi(d_{\text{lat}}^{d/2} zJ)^{-1}$  [94]. The effective action  $S_{\text{eff}}[\psi^*, \psi]$  describing the superfluid order parameter is given as follows:

$$S_{\text{eff}} = \beta F_0 + \int d\tau \int d^d x \left\{ K_1 \psi^* \frac{\partial}{\partial \tau} \psi + K_2 \left| \frac{\partial}{\partial \tau} \psi \right|^2 + \frac{1}{2m_*} |\nabla \psi|^2 + r |\psi|^2 + \frac{u}{2} |\psi|^4 \right\}, \quad (2.29)$$

where  $F_0$  is the free-energy density along with the imaginary-time axis. The coefficients  $K_1$ ,  $K_2$ ,  $m_*$ ,  $r$ , and  $u$  are functions of the microscopic parameters of the Bose–Hubbard model. The explicit forms are found in e.g. Ref. [94].

The static part of the effective action except for the dynamical terms, which are proportional to  $K_1$  or  $K_2$ , characterizes the (saddle-point) ground state configuration of the order parameter. Assuming that the system takes spatially-uniform configurations of the order parameter, we find that the configuration

$$|\psi| = \sqrt{-\frac{r}{u}} \quad \text{or} \quad |\psi| = 0 \quad (2.30)$$

minimizes the effective action for  $r < 0$  or  $r > 0$ . Thus,  $r < 0$  ( $r > 0$ ) corresponds to the order (disorder) phase, and  $r = 0$  defines the phase boundary.

It is important to emphasize that  $K_1$  and  $K_2$  should satisfy the following relations [80, 94]:

$$K_1 = -\frac{\partial r}{\partial \mu}, \quad K_2 = \frac{1}{2} \frac{\partial K_1}{\partial \mu}. \quad (2.31)$$

These follow from the invariance of the effective action with respect to the U(1) gauge transformation such that  $\psi \rightarrow \psi e^{i\phi}$  and  $\mu \rightarrow \mu + i \frac{\partial \phi}{\partial \tau}$ . In particular, the former one implies that  $K_1$  vanishes at the tip of the Mott lobe, at which the atomic density is commensurate. There, the effective action acquires an effective Lorentz invariance: it is invariant with respect to the complex-conjugated pair replacement of the field  $\psi \rightarrow \psi^*$ . This is nothing but the origin of the dynamical critical exponent  $z_{\text{dyn}} = 1$  near the Mott-insulator transition at commensurate densities. Due to such a characteristic property, the superfluid near the Mott-insulator transition can show emergent-relativistic dynamics of the order parameter, such as the Higgs mode (see the next section) [26].

## 2.4 Higgs and Nambu–Goldstone modes

Let us consider real-time dynamics of the commensurate superfluid near the Mott-insulator transition. Our starting point is the analytically-continued effective action of Eq. (2.29) at  $K_1 = 0$  [95], which is given by

$$\mathcal{S}_{\text{eff}} = \int dt \int d^d x \left\{ -K_2 \left| \frac{\partial}{\partial t} \psi \right|^2 + \frac{1}{2m_*} |\nabla \psi|^2 + r |\psi|^2 + \frac{u}{2} |\psi|^4 \right\}, \quad (2.32)$$

where  $t$  represents the real-time axis. Setting  $\delta \mathcal{S}_{\text{eff}} / \delta \psi^* = \delta \mathcal{S}_{\text{eff}} / \delta \psi = 0$ , we obtain the relativistic non-linear Klein–Gordon equation describing the saddle-point dynamics of the order parameter:

$$K_2 \ddot{\psi} - \frac{1}{2m_*} \nabla^2 \psi + r \psi + u \psi |\psi|^2 = 0. \quad (2.33)$$

Unlike the Gross–Pitaevskii equation, this equation notably possesses the second-order time-derivative term.

To describe low-energy collective fluctuations of the order parameter, let us linearize the Klein–Gordon equation with respect to a small fluctuation around the equilibrium configuration  $\psi = \psi_{\text{eq}} = \sqrt{-r/u}$  [cf. Eq. (2.30)]:

$$\psi(t) = \psi_{\text{eq}} + \mathcal{U} e^{i\mathbf{p}\cdot\mathbf{r} - i\omega t} - \mathcal{V} e^{-i\mathbf{p}\cdot\mathbf{r} + i\omega t}, \quad (2.34)$$

where  $\mathcal{U}$  and  $\mathcal{V}$  are small amplitudes, and  $\mathbf{p}$  and  $\omega$  are the momentum and frequency of the fluctuation, respectively. Notice that  $\mathcal{U} - \mathcal{V}$  corresponds to an amplitude fluctuation of the order

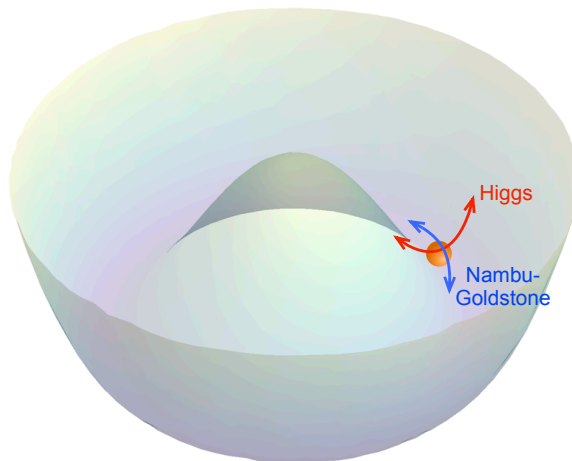


Figure 2.2: Schematic picture of the Higgs and NG modes. The Higgs mode corresponds to an amplitude oscillation of the order parameter along the radial direction of the mexican-hat potential. On the other hand, the NG mode corresponds to a phase oscillating motion of that on the bottom of the potential along the azimuthal direction.

parameter while  $\mathcal{U} + \mathcal{V}$  does to a phase fluctuation of that. Substituting this into Eq. (2.33) and neglecting the high-order contributions, we find that there are two orthogonal eigen modes corresponding to the amplitude and phase oscillations. The corresponding eigen frequencies are calculated as follows:

$$\omega_{\text{higgs}} = \sqrt{\Delta_{\text{higgs}}^2 + c^2|\mathbf{p}|^2}, \quad \omega_{\text{ng}} = c|\mathbf{p}|, \quad (2.35)$$

where  $c^2 = (2m_*K_2)^{-1}$ . The former dispersion  $\omega_{\text{higgs}}$  describes the amplitude fluctuation mode and opens an energy gap  $\Delta_{\text{higgs}} = \sqrt{-2r/K_2}$  if  $r < 0$ . This mode is referred to as the Higgs or amplitude mode [95]. On the other hand, the latter gapless dispersion  $\omega_{\text{ng}}$  characterizes the phase fluctuation mode of the order parameter. This is known as the Nambu–Goldstone (NG) or phase mode associated with restoring of the U(1) symmetry [95]. The schematic picture of these modes is depicted in Fig. 2.2.

Such separation and orthogonality of the amplitude and phase fluctuations stem from the fact that they are no longer canonical conjugate with each other when the effective action has the relativistic Lorentz invariance. In other words, each sector of fluctuations has its own conjugated momentum. The amplitude fluctuation and its conjugate momentum (not the phase fluctuation) form one collective mode, i.e., the gapped Higgs amplitude mode, which is independent of the phase fluctuation. In a similar way, the phase fluctuation and its conjugate momentum also form the

gapless NG phase mode independently. This is in contrast to the non-relativistic Gross–Pitaevskii case, where the phase fluctuation is canonical conjugate with the amplitude one. In this case, these degrees of freedom form only one collective mode, namely the gapless Bogoliubov mode.

The Higgs mode can ubiquitously emerge in general thermodynamic phases with a particle-hole symmetry and spontaneous breaking of a continuous symmetry [95, 96]. This feature has attracted particular attention from many experimental research fields of condensed matter and ultra-cold gases [95]. The examples of quantum many-body systems, which can show the Higgs mode, include superconductors NbSe<sub>2</sub> [97–101] and Nb<sub>1-x</sub>Ti<sub>x</sub>N [102–105], quantum antiferromagnets TlCuCl<sub>3</sub> [106, 107] and KCuCl<sub>3</sub> [108], charge density wave materials K<sub>0.3</sub>MoO<sub>3</sub> [109, 110] and TbTe<sub>3</sub> [111, 112], superfluid <sup>3</sup>He B-phase [113, 114], two-component Fermi gases across the BCS-BEC crossover [115], and superfluid Bose gases in optical lattices [18, 19]. Moreover, the Higgs mode can be regarded as a counterpart of the Higgs boson in the standard theory of high energy physics [116].

Within the linear approximation, the Higgs and NG modes can be defined as decoupled eigenmodes (or steady solutions) of the order parameter dynamics. However, in more realistic situations, these modes have intrinsic damping rates because there are actually interactions between them due to the non-linearity of the original model. Indeed, the Higgs mode can attenuate into two NG modes, and the damping property affects its visibility in experimental probes [26, 37, 46]. The damping rate of the Higgs mode arises from a virtual transition mediated by such Higgs-NG interactions. In a perturbative picture of the field-theoretical language, it can be interpreted as a loop correction to the eigen energy of the Higgs mode, which stems from quantum and thermal fluctuations [37, 46].

## 2.5 Hilbert-space truncation and effective pseudospin-1 models

In this section, we focus on an effective and microscopic description of the strongly-interacting regime of the Bose–Hubbard model for  $U/J \gg 1$ . For the purpose, it is convenient to modify our notation of the Bose–Hubbard model (2.20) as follows:

$$\hat{\mathcal{H}}_{\text{BH}} = -J \sum_{\langle ij \rangle} \hat{a}_i^\dagger \hat{a}_j + \frac{U}{2} \sum_i (\hat{n}_i - n_0)^2 - \sum_i \mu (\hat{n}_i - n_0),$$

where  $n_i = \hat{a}_i^\dagger \hat{a}_i$  is the density operator at site  $i$  and  $n_0$  is the commensurate filling factor. The difference from the original definition is the origin of the chemical potential.

This section is organized as follows: In Sec. 2.5.1, we introduce a reduced local Hilbert space to define a strongly-correlated effective model and a pseudospin representation of physical operators in the projected space based on the Schwinger-boson theory. In Sec. 2.5.2, we derive an

effective model for a large-filling limit and discuss its intrinsic property, i.e., an effective particle-hole symmetry. In Sec. 2.5.3, we generalize the large-filling effective model into low-filling cases, which correspond to typical setups in ultracold-gas experiments. In Sec. 2.5.4, we discuss the ground state property of the effective model within a Gutzwiller's mean-field ansatz. Finally, in Sec. 2.5.5, especially at a high-filling limit, we derive mean-field dispersion relations of elementary excitations inside the superfluid and Mott-insulator phases, respectively.

### 2.5.1 Reduced Hilbert space in strongly-correlated regimes

Let us assume that the system involves an integer number of particles with  $\langle \hat{n}_i \rangle = n_0$ . At a sufficiently large interaction compared with the hopping amplitude, local fluctuations of  $\hat{n}_i$  from the mean density are strongly suppressed. Therefore, low-energy properties of the system can be described by an effective model

$$\hat{\mathcal{H}}_{\text{eff}}^{n_0} = \mathcal{P}_{n_0} \hat{\mathcal{H}}_{\text{BH}} \mathcal{P}_{n_0}^{-1}, \quad (2.36)$$

where  $\mathcal{P}_{n_0}$  is a projection operator eliminating high-energy Fock states  $|n_0 + \alpha\rangle$  for  $|\alpha| > 1$  from the complete Hilbert space. The remaining states, which effectively describe the low-energy phenomena, can be represented by three Schwinger bosons [26, 46, 92, 117],

$$|n_0 + 1\rangle_j \equiv \hat{t}_{1,j}^\dagger |\text{vac}\rangle, \quad |n_0\rangle_j \equiv \hat{t}_{0,j}^\dagger |\text{vac}\rangle, \quad |n_0 - 1\rangle_j \equiv \hat{t}_{-1,j}^\dagger |\text{vac}\rangle, \quad (2.37)$$

where  $|\text{vac}\rangle$  is the vacuum of new bosons. The new bosons fulfill the commutation relations

$$[\hat{t}_{\alpha,i}, \hat{t}_{\alpha',j}^\dagger] = \delta_{\alpha,\alpha'} \delta_{i,j}, \quad [\hat{t}_{\alpha,i}, \hat{t}_{\alpha',j}] = [\hat{t}_{\alpha,i}^\dagger, \hat{t}_{\alpha',j}^\dagger] = 0. \quad (2.38)$$

In order to eliminate the unphysical states such as  $\hat{t}_{1,i}^\dagger \hat{t}_{0,i}^\dagger |\text{vac}\rangle$ , we assume that these operators obey a local holonomic constraint

$$\sum_{\alpha=-1}^1 \hat{t}_{\alpha,i}^\dagger \hat{t}_{\alpha,i} = \hat{1}, \quad (2.39)$$

where  $\hat{1}$  on the righthand side is the identity operator in the reduced Hilbert subspace.

In the projected Hilbert space, each of local operator that constitutes the model Hamiltonian,  $\hat{a}_i, \hat{a}_i^\dagger$ , and  $\delta \hat{n}_i = \hat{n}_i - n_0$ , reduces to a simple form represented by the constrained Schwinger bosons  $\hat{t}_\alpha, \hat{t}_\alpha^\dagger$  ( $\alpha = -1, 0, 1$ ). In terms of the bosons, the operators read

$$\begin{aligned} \mathcal{P}_{n_0} \hat{a}_i^\dagger \mathcal{P}_{n_0}^{-1} &= \sqrt{n_0 + 1} \hat{t}_{1,i}^\dagger \hat{t}_{0,i} + \sqrt{n_0} \hat{t}_{0,i}^\dagger \hat{t}_{-1,i}, \\ \mathcal{P}_{n_0} \hat{a}_i \mathcal{P}_{n_0}^{-1} &= \sqrt{n_0 + 1} \hat{t}_{0,i}^\dagger \hat{t}_{1,i} + \sqrt{n_0} \hat{t}_{-1,i}^\dagger \hat{t}_{0,i}, \\ \mathcal{P}_{n_0} \delta \hat{n}_i \mathcal{P}_{n_0}^{-1} &= \hat{t}_{1,i}^\dagger \hat{t}_{1,i} - \hat{t}_{-1,i}^\dagger \hat{t}_{-1,i}. \end{aligned}$$

Here, let us introduce pseudospin-1 operators of the Schwinger bosons, which are defined by

$$\hat{S}_i^+ = \sqrt{2}(\hat{t}_{1,i}^\dagger \hat{t}_{0,i} + \hat{t}_{0,i}^\dagger \hat{t}_{-1,i}), \quad \hat{S}_i^- = \sqrt{2}(\hat{t}_{0,i}^\dagger \hat{t}_{1,i} + \hat{t}_{-1,i}^\dagger \hat{t}_{0,i}), \quad \hat{S}_i^z = \hat{t}_{1,i}^\dagger \hat{t}_{1,i} - \hat{t}_{-1,i}^\dagger \hat{t}_{-1,i}. \quad (2.40)$$

It is easy to see that these operators satisfy the standard SU(2) commutation relations such that

$$[\hat{S}_i^+, \hat{S}_j^-] = 2\hat{S}_i^z \delta_{i,j}, \quad [\hat{S}_i^z, \hat{S}_j^\pm] = \pm \hat{S}_i^\pm \delta_{i,j}. \quad (2.41)$$

In addition, there exists a conserved Casimir operator, which commutes all of the ingredients of the algebra, such that  $\sum_{\alpha=x,y,z} (\hat{S}_j^\alpha)^2 = 2 \equiv S(S+1)$ , where  $\hat{S}_j^\pm = \hat{S}_j^x \pm i\hat{S}_j^y$ . Using the pseudospin representation, we obtain

$$\mathcal{P}_{n_0} \hat{a}_i^\dagger \mathcal{P}_{n_0}^{-1} = \sqrt{\frac{n_0}{2}} (1 + \delta\nu \hat{S}_i^z) \hat{S}_i^+, \quad \mathcal{P}_{n_0} \hat{a}_i \mathcal{P}_{n_0}^{-1} = \sqrt{\frac{n_0}{2}} \hat{S}_i^- (1 + \delta\nu \hat{S}_i^z), \quad \mathcal{P}_{n_0} \delta \hat{n}_i \mathcal{P}_{n_0}^{-1} = \hat{S}_i^z, \quad (2.42)$$

where  $\delta\nu = \sqrt{1 + 1/n_0} - 1$ . The results of the first and second equations have an explicit dependence on the projection center  $n_0$ . On the other hand, the righthand side of the final equation does not depend on  $n_0$ , so that it has the same form for any  $n_0$ .

## 2.5.2 Effective pseudospin-1 model at a high-filling limit

Applying the mapping formula (2.42), let us derive an explicit form of the strongly-interacting effective model at a large-occupation limit [26]. At  $n_0 \gg 1$ , the difference between  $\sqrt{n_0 + 1}$  and  $\sqrt{n_0}$  vanishes and  $\delta\nu$  approaches to zero. In this limit, the creation and annihilation operators of bosons are effectively written as

$$\mathcal{P}_{n_0} \hat{a}_i^\dagger \mathcal{P}_{n_0}^{-1} \approx \sqrt{\frac{n_0}{2}} \hat{S}_i^+, \quad \mathcal{P}_{n_0} \hat{a}_i \mathcal{P}_{n_0}^{-1} \approx \sqrt{\frac{n_0}{2}} \hat{S}_i^-. \quad (2.43)$$

Substituting these results into Eq. (2.36), we obtain an effective pseudospin-1 model [26],

$$\hat{\mathcal{H}}_{\text{eff}}^{n_0 \gg 1} = -\frac{Jn_0}{2} \sum_{\langle ij \rangle} \hat{S}_i^+ \hat{S}_j^- + \frac{U}{2} \sum_i (\hat{S}_i^z)^2 - B \sum_i \hat{S}_i^z, \quad (2.44)$$

where  $B = \mu$  is the uniform *magnetic field* coupling with the z-component of the pseudospins. The XY spin exchange, on-site single-ion anisotropy, and magnetic coupling terms correspond to the hopping, onsite-interaction, and chemical potential terms in the original Bose–Hubbard model, respectively.

The effective model (2.44) was first obtained by Altman and Auerbach in 2002 [26]. They used it to investigate dynamical properties of superfluid Bose gases with a large occupation, in particular, oscillations of the superfluid order parameter in the vicinity of the Mott-insulator transition [26]. Furthermore, this model has been utilized for examining universal aspects of adiabatic-limit dynamics near a quantum phase transition [118], estimating damping rates of the Higgs and

NG modes at finite temperatures and at three dimensions [46], and demonstrating the applicability of the SU(3) truncated-Wigner approximation to ultracold gas systems [119].

An important feature of Eq. (2.44) is its explicit particle-hole symmetry at commensurate filling, which corresponds to  $B = \mu = 0$ . In the Schwinger-boson language, this symmetry can be seen as an invariance associated with an exchange between  $\hat{t}_1$  (particle) and  $\hat{t}_{-1}$  (hole). In Sec. 2.5.5, we will derive an energy dispersion of elementary excitations around a mean-field ground state using a Holstein–Primakoff expansion of the Schwinger bosons. There, we will see that the Higgs and NG branches are completely decoupled at a quadratic level due to the particle-hole symmetry. Furthermore, such an explicit symmetry forbids interactions associated with an odd number of the NG mode. It is worth noting that the relativistic Klein–Gordon-type effective action can be derived through the spin-coherent-state path-integral representation of the effective pseudospin-1 model at  $B = 0$  [26].

### 2.5.3 Effective pseudospin-1 model at low-filling rates

The high-filling model (2.44) does not correspond to typical experimental situations, where the filling factor is tuned to unity (see e.g. Ref. [19]). For lower commensurate filling rates ( $n_0 \sim 1$ ), we need to modify the spin exchange term [92] such that

$$\mathcal{H}_{\text{eff}}^{n_0} = -\frac{Jn_0}{2} \sum_{\langle ij \rangle} (1 + \delta\nu S_i^z) S_i^+ S_j^- (1 + \delta\nu S_j^z) + \frac{U}{2} \sum_i (S_i^z)^2 - B \sum_i S_i^z. \quad (2.45)$$

The modified model (2.45) has no longer the explicit particle-hole symmetry seen in the high-filling model even at a commensurate filling rate. Note that  $\delta\nu$  measures the deviation from the particle-hole symmetric point. In fact, when we make a limit  $\delta\nu \rightarrow 0$ , the effective model obviously returns to the particle-hole symmetric model (2.44). The correction terms at low-filling rates were first discussed by Huber et al. [92].

In Chap. 4, we use the low-filling effective model (2.45) to analyze some response functions in the 3D Bose–Hubbard model at unit filling. Despite the absence of the particle-hole symmetry at the microscopic level, Eq. (2.45) is able to exhibit two independent collective excitations, i.e., the Higgs and NG modes, within a quadratic approximation of the Holstein–Primakoff expansion. This can be interpreted as that the system attains an emergent particle-hole symmetry near the Mott-insulator transition.

### 2.5.4 Gutzwiller’s variational ansatz in the reduced Hilbert space

Let us discuss the ground state of the projected effective model (2.45) within a mean-field approximation. To do that, we use a Gutzwiller’s variational ansatz according to Refs. [26, 92]. Our

starting point is to define a variational wave function spanned in the reduced Hilbert space [26,92]:

$$|\Omega(\theta, \eta, \varphi, \chi)\rangle = \prod_i \left\{ \cos\left(\frac{\theta}{2}\right) \hat{t}_{0,i}^\dagger + e^{i\eta} \sin\left(\frac{\theta}{2}\right) \left[ e^{i\varphi} \sin\left(\frac{\chi}{2}\right) \hat{t}_{1,i}^\dagger + e^{-i\varphi} \cos\left(\frac{\chi}{2}\right) \hat{t}_{-1,i}^\dagger \right] \right\} |\text{vac}\rangle, \quad (2.46)$$

where  $\theta \in [0, \pi]$ ,  $\eta \in [-\pi/2, \pi/2]$ ,  $\varphi \in [0, 2\pi]$ , and  $\chi \in [0, \pi]$  are the variational parameters. Note that this wave function at  $\theta = 0$  describes the Mott-insulating state of  $n_0$  filling factor with no fluctuation, i.e.  $\prod_i \hat{t}_{0,i}^\dagger |\text{vac}\rangle$ . In the superfluid phase,  $\theta \neq 0$  mixes the mean filling state  $\hat{t}_{0,i}^\dagger$  with the particle and hole fluctuations  $\hat{t}_{1,i}^\dagger$  and  $\hat{t}_{-1,i}^\dagger$ . Hence, it plays a role of the order parameter strength.

In the superfluid phase ( $\theta \neq 0$ ), the variational parameters are determined from minimizing the mean energy density  $E^{\text{MF}} = \langle \Omega | \mathcal{H}_{\text{eff}}^{n_0} | \Omega \rangle / M$  with respect to the variational parameters. Here,  $M$  is the total number of the lattice point. The explicit form can be computed as

$$E^{\text{MF}} = \left[ \frac{1}{2} + \mu \cos \chi \right] \sin^2\left(\frac{\theta}{2}\right) - \frac{Jz}{4} \sin^2 \theta \left[ n_0 + \sin^2\left(\frac{\chi}{2}\right) + \sqrt{n_0(n_0+1)} \sin \chi \cos 2\eta \right]. \quad (2.47)$$

After effecting the variation of Eq. (2.47) with respect to the variational parameters, we obtain a mean-field ground-state energy  $E_0(\theta_{\text{mf}}) = E^{\text{MF}}[\theta_{\text{mf}}, 0, 0, \chi(\theta_{\text{mf}})]$  where

$$\tan \chi(\theta) = -\frac{2Jz \sqrt{n_0(n_0+1)} [1 - \sin^2(\theta/2)]}{2\mu + Jz [1 - \sin^2(\theta/2)]}, \quad (2.48)$$

and  $\theta_{\text{mf}}$  is determined such that it minimizes the function  $E_0(\theta)$ . Using the optimized wave function after the variation, we also obtain the order parameter  $\Psi = \langle \Omega | a_i | \Omega \rangle$  and mean density  $\bar{n} = \langle \Omega | n_i | \Omega \rangle$  of the ground state as follows:

$$\Psi = \frac{1}{2} \sin \theta_{\text{mf}} \left[ \sqrt{n_0+1} \sin\left(\frac{\chi_{\text{mf}}}{2}\right) + \sqrt{n_0} \cos\left(\frac{\chi_{\text{mf}}}{2}\right) \right], \quad (2.49)$$

$$\bar{n} = n_0 - \sin^2\left(\frac{\theta_{\text{mf}}}{2}\right) \cos \chi_{\text{mf}}, \quad (2.50)$$

$$\chi_{\text{mf}} = \chi(\theta_{\text{mf}}). \quad (2.51)$$

It is easy to obtain an analytical form of  $\theta_{\text{mf}}$  at commensurate filling rates. In this case,  $\chi_{\text{mf}}$  turns out to be  $\chi_{\text{mf}} = \pi/2$  [see Eq. (2.51)]. Minimizing  $E^{\text{MF}}(\theta, 0, 0, \pi/2)$  with respect to  $\theta$ , we obtain

$$\theta_{\text{mf}} = \sin^{-1} \left( \sqrt{1 - (Jz)^{-2} (\sqrt{n_0+1} + \sqrt{n_0})^{-4}} \right), \quad (2.52)$$

and the corresponding chemical potential at  $\bar{n} = n_0$  reads

$$\mu_{n_0} = -\frac{1}{4} \left[ zJ + (\sqrt{n_0+1} + \sqrt{n_0})^{-2} \right]. \quad (2.53)$$

Furthermore, it is worth noting that at  $\chi_{\text{mf}} = \pi/2$  the ground state is particle-hole symmetric. This is because the corresponding wave function (2.46) contains  $t_{1,i}^\dagger$  and  $t_{-1,i}^\dagger$  components with equal weights at each site.

From the Ginzburg–Landau expansion of  $E^{\text{MF}}$  of the ground state with respect to the order parameter  $\Psi = \langle \Omega | a_i | \Omega \rangle$ , we can determine the phase-boundary of the superfluid to insulator transition [92]. Now we introduce a dimensionless parameter  $u = U/(4Jn_0z)$  measuring the distance from the critical point at the commensurate filling rate. The critical value of the superfluid to insulator transition within the mean-field approximation [92] is

$$u_c = \frac{1}{4n_0} (\sqrt{n_0 + 1} + \sqrt{n_0})^2. \quad (2.54)$$

At  $n_0 \rightarrow \infty$ , the critical value  $u_c$  approaches 1. At the unit filling rate  $n_0 = 1$ ,  $u_c = (\sqrt{2} + 1)^2/4 \approx 1.457$ . The same result has been obtained from the decoupling approximation of the Bose–Hubbard model (see Sec. 2.3.1). The exact critical value at the unit filling rate has been numerically computed as  $u_c = 1.22(2)$  by the quantum Monte-Carlo method of the 3D Bose–Hubbard model in Ref. [81]. In Chap. 4, we mainly use the mean-field result of Eq. (2.54) to be consistent with our analysis on the mean-field ground state.

### 2.5.5 Elementary excitations around the Gutzwiller’s wave function

Using the effective pseudospin-1 model and Gutzwiller’s wave function, we discuss elementary excitations around the Mott-insulator and superfluid states, respectively. For simplicity, we focus on the high-filling limit where the calculation is simple due to the particle-hole symmetry of the effective model. The low-filling generalization will be presented in Chap. 4 because it is closely related with our main analysis of this thesis. In this subsection, we assume the commensurate case  $B = 0$  in order to discuss the Higgs and NG modes. The following discussion is basically a review of Ref. [26].

To obtain the energy dispersion of elementary excitations in the superfluid phase (i.e., the amplitude and phase fluctuations), let us introduce a creation operator of the mean-field ground state  $|\Omega\rangle \equiv \prod_i \hat{b}_{0,i}^\dagger |\text{vac}\rangle$  and define a canonical transformation

$$\begin{aligned} \hat{b}_{0,i}^\dagger &= c_1 \hat{t}_{0,i}^\dagger + s_1 [s_2 \hat{t}_{1,i}^\dagger + c_2 \hat{t}_{-1,i}^\dagger], \\ \hat{b}_{1,i}^\dagger &= s_1 \hat{t}_{0,i}^\dagger - c_1 [s_2 \hat{t}_{1,i}^\dagger + c_2 \hat{t}_{-1,i}^\dagger], \\ \hat{b}_{2,i}^\dagger &= c_2 \hat{t}_{1,i}^\dagger - s_2 \hat{t}_{-1,i}^\dagger, \end{aligned} \quad (2.55)$$

where the coefficients are  $s_1 = \sin(\theta_{\text{mf}}/2)$ ,  $c_1 = \cos(\theta_{\text{mf}}/2)$ ,  $s_2 = \sin[\chi(\theta_{\text{mf}})/2]$ , and  $c_2 = \cos[\chi(\theta_{\text{mf}})/2]$ .  $\theta_{\text{mf}} (\neq 0)$  denotes the optimal value of  $\theta$  for the ground state.  $\hat{b}_{1,i}^\dagger$  describes the

amplitude fluctuation of the order parameter on the ground state while  $\hat{b}_{2,i}^\dagger$  describes the phase fluctuation. These new operators fulfill the same commutation relations as the old operators  $\hat{t}_{\alpha,i}$ . In addition, the transformation retains the constraint (2.39) so that

$$\sum_{m=0}^2 \hat{b}_{m,i}^\dagger \hat{b}_{m,i} = \hat{1}. \quad (2.56)$$

As a next step, we simplify the effective model by means of the Holstein–Primakoff (HP) expansion [117, 120]. Since the mean-field ground state can be regarded as a Bose–Einstein condensate of the constrained boson  $\hat{b}_{0,i}$ , we can eliminate  $\hat{b}_{0,i}$  by an expansion with respect to the fluctuations (*spin waves*)  $\hat{b}_{1,i}$  and  $\hat{b}_{2,i}$ :

$$\begin{aligned} \hat{b}_{m,i}^\dagger \hat{b}_{0,j} &= \hat{b}_{m,i}^\dagger \sqrt{1 - \hat{b}_{1,j}^\dagger \hat{b}_{1,j} - \hat{b}_{2,j}^\dagger \hat{b}_{2,j}}, \\ &\approx \hat{b}_{m,i}^\dagger - \frac{1}{2} \hat{b}_{m,i}^\dagger \hat{b}_{1,j}^\dagger \hat{b}_{1,j} - \frac{1}{2} \hat{b}_{m,i}^\dagger \hat{b}_{2,j}^\dagger \hat{b}_{2,j} + \dots \end{aligned} \quad (2.57)$$

When the expansion is stopped up to quadratic order, we obtain a free Hamiltonian, which describes the excitations within a non-interacting limit (the interacting effects are discussed in Chap. 4).

The quadratic Hamiltonian can be diagonalized using the standard Bogoliubov transformation [121]. In the high-filling limit, the transformation can be performed independently in each branch because the amplitude and phase sectors are completely decoupled due to the explicit particle-hole symmetry. It is important to note that the HP expansion does not destroy that symmetry. Therefore, we rotate the operator basis with a canonical transformation given by

$$\hat{b}_{m,\mathbf{k}} = u_{m,\mathbf{k}} \hat{\beta}_{m,\mathbf{k}} + v_{m,-\mathbf{k}}^* \hat{\beta}_{m,-\mathbf{k}}^\dagger, \quad \hat{b}_{m,\mathbf{k}}^\dagger = u_{m,-\mathbf{k}}^* \hat{\beta}_{m,-\mathbf{k}}^\dagger + v_{m,\mathbf{k}} \hat{\beta}_{m,\mathbf{k}}, \quad m \in \{1, 2\}, \quad (2.58)$$

where we have introduced the Fourier transformation of the fluctuation operators  $\hat{b}_{1,i}$  and  $\hat{b}_{2,i}$ ,

$$\hat{b}_{m,i}^\dagger = \frac{1}{\sqrt{M}} \sum_{\mathbf{k} \in \Lambda_0} \hat{b}_{m,\mathbf{k}}^\dagger e^{-i\mathbf{k} \cdot \mathbf{r}_i}, \quad \hat{b}_{m,i} = \frac{1}{\sqrt{M}} \sum_{\mathbf{k} \in \Lambda_0} \hat{b}_{m,\mathbf{k}} e^{i\mathbf{k} \cdot \mathbf{r}_i}, \quad m \in \{1, 2\}.$$

The notation  $\sum_{\mathbf{k} \in \Lambda_0}$  denotes that the momentum  $\mathbf{k}$  runs over the cubic-shaped first Brillouin zone  $\Lambda_0 \equiv [-\pi, \pi]^3$ . The free coefficients of rotation,  $u_{m,\mathbf{k}}$  and  $v_{m,\mathbf{k}}$ , should satisfy a condition  $|u_{m,\mathbf{k}}|^2 - |v_{m,\mathbf{k}}|^2 = 1$ . Then, the new operator  $\hat{\beta}_{m,\mathbf{k}}$  fulfills the canonical commutation relation  $[\hat{\beta}_{m,\mathbf{k}}, \hat{\beta}_{m',\mathbf{k}'}^\dagger] = \delta_{m,m'} \delta_{\mathbf{k},\mathbf{k}'}$ . When we choose the coefficients such that

$$u_{1,\mathbf{k}} = \sqrt{\frac{2 - u^2 \gamma_{\mathbf{k}}}{4 \sqrt{1 - u^2 \gamma_{\mathbf{k}}}}} + \frac{1}{2}, \quad v_{1,\mathbf{k}} = \text{sgn}(\gamma_{\mathbf{k}}) \sqrt{\frac{2 - u^2 \gamma_{\mathbf{k}}}{4 \sqrt{1 - u^2 \gamma_{\mathbf{k}}}}} - \frac{1}{2}, \quad (2.59)$$

$$u_{2,\mathbf{k}} = \sqrt{\frac{2 - \gamma_{\mathbf{k}}}{4 \sqrt{1 - \gamma_{\mathbf{k}}}}} + \frac{1}{2}, \quad v_{2,\mathbf{k}} = -\text{sgn}(\gamma_{\mathbf{k}}) \sqrt{\frac{2 - \gamma_{\mathbf{k}}}{4 \sqrt{1 - \gamma_{\mathbf{k}}}}} - \frac{1}{2}, \quad (2.60)$$

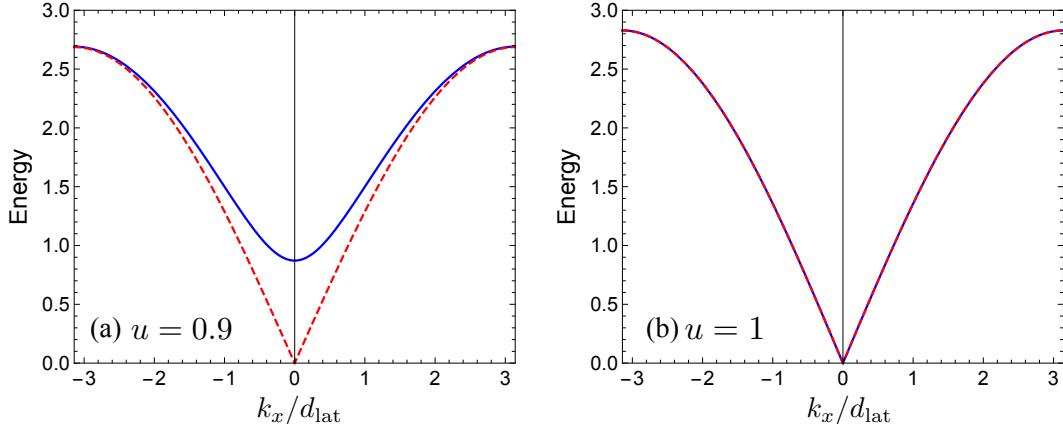


Figure 2.3: Higgs (blue-solid) and NG (red-dashed) energy dispersions at the high-filling limit. The vertical axis represents the energy dispersions ( $Jn_{0z} = 1$ ), whereas the horizontal axis does the wave-number vector at one dimension ( $d_{\text{lat}} = 1$ ). Two different results are calculated at (a)  $u = 0.9$  and (b)  $u = 1$ , respectively.

where  $\text{sgn}(x)$  is the sign function, then the quadratic Hamiltonian reads a diagonalized form

$$\hat{\mathcal{H}}_{\text{eff}}^{n_0 \gg 1} \approx \text{const.} + \sum_{m=1,2} \sum_{\mathbf{k} \in \Lambda_0} \mathcal{E}_{m,\mathbf{k}} \hat{\beta}_{m,\mathbf{k}}^\dagger \hat{\beta}_{m,\mathbf{k}}. \quad (2.61)$$

The band dispersions  $\mathcal{E}_{1,\mathbf{k}}$  (Higgs) and  $\mathcal{E}_{2,\mathbf{k}}$  (NG) are given by

$$\mathcal{E}_{1,\mathbf{k}} = 2Jn_{0z} \sqrt{1 - u^2 \gamma_{\mathbf{k}}}, \quad \mathcal{E}_{2,\mathbf{k}} = Jn_{0z}(1 + u) \sqrt{1 - \gamma_{\mathbf{k}}}, \quad (2.62)$$

where  $\gamma_{\mathbf{k}} = \sum_{i=1}^d \cos(k_i d_{\text{lat}})/d$ . Figure 2.3 depicts the energy dispersions as a function of  $\mathbf{k}$  at one dimension ( $d = 1$ ). As shown in Fig. 2.3(a), the Higgs dispersion has a finite energy gap  $\tilde{\Delta} = 2Jn_{0z} \sqrt{1 - u^2}$  at  $\mathbf{k} = 0$  (apart from  $u = u_c = 1$ ) while the NG one is gapless at that point. Moreover, it is clearly seen that at the critical point  $u = u_c = 1$ , the energy gap  $\tilde{\Delta}$  closes and these dispersions coincide with each other.

Similarly, we can derive the energy dispersion of the particle-hole excitations in the Mott-insulator state. To do that, we expand  $\hat{t}_{0,i}$  in  $\hat{t}_{1,i}$  and  $\hat{t}_{-1,i}$  via the constraint  $\sum_m \hat{t}_m^\dagger \hat{t}_m = \hat{1}$  within the quadratic order, i.e.,

$$\begin{aligned} \hat{t}_{0,i} &= \sqrt{1 - \hat{t}_{1,i}^\dagger \hat{t}_{1,i} - \hat{t}_{-1,i}^\dagger \hat{t}_{-1,i}} \\ &\approx 1 - \frac{1}{2} \hat{t}_{1,i}^\dagger \hat{t}_{1,i} - \frac{1}{2} \hat{t}_{-1,i}^\dagger \hat{t}_{-1,i} + \dots \end{aligned} \quad (2.63)$$

The diagonalization of the resulting quadratic Hamiltonian is also simple because the particle and hole sectors are completely decoupled. After simple calculations based on the Bogoliubov

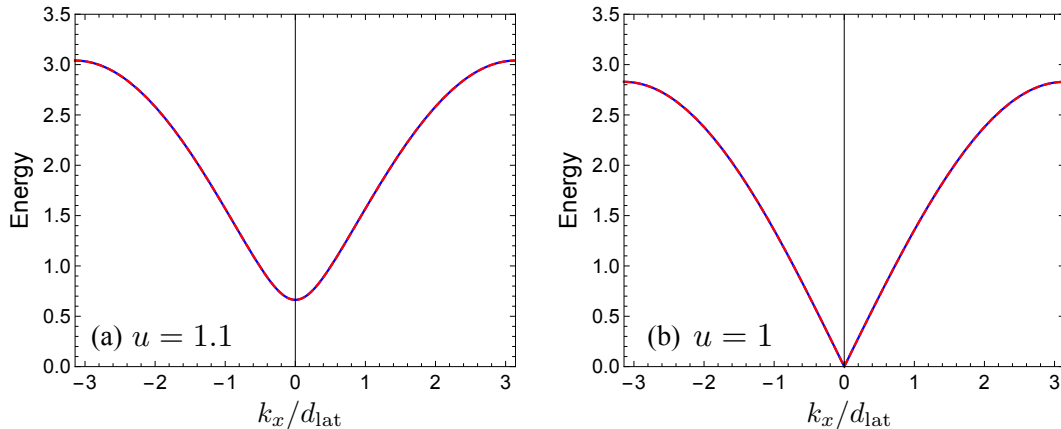


Figure 2.4: Particle (blue-solid) and hole (red-dashed) energy dispersions at the high-filling limit. The vertical axis represents the energy dispersions ( $Jn_{0z} = 1$ ), whereas the horizontal axis does the wave-number vector at one dimension ( $d_{\text{lat}} = 1$ ). Two different results are calculated at (a)  $u = 1.1$  and (b)  $u = 1$ , respectively.

transformation, we finally obtain the particle and hole dispersions [26],  $\hbar\omega_p$  and  $\hbar\omega_h$ , written as

$$\hbar\omega_p = \hbar\omega_h = \frac{U}{2} \sqrt{1 - u^{-1}\gamma_{\mathbf{k}}}. \quad (2.64)$$

These dispersions have an entirely same form due to the commensurate filling ( $B = 0$ ). In Fig. 2.4, we show  $\hbar\omega_p$  and  $\hbar\omega_h$  as a function of  $\mathbf{k}$  at one dimension. For  $u > u_c$ , the excitation energies have a finite gap corresponding to the incompressibility of the Mott-insulator phase [Fig. 2.4(a)]. In contrast, the gap vanishes at  $u = u_c = 1$  [Fig. 2.4(b)].

Within the quadratic approximation of the HP expansion, the Higgs and NG modes can be regarded as well-defined eigenstates because there is no transition among different levels. However, including further contributions of the expansion, these modes are able to attenuate into other non-perturbed states with certain decay rates. The stability of the Higgs mode against quantum and thermal fluctuations mediated by the interactions are studied in Chap. 4. There, we apply the HP expansion to the high and low filling effective models respectively in order to analyze some response functions to external perturbations.

# Chapter 3

## Phase space methods for quantum dynamics

In this chapter, we review the phase-space method, which represents quantum systems using classical phase-space variables and quasi-probability distribution functions. In Sec. 3.1, we provide a general overview of the phase-space method and introduce the Wigner function for a quantum state and the Wigner–Weyl transform of some operators, especially in the coordinate-momentum phase space. In Sec. 3.2, we formulate the phase-space representation of Bose fields using the Wigner function spanned by the coherent-state basis. In Sec. 3.3, we represent quantum dynamics of Bose fields by means of the time-dependent Wigner function and discuss the truncated-Wigner semiclassical approximation through two different ways.

### 3.1 Introduction

Phase-space representation of quantum systems provides a useful and interesting way to express general quantum states of quantized particles or fields using a distribution function in a classical phase space. For instance, a single-particle quantum state described by a density operator  $\hat{\rho}$  can be represented by using a Wigner function [122], which is a distribution function defined in the coordinate-momentum phase space  $(x, p) \in \mathbb{R}^2$ :

$$W(x, p) = \int_{-\infty}^{\infty} dy \left\langle x - \frac{y}{2} \left| \hat{\rho} \right| x + \frac{y}{2} \right\rangle e^{\frac{i}{\hbar} p y}, \quad (3.1)$$

where  $|x\rangle$  ( $\langle x|$ ) is a ket (bra) vector with a position  $x$ . Unlike standard distribution functions encountered in classical statistical mechanics, the Wigner function is not positive definite. Therefore, that is often termed a quasi-probability distribution function (for reviews of the Wigner function, see e.g. Refs. [47, 49, 123, 124]).

The Wigner function allows us to express the quantum average of arbitrary operators using

entirely classical objects. Let us consider the quantum average of an arbitrary operator  $\hat{\Omega}(\hat{x}, \hat{p})$  with respect to the density operator  $\hat{\rho}$ , which is given by

$$\langle \hat{\Omega}(\hat{x}, \hat{p}) \rangle = \text{Tr} \{ \hat{\rho} \hat{\Omega}(\hat{x}, \hat{p}) \}. \quad (3.2)$$

This can be represented as a phase-space integration form where a classical function corresponding to  $\hat{\Omega}(\hat{x}, \hat{p})$  is weighted with the coordinate-momentum Wigner function [123]:

$$\langle \hat{\Omega}(\hat{x}, \hat{p}) \rangle = \frac{1}{2\pi\hbar} \int dx dp W(x, p) \Omega_W(x, p). \quad (3.3)$$

Here, the classical function  $\Omega_W(x, p)$  is referred to as the Wigner–Weyl transform [123] of  $\hat{\Omega}(\hat{x}, \hat{p})$  (a.k.a. Weyl symbol) defined by

$$\Omega_W(x, p) = \int_{-\infty}^{\infty} dy \left\langle x - \frac{y}{2} \left| \hat{\Omega} \right| x + \frac{y}{2} \right\rangle e^{\frac{i}{\hbar} p y}. \quad (3.4)$$

Notice that the Wigner function is nothing but the Weyl symbol of the density operator  $\hat{\rho}$ . The Weyl symbol is closely related with the Weyl-ordering rule for operator products of  $\hat{x}$  and  $\hat{p}$  [49, 125]. The above discussion for the single particle can be generalized into multi-particle cases straightforwardly.

In the so called Wigner (or Wigner–Weyl) representation based on the quasi-probability distribution function, the dynamics of the density operator in the Hilbert space is translated into that of the Wigner function in the phase space [123]. The corresponding phase-space equation follows from an important quantity, i.e., the Moyal bracket [126]. For two arbitrary operators  $\hat{A}$  and  $\hat{B}$ , the Moyal bracket is defined by

$$\{A_W, B_W\}_{\text{M.B.}} = \frac{2}{\hbar} A_W(x, p) \sin \left[ \frac{\hbar}{2} \Lambda_{cm} \right] B_W(x, p), \quad (3.5)$$

where

$$\Lambda_{cm} = \frac{\overleftarrow{\partial}}{\partial x} \frac{\overrightarrow{\partial}}{\partial p} - \frac{\overleftarrow{\partial}}{\partial p} \frac{\overrightarrow{\partial}}{\partial x} \quad (3.6)$$

is the symplectic operator in the coordinate-momentum space. If we take a classical limit  $\hbar \rightarrow 0$ , it is reduced to the standard Poisson bracket. As we will see later, the Moyal bracket is nothing but the Weyl symbol of an operator product  $\hat{A}\hat{B}$ , i.e.,  $(\hat{A}\hat{B})_W(x, p)$ . Using the Moyal bracket, we can write down the equation of motion of the Wigner function as follows:

$$\begin{aligned} i\hbar \frac{\partial W}{\partial t} &= \{H_W, W\}_{\text{M.B.}} \\ &= \frac{2}{\hbar} H_W \sin \left[ \frac{\hbar}{2} \Lambda_{cm} \right] W, \end{aligned} \quad (3.7)$$

where  $H_W$  is a classical function mapped from a Hamiltonian operator through the Wigner–Weyl transform.

A similar representation by use of the Wigner function can be made for a system of Bose fields describing, e.g., photons or bosonic atoms [47, 124]. There, it is convenient to span the phase-space distribution function by means of the coherent state basis [123, 127]. The coherent state introduces a complex classical field as a phase-space variable. Such a complex field corresponds to a natural classical limit of Bose fields. The time evolution of the coherent-state Wigner function is described by a similar equation to Eq. (3.7) [49].

Our main purpose of this chapter is to provide the coherent-state Wigner representation of general Bose fields and show how to utilize it for describing quantum dynamics of the systems. In particular, we focus on a useful fact that within a semiclassical regime one can diminish the computational difficulty in simulating the quantum dynamics. Indeed, when the system is in a nearly classical limit, the dynamics of the system can be approximated by deterministic Gross–Pitaevskii trajectories of the classical field, whose initial conditions are weighted with the initial Wigner function. This treatment is often referred to as the truncated-Wigner approximation (TWA) in quantum optics and other fields [48, 49]. Since the number of the classical equations of motion is proportional to the total mode number or system size, the TWA can be applied even to macroscopic quantum many-body systems, to which exact numerical methods are inaccessible due to the exponentially-large Hilbert space.

In the past two decades, TWA or related semiclassical frameworks were widely used to explore non-equilibrium phenomena of isolated Bose gases trapped by optical lattices [27, 31, 49–51, 128–137], quantum spin systems [49, 63, 119, 138, 139], open quantum systems [124, 140–144], spin-boson models [145–147], and interacting fermions [148–150]. In earlier literatures on interacting bosons in optical lattices [27, 31, 50, 51, 134, 136], it was argued that in a weakly interacting regime the semiclassical approach can be used to describe the time evolution induced by a sudden quench from a Mott-insulator state. However, the application of such semiclassical approaches to the three-dimensional (3D) case at unit filling, which is the situation realized in the experiment [35, 36], has not been demonstrated in practice. One of the goals of this thesis is to apply a TWA method, which was previously used to study dynamics of the one-dimensional (1D) Bose–Hubbard at a large-filling factor [27, 50, 51], to the experimental setup of Ref. [35, 36] that the 3D Bose–Hubbard model is quenched from a singly-occupied Mott-insulator state. The details of the numerical simulation and direct comparison with the experimental data will be presented in Chap. 5.

## 3.2 Wigner representation of Bose fields

### 3.2.1 Coherent-state phase space representation

Let us consider a single-mode Bose field described by boson annihilation and creation operators,  $\hat{a}$  and  $\hat{a}^\dagger$ . An important step to build up a phase-space representation of the Bose field is to introduce the coherent state [127], which is given by

$$|\alpha\rangle = \hat{D}(\alpha)|0\rangle, \quad \langle\alpha| = \langle 0|\hat{D}^\dagger(\alpha) = \langle 0|\hat{D}(-\alpha), \quad (3.8)$$

where  $\alpha \in \mathbb{C}$  is a complex number,  $\hat{D}(\alpha) = e^{\alpha\hat{a}^\dagger - \alpha^*\hat{a}}$  is the so called displacement operator [124], and  $|0\rangle$  represents the vacuum state of the Bose field. This vector is normalized as  $\langle\alpha|\alpha\rangle = 1$ . The displacement operator is a unitary operator, and it yields a unitary transformation that adds an offset to the canonical field operators such that  $\hat{a} \rightarrow \hat{a} + \alpha$ , hence,

$$\hat{D}^\dagger(\alpha)\hat{a}\hat{D}(\alpha) = \hat{a} + \alpha, \quad \hat{D}^\dagger(\alpha)\hat{a}^\dagger\hat{D}(\alpha) = \hat{a}^\dagger + \alpha^*. \quad (3.9)$$

Because of this property, the coherent state is found to be a right (left) eigenstate of the field operator  $\hat{a}$  ( $\hat{a}^\dagger$ ),

$$\hat{a}|\alpha\rangle = \alpha|\alpha\rangle, \quad \langle\alpha|\hat{a}^\dagger = \alpha^*\langle\alpha|, \quad (3.10)$$

and the number  $\alpha$  gives the resulting complex eigenvalues. This vector produces an over-complete basis to span the Hilbert space and satisfies a completeness relation

$$\int \frac{d^2\alpha}{\pi} |\alpha\rangle\langle\alpha| = \hat{1}, \quad (3.11)$$

where  $d^2\alpha/\pi \equiv d\text{Re}[\alpha] d\text{Im}[\alpha]/\pi$ . The conjugated pair  $(\alpha, \alpha^*)$  of the coherent-state index plays a role of natural phase-space variables for the Bose field in the following discussions.

The coherent state basis makes up key ingredients for representing the Bose field using phase-space variables, i.e., the Weyl symbol of operators and Wigner function for quantum states. For the single-mode Bose field, the Weyl symbol of an arbitrary operator  $\hat{\Omega} = \hat{\Omega}(\hat{a}, \hat{a}^\dagger)$  can be defined as

$$\Omega_W(\alpha, \alpha^*) = \frac{1}{2} \int d\eta d\eta^* \left\langle \alpha - \frac{\eta}{2} \left| \hat{\Omega} \left| \alpha + \frac{\eta}{2} \right. \right. \right\rangle e^{\frac{1}{2}(\eta^*\alpha - \alpha^*\eta)}, \quad (3.12)$$

where  $d\alpha d\alpha^* = d^2\alpha/\pi$ . When we insert a density operator  $\hat{\rho}$  into  $\hat{\Omega}$ , it results in the corresponding Wigner function

$$W(\alpha, \alpha^*) = \frac{1}{2} \int d\eta d\eta^* \left\langle \alpha - \frac{\eta}{2} \left| \hat{\rho} \left| \alpha + \frac{\eta}{2} \right. \right. \right\rangle e^{\frac{1}{2}(\eta^*\alpha - \alpha^*\eta)}. \quad (3.13)$$

Using these classical functions, the quantum average of  $\hat{\Omega}$  with respect to  $\hat{\rho}$ , i.e.,  $\langle \hat{\Omega} \rangle = \text{Tr}[\hat{\rho}\hat{\Omega}]$ , can be written as

$$\langle \hat{\Omega} \rangle = \int d\alpha d\alpha^* \Omega_W(\alpha, \alpha^*) W(\alpha, \alpha^*). \quad (3.14)$$

This equation corresponds to Eq. (3.3) in the coordinate-momentum representation. The detailed derivation of Eq. (3.14) will be given in Sec. 3.2.4.

The multi-mode generalization of Eqs. (3.12), (3.13), and (3.14) is straightforward: When the Bose field possesses an  $M$ -number of distinct modes, then the corresponding Weyl symbol and Wigner function are generalized into

$$\Omega_W(\vec{\alpha}, \vec{\alpha}^*) = \frac{1}{2^M} \int d\vec{\eta}^* d\vec{\eta} \left\langle \vec{\alpha} - \frac{\vec{\eta}}{2} \left| \hat{\Omega} \right| \vec{\alpha} + \frac{\vec{\eta}}{2} \right\rangle e^{\frac{1}{2}(\vec{\eta}^* \cdot \vec{\alpha} - \vec{\alpha}^* \cdot \vec{\eta})}, \quad (3.15)$$

$$W(\vec{\alpha}, \vec{\alpha}^*) = \frac{1}{2^M} \int d\vec{\eta}^* d\vec{\eta} \left\langle \vec{\alpha} - \frac{\vec{\eta}}{2} \left| \hat{\rho} \right| \vec{\alpha} + \frac{\vec{\eta}}{2} \right\rangle e^{\frac{1}{2}(\vec{\eta}^* \cdot \vec{\alpha} - \vec{\alpha}^* \cdot \vec{\eta})}, \quad (3.16)$$

where  $\vec{\alpha} = (\alpha_1, \alpha_2, \dots, \alpha_M)$  indicates a point in the  $2M$ -dimensional phase space and  $d\vec{\eta}d\vec{\eta}^* = \prod_{i=1}^M d\eta_i d\eta_i^* = \prod_{i=1}^M [d^2\eta_i/\pi]$ . The multiple coherent state  $|\vec{\alpha}\rangle$  is written as a product state of the single-mode coherent state:

$$|\vec{\alpha}\rangle = \hat{D}_1(\alpha_1)\hat{D}_2(\alpha_2)\cdots\hat{D}_M(\alpha_M)|0, 0, \dots, 0\rangle = \bigotimes_{i=1}^M \hat{D}_i(\alpha_i)|0\rangle, \quad (3.17)$$

where  $\hat{D}_i(\alpha_i) \equiv e^{\alpha_i \hat{a}_i^\dagger - \alpha_i^* \hat{a}_i}$  and  $[\hat{D}_i(\alpha_i), \hat{D}_j(\alpha_j)] = 0$  for  $i \neq j$ . Thus, we obtain a general formula of the phase-space averaging:

$$\langle \hat{\Omega} \rangle = \int d\vec{\alpha} d\vec{\alpha}^* \Omega_W(\vec{\alpha}, \vec{\alpha}^*) W(\vec{\alpha}, \vec{\alpha}^*). \quad (3.18)$$

### 3.2.2 Weyl symbols and Weyl ordering

To illustrate the mapping of Eq. (3.12) from operators to classical functions, we calculate Weyl symbols of operators in practice. First, let us consider an operator where the canonical pairs are decoupled such that  $\hat{\Omega}(\hat{a}, \hat{a}^\dagger) = A(\hat{a}) + B(\hat{a}^\dagger)$ . When we choose  $A(x) = ax^n$  and  $B(x) = bx^m$ , the corresponding Weyl symbol is given as

$$(\hat{\Omega})_W(\alpha, \alpha^*) = a\alpha^n + b(\alpha^*)^m. \quad (3.19)$$

Indeed, it can be confirmed that

$$\begin{aligned}
[\hat{a}^n]_W(\alpha, \alpha^*) &= \frac{1}{2} \int \frac{d^2\eta}{\pi} \left\langle \alpha - \frac{\eta}{2} \left| \hat{a}^n \right| \alpha + \frac{\eta}{2} \right\rangle e^{\frac{1}{2}(\eta^* \alpha - \alpha^* \eta)} \\
&= \frac{1}{2} \int \frac{d^2\eta}{\pi} \left( \alpha + \frac{\eta}{2} \right)^n e^{-\frac{1}{2}|\eta|^2} \\
&= \alpha^n, \\
[(\hat{a}^\dagger)^m]_W(\alpha, \alpha^*) &= \frac{1}{2} \int \frac{d^2\eta}{\pi} \left( \alpha^* - \frac{\eta^*}{2} \right)^m e^{-\frac{1}{2}|\eta|^2} \\
&= (\alpha^*)^m.
\end{aligned}$$

To calculate them, we have used two relations, i.e., the overlap between  $|\alpha\rangle$  and  $|\beta\rangle$

$$\langle \alpha | \beta \rangle = e^{-\frac{1}{2}|\alpha|^2 - \frac{1}{2}|\beta|^2 + \alpha^* \beta}, \quad (3.20)$$

and a set of Gaussian integrals,

$$[1]_\eta = 1, \quad [|\eta|^n]_\eta = 2^n n!, \quad [\eta^n]_\eta = [(\eta^*)^m]_\eta = 0, \quad (3.21)$$

where  $[f(\eta, \eta^*)]_\eta = \frac{1}{2} \int \frac{d^2\eta}{\pi} f(\eta, \eta^*) e^{-\frac{1}{2}|\eta|^2}$ . Thus, for the decoupled operators, the Weyl symbol can be obtained from replacing the canonical operators with corresponding classical numbers:  $(\hat{a}, \hat{a}^\dagger) \rightarrow (\alpha, \alpha^*)$ .

The same operational manual based on such a replacement is also true when the operator of interest is fully symmetrized with respect to the canonical variables. To see that, let us consider a symmetrized operator

$$\frac{\hat{a}^\dagger \hat{a} + \hat{a} \hat{a}^\dagger}{2}. \quad (3.22)$$

Using Eqs. (3.12), (3.20), and (3.21), we find that the resulting Weyl symbol coincides with the classical number obtained from the replacement into Eq. (3.22):

$$\frac{1}{2} [\hat{a}^\dagger \hat{a} + \hat{a} \hat{a}^\dagger]_W(\alpha, \alpha^*) = \alpha^* \alpha. \quad (3.23)$$

This property implies the standard Weyl-ordering rule of operators that a product constructed from some phase-space variables correspond to a fully-symmetrized product of corresponding operators.

In contrast, if Eq. (3.22) is not symmetrized, for instance, if it is written as  $\hat{a}^\dagger \hat{a}$  or  $\hat{a} \hat{a}^\dagger$ , then, there arises a constant factor in addition to  $\alpha^* \alpha$ :

$$[\hat{a}^\dagger \hat{a}]_W(\alpha, \alpha^*) = \alpha^* \alpha - \frac{1}{2}, \quad [\hat{a} \hat{a}^\dagger]_W(\alpha, \alpha^*) = \alpha^* \alpha + \frac{1}{2}. \quad (3.24)$$

The factors follow from the non-commutativity of the canonical variables  $[\hat{a}, \hat{a}^\dagger] = 1$ . Indeed, when we rewrite them as a fully symmetrized form, and perform the replacement, the same results are recovered such that

$$\begin{aligned}\hat{a}^\dagger \hat{a} &= \frac{\hat{a}^\dagger \hat{a} + \hat{a} \hat{a}^\dagger}{2} + \frac{1}{2}[\hat{a}^\dagger, \hat{a}] \rightarrow \alpha^* \alpha - \frac{1}{2}, \\ \hat{a} \hat{a}^\dagger &= \frac{\hat{a}^\dagger \hat{a} + \hat{a} \hat{a}^\dagger}{2} + \frac{1}{2}[\hat{a}, \hat{a}^\dagger] \rightarrow \alpha^* \alpha + \frac{1}{2}.\end{aligned}$$

### 3.2.3 Moyal products and Bopp operators

In the coherent-state phase space, we can also define the Moyal product between two classical functions. For arbitrary operators  $\hat{A}$  and  $\hat{B}$ , the Weyl symbol  $(\hat{A}\hat{B})_W$  is expressed by [49]:

$$(\hat{A}\hat{B})_W(\alpha, \alpha^*) \equiv A_W(\alpha, \alpha^*) \exp\left[\frac{1}{2}\Lambda_c\right] B_W(\alpha, \alpha^*) \quad (3.25)$$

$$= B_W(\alpha, \alpha^*) \exp\left[-\frac{1}{2}\Lambda_c\right] A_W(\alpha, \alpha^*), \quad (3.26)$$

where  $\Lambda_c$  is the symplectic operator in the coherent phase space, given by

$$\Lambda_c = \frac{\overleftarrow{\partial}}{\partial\alpha} \frac{\overrightarrow{\partial}}{\partial\alpha^*} - \frac{\overleftarrow{\partial}}{\partial\alpha^*} \frac{\overrightarrow{\partial}}{\partial\alpha}. \quad (3.27)$$

The symplectic operator provides the Poisson bracket in the complex phase space between  $A_W(\alpha, \alpha^*)$  and  $B_W(\alpha, \alpha^*)$ :

$$A_W \Lambda_c B_W = \frac{\partial A_W}{\partial\alpha} \frac{\partial B_W}{\partial\alpha^*} - \frac{\partial A_W}{\partial\alpha^*} \frac{\partial B_W}{\partial\alpha} = \{A_W, B_W\}_{\text{P.B.}}. \quad (3.28)$$

Using the Moyal product (3.26), it is easy to obtain again the result of Eq. (3.24):

$$\begin{aligned}(\hat{a}^\dagger \hat{a})_W(\alpha, \alpha^*) &= \alpha^* \left[1 + \frac{1}{2}\Lambda_c + \dots\right] \alpha = \alpha^* \alpha - \frac{1}{2}, \\ (\hat{a} \hat{a}^\dagger)_W(\alpha, \alpha^*) &= \alpha \left[1 + \frac{1}{2}\Lambda_c + \dots\right] \alpha^* = \alpha^* \alpha + \frac{1}{2}.\end{aligned}$$

The Moyal product defines the Moyal bracket, which is equivalent to the Weyl symbol of a commutator  $[\hat{A}, \hat{B}]$ . Using Eq. (3.26), it is given by

$$\{A_W, B_W\}_{\text{M.B.}} \equiv ([\hat{A}, \hat{B}])_W = 2A_W \sinh\left[\frac{1}{2}\Lambda_c\right] B_W. \quad (3.29)$$

If we take a classical limit, the Moyal bracket reduces to the Poisson bracket. This limit is formally equivalent to eliminating higher-order terms of expansion of Eq. (3.29) in  $\Lambda_c$ .

It is also possible to calculate Weyl symbols using Bopp operators for the canonical variables [49, 124]. For the Bose operators  $\hat{a}$  and  $\hat{a}^\dagger$ , the corresponding right-derivative Bopp operators are introduced as

$$\hat{a} \rightarrow \alpha + \frac{1}{2} \frac{\partial}{\partial \alpha^*}, \quad \hat{a}^\dagger \rightarrow \alpha^* - \frac{1}{2} \frac{\partial}{\partial \alpha}. \quad (3.30)$$

Using the Bopp operators, the Weyl symbols of  $\hat{a}^\dagger \hat{a}$  and  $\hat{a} \hat{a}^\dagger$  are calculated as follows:

$$\begin{aligned} \hat{a}^\dagger \hat{a} \hat{1} &\rightarrow \left( \alpha^* - \frac{1}{2} \frac{\partial}{\partial \alpha} \right) \left( \alpha + \frac{1}{2} \frac{\partial}{\partial \alpha^*} \right) 1 = \alpha^* \alpha - \frac{1}{2}, \\ \hat{a} \hat{a}^\dagger \hat{1} &\rightarrow \left( \alpha + \frac{1}{2} \frac{\partial}{\partial \alpha^*} \right) \left( \alpha^* - \frac{1}{2} \frac{\partial}{\partial \alpha} \right) 1 = \alpha^* \alpha + \frac{1}{2}. \end{aligned}$$

Moreover, we can write down left-derivative Bopp operators instead of the right-derivative ones, which are given by

$$\hat{a} \rightarrow \alpha - \frac{1}{2} \overleftarrow{\frac{\partial}{\partial \alpha^*}}, \quad \hat{a}^\dagger \rightarrow \alpha^* + \frac{1}{2} \overleftarrow{\frac{\partial}{\partial \alpha}}. \quad (3.31)$$

A similar calculation is performed as follows:

$$\begin{aligned} \hat{1} \hat{a}^\dagger \hat{a} &\rightarrow 1 \left( \alpha^* + \frac{1}{2} \overleftarrow{\frac{\partial}{\partial \alpha^*}} \right) \left( \alpha - \frac{1}{2} \overleftarrow{\frac{\partial}{\partial \alpha}} \right) = \alpha^* \alpha - \frac{1}{2}, \\ \hat{1} \hat{a} \hat{a}^\dagger &\rightarrow 1 \left( \alpha - \frac{1}{2} \overleftarrow{\frac{\partial}{\partial \alpha^*}} \right) \left( \alpha^* + \frac{1}{2} \overleftarrow{\frac{\partial}{\partial \alpha}} \right) = \alpha^* \alpha + \frac{1}{2}. \end{aligned}$$

It is important to note that the Bopp-operator replacement is valid for the time-dependent Heisenberg operators within a semiclassical limit (see Ref. [49]). The time-dependent Bopp operator is very useful to derive semiclassical representations of non-equal time correlation functions of the field operators.

### 3.2.4 Displacement operator expansion

It is convenient to expand an arbitrary operator  $\hat{A}$  with respect to the displacement operator  $\hat{D}(\alpha)$  [123, 151] as

$$\hat{A} = \int \frac{d^2 \alpha}{\pi} \chi_A(\alpha) \hat{D}(\alpha), \quad (3.32)$$

in which the coefficient  $\chi_A(\alpha)$  is referred to as the characteristic function of  $\hat{A}$ . Since the displacement operator satisfies relations

$$\hat{D}(\alpha) \hat{D}(\beta) = e^{\frac{1}{2}(\alpha \beta^* - \alpha^* \beta)} \hat{D}(\alpha + \beta), \quad (3.33)$$

$$\text{Tr}[\hat{D}(\alpha) \hat{D}(\beta)] = \pi \delta^{(2)}(\alpha + \beta), \quad (3.34)$$

the characteristic function is given by

$$\chi_A(\alpha) = \text{Tr} [\hat{A} \hat{D}^\dagger(\alpha)]. \quad (3.35)$$

Here we introduced the delta function in the complex plane given by

$$\delta^{(2)}(\alpha) = \frac{1}{\pi} \int \frac{d^2\xi}{\pi} e^{\alpha\xi^* - \xi\alpha^*}. \quad (3.36)$$

Notice that this expansion is similar with the usual expansion of a vector in a linear space with respect to an adequate basis. In particular, the trace operation implies an inner product between two *vectors*  $\hat{D}(\alpha)$  and  $\hat{D}^\dagger(\beta)$ .

Starting from the displacement operator expansion (3.32), we can derive the phase-space representations in the previous subsections, which were given with no proof, and some useful formulae. Let us consider the Weyl symbol of Eq. (3.32):

$$A_W(\alpha) = \int \frac{d^2\xi}{\pi} \chi_A(\xi) [\hat{D}(\xi)]_W(\alpha). \quad (3.37)$$

The Weyl symbol of  $\hat{D}(\xi)$  can be obtained from replacing the field operators with the corresponding complex numbers because the operator is written as a Weyl-ordered form. Therefore,  $A_W(\alpha)$  reads

$$A_W(\alpha) = \int \frac{d^2\beta}{\pi} \chi_A(\beta) e^{\beta\alpha^* - \beta^*\alpha}. \quad (3.38)$$

If we substitute Eq. (3.32) into Eq. (3.12), we are able to obtain again this result. Indeed, it is checked that

$$\begin{aligned} A_W(\alpha) &= \frac{1}{2} \int \frac{d^2\eta}{\pi} \frac{d^2\xi}{\pi} \chi_A(\xi) \left\langle \alpha - \frac{\eta}{2} \left| \hat{D}(\xi) \right| \alpha + \frac{\eta}{2} \right\rangle e^{\frac{1}{2}(\eta^*\alpha - \alpha^*\eta)} \\ &= \frac{1}{2} \int \frac{d^2\eta}{\pi} \frac{d^2\xi}{\pi} \chi_A(\xi) e^{\xi\alpha^* - \xi^*\alpha - \frac{1}{2}|\eta + \xi|^2} \\ &= \frac{1}{2} \int \frac{d^2\xi}{\pi} \left[ \int \frac{d^2\eta}{\pi} e^{-\frac{1}{2}|\eta|^2 - \frac{1}{2}(\eta^*\xi + \xi^*\eta)} \right] e^{-\frac{1}{2}|\xi|^2} \chi_A(\xi) e^{\xi\alpha^* - \xi^*\alpha} \\ &= \int \frac{d^2\xi}{\pi} \chi_A(\xi) e^{\xi\alpha^* - \xi^*\alpha}. \end{aligned} \quad (3.39)$$

In the last equality, we have performed a complex Gauss integration with respect to  $\eta$  [see, e.g., Eq. (3.50)]. Therefore, Eq. (3.38) gives another definition of the Weyl symbol of operators.

Next we express the trace of two arbitrary operators,  $\text{Tr}[\hat{A}\hat{B}]$ , using the classical functions with

the phase-space integration. Substituting Eq. (3.32) into the expression, it is found that

$$\begin{aligned}\mathrm{Tr}[\hat{A}\hat{B}] &= \int \frac{d^2\alpha}{\pi} \frac{d^2\beta}{\pi} \chi_A(\alpha)\chi_B(\beta)\mathrm{Tr}[\hat{D}(\alpha)\hat{D}(\beta)] \\ &= \int \frac{d^2\alpha}{\pi} \frac{d^2\beta}{\pi} \chi_A(\alpha)\chi_B(\beta) \cdot \pi\delta^{(2)}(\alpha + \beta) \\ &= \int \frac{d^2\alpha}{\pi} A_W(\alpha)B_W(\alpha).\end{aligned}\quad (3.40)$$

If we select  $\hat{A} = \hat{\Omega}$  and  $\hat{B} = \hat{\rho}$ , then Eq. (3.14) is recovered. In addition, this relation allows the characteristic function  $\chi_A$  to be rewritten as a function of  $A_W$ :

$$\chi_A(\alpha) = \int \frac{d^2\xi}{\pi} A_W(\xi) e^{-\alpha\xi^* + \alpha^*\xi}.\quad (3.41)$$

Let us compute the Weyl symbol of a product  $\hat{A}\hat{B}$  of two arbitrary operators  $\hat{A}$  and  $\hat{B}$ . Using Eqs. (3.32), (3.36), and (3.40), it is performed that

$$\begin{aligned}(\hat{A}\hat{B})_W(\alpha) &= \int \frac{d^2\eta}{\pi} \frac{d^2\xi}{\pi} \chi_A(\eta)\chi_B(\xi)[\hat{D}(\eta)\hat{D}(\xi)]_W(\alpha) \\ &= \int \frac{d^2\eta}{\pi} \frac{d^2\xi}{\pi} \chi_A(\eta)\chi_B(\xi) e^{\frac{1}{2}(\eta\xi^* - \eta^*\xi)} e^{(\eta+\xi)\alpha^* - (\eta^* + \xi^*)\alpha} \\ &= \int \frac{d^2\eta}{\pi} \frac{d^2\xi}{\pi} \frac{d^2\alpha_0}{\pi} \frac{d^2\beta_0}{\pi} A_W(\alpha_0)B_W(\beta_0) e^{-\eta\alpha_0^* + \eta^*\alpha_0 - \xi\beta_0^* + \xi^*\beta_0} e^{\frac{1}{2}(\eta\xi^* - \eta^*\xi)} e^{(\eta+\xi)\alpha^* - (\eta^* + \xi^*)\alpha} \\ &= \int \frac{d^2\alpha_0}{\pi} \frac{d^2\eta}{\pi} A_W(\alpha_0)B_W(\alpha - \eta/2) e^{\eta(\alpha^* - \alpha_0^*) - \eta^*(\alpha - \alpha_0)}.\end{aligned}$$

Taking a transformation  $\eta \rightarrow -2\alpha_0 - \sigma + 2\alpha$  under the integration of  $\alpha_0$ , we obtain

$$(\hat{A}\hat{B})_W(\alpha) = \int \frac{d^2\alpha_0 d^2\sigma}{\pi^2} A_W(\alpha_0)B_W(\alpha_0 + \sigma/2) e^{\sigma^*(\alpha - \alpha_0) - \sigma(\alpha^* - \alpha_0^*)}.\quad (3.42)$$

It is also possible to express this equation such that  $\sigma$  appears in the argument of  $A_W(\alpha)$ :

$$(\hat{A}\hat{B})_W(\alpha) = \int \frac{d^2\alpha_0 d^2\sigma}{\pi^2} A_W(\alpha_0 - \sigma/2)B_W(\alpha_0) e^{\sigma^*(\alpha - \alpha_0) - \sigma(\alpha^* - \alpha_0^*)}.\quad (3.43)$$

Similarly, we can obtain the Weyl symbol of  $\hat{B}\hat{A}$ :

$$(\hat{B}\hat{A})_W(\alpha) = \int \frac{d^2\alpha_0 d^2\sigma}{\pi^2} A_W(\alpha_0 + \sigma/2)B_W(\alpha_0) e^{\sigma^*(\alpha - \alpha_0) - \sigma(\alpha^* - \alpha_0^*)},\quad (3.44)$$

$$= \int \frac{d^2\alpha_0 d^2\sigma}{\pi^2} A_W(\alpha_0)B_W(\alpha_0 - \sigma/2) e^{\sigma^*(\alpha - \alpha_0) - \sigma(\alpha^* - \alpha_0^*)}.\quad (3.45)$$

Thus, the permutation of  $\hat{A}$  and  $\hat{B}$  leads to the sign inversion of  $\sigma$  in the argument of  $A_W$  or  $B_W$ .

If we expand  $B_W(\alpha_0 + \sigma/2)$  with respect to  $\sigma$  such that

$$B_W(\alpha_0 + \sigma/2) = B_W(\alpha_0) + \frac{\sigma}{2} \frac{\partial B_W(\alpha_0)}{\partial \alpha_0} + \frac{\sigma^2}{2} \frac{\partial^2 B_W(\alpha_0)}{\partial \alpha_0^2} + \cdots, \quad (3.46)$$

then, Eq. (3.42) reads

$$\begin{aligned} (\hat{A}\hat{B})_W(\alpha) &= \sum_{n,m=0}^{\infty} \frac{(-1)^n}{2^{m+n} m! n!} \frac{\partial^{m+n} A_W(\alpha)}{\partial \alpha^m (\partial \alpha^*)^n} \frac{\partial^{m+n} B_W(\alpha)}{\partial \alpha^n (\partial \alpha^*)^m} \\ &= A_W(\alpha) \exp \left[ \frac{1}{2} \left( \overleftarrow{\frac{\partial}{\partial \alpha}} \overrightarrow{\frac{\partial}{\partial \alpha^*}} - \overleftarrow{\frac{\partial}{\partial \alpha^*}} \overrightarrow{\frac{\partial}{\partial \alpha}} \right) \right] B_W(\alpha). \end{aligned}$$

This is the derivation of the Moyal product given by Eq. (3.26). Furthermore, when  $\hat{A} = \hat{a}$  and  $\hat{B}$  is arbitrary, it follows from Eqs. (3.43) and (3.45) that

$$\begin{aligned} (\hat{a}\hat{B})_W(\alpha) &= \int \frac{d^2 \alpha_0 d^2 \sigma}{\pi^2} \left( \alpha_0 - \frac{\sigma}{2} \right) B_W(\alpha_0) e^{\sigma^*(\alpha - \alpha_0) - \sigma(\alpha^* - \alpha_0^*)} \\ &= \int \frac{d^2 \alpha_0 d^2 \sigma}{\pi^2} \left( \alpha_0 + \frac{1}{2} \frac{\partial}{\partial \alpha^*} \right) B_W(\alpha_0) e^{\sigma^*(\alpha - \alpha_0) - \sigma(\alpha^* - \alpha_0^*)} \\ &= \left( \alpha + \frac{1}{2} \frac{\partial}{\partial \alpha^*} \right) B_W(\alpha), \end{aligned} \quad (3.47)$$

$$(\hat{B}\hat{a})_W(\alpha) = \left( \alpha - \frac{1}{2} \frac{\partial}{\partial \alpha^*} \right) B_W(\alpha). \quad (3.48)$$

Hence, the Bopp operators introduced in Sec. 3.2.3 naturally arise from the simple starting point of Eq. (3.32).

### 3.2.5 Wigner functions

In the coherent-state basis, the Wigner function exists as a quasi-probability distribution function in the complex-number phase space. Here, we overview some examples of Wigner functions of Bose fields in the single-mode case. For reviews, see e.g. Refs. [47–49, 123, 124].

We start from the vacuum state denoted by  $\hat{\rho} = |0\rangle\langle 0|$ . Using Eq. (3.20), the Wigner function  $W_{\text{vac}} = (|0\rangle\langle 0|)_W$  reads

$$W_{\text{vac}}(\alpha, \alpha^*) = \frac{1}{2\pi} \int d^2 \eta e^{-|\alpha|^2 - \frac{1}{4} |\eta|^2} e^{\frac{1}{2} (\eta^* \alpha - \alpha^* \eta)}. \quad (3.49)$$

The integration with respect to  $\eta$  and  $\eta^*$  can be performed by using a useful relation [165]

$$\int d^2 z e^{-z^* w z + u^* z + z^* v} = \frac{\pi}{w} e^{\frac{u^* v}{w}}, \quad (3.50)$$

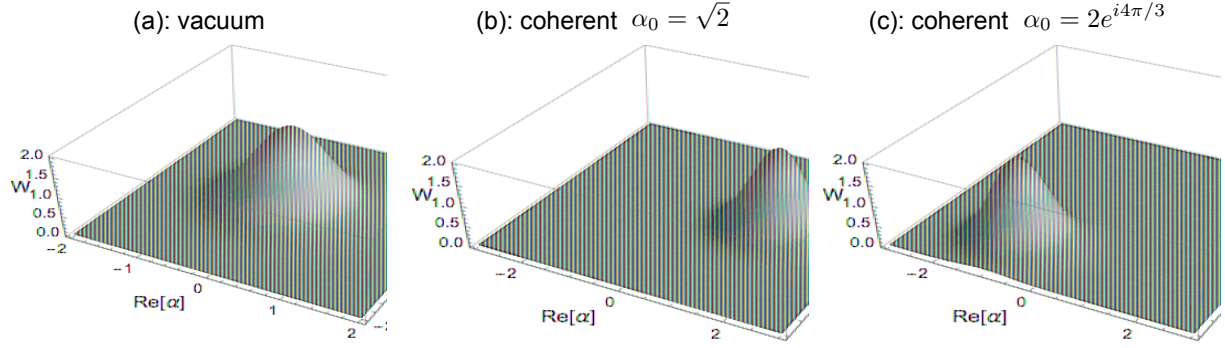


Figure 3.1: Wigner functions of (a) the vacuum state and the coherent states with (b)  $\alpha_0 = \sqrt{2}$  and (c)  $\alpha_0 = 2e^{i4\pi/3}$ .

where  $\text{Re}[w] > 0$  and  $u^*$  and  $v$  are independent complex numbers. Thus, we obtain a Gaussian-form Wigner function with the variance  $\sigma = 1/2$ :

$$W_{\text{vac}}(\alpha, \alpha^*) = 2e^{-2|\alpha|^2}. \quad (3.51)$$

As seen in Fig. 3.1(a), it describes the vacuum noise of the Bose field due to quantum fluctuations.

Similarly, we can also derive the Wigner function of the coherent state  $|\alpha_0\rangle = \hat{D}(\alpha_0)|0\rangle$ . The Weyl symbol of the density operator  $|\alpha_0\rangle\langle\alpha_0|$  is given by

$$W_{\alpha_0}(\alpha, \alpha^*) = 2e^{-2|\alpha - \alpha_0|^2}. \quad (3.52)$$

In Fig. 3.1, we show Eq. (3.52) with different values of  $\alpha_0$ . As expected from Eq. (3.8), the central position of this distribution is shifted to  $\alpha = \alpha_0$  compared with that of the vacuum Wigner function.

In contrast to the above examples, the Wigner function of Fock states can take negative values. Let us consider a  $N$ -particle Fock state given by

$$|N\rangle = \frac{1}{\sqrt{N!}}(\hat{a}^\dagger)^N|0\rangle. \quad (3.53)$$

Substituting  $|N\rangle\langle N|$  into the definition, the Wigner function is written as

$$W_N(\alpha, \alpha^*) = \frac{1}{2N!\pi} \int d^2\eta \left(\alpha^* - \frac{\eta^*}{2}\right)^N \left(\alpha + \frac{\eta}{2}\right)^N e^{-|\alpha|^2 - \frac{1}{4}|\eta|^2} e^{(\eta^*\alpha - \alpha^*\eta)/2}.$$

The exponential factor can be separated into two independent factors such that

$$\exp\left[-\frac{1}{4}|\eta|^2 + \frac{1}{2}(\eta^*\alpha - \alpha^*\eta)\right] = e^{-|\alpha|^2} \exp\left[-\frac{1}{4}\{\eta_1 - 2i\alpha_2\}^2\right] \exp\left[-\frac{1}{4}\{\eta_2 + 2i\alpha_1\}^2\right], \quad (3.54)$$

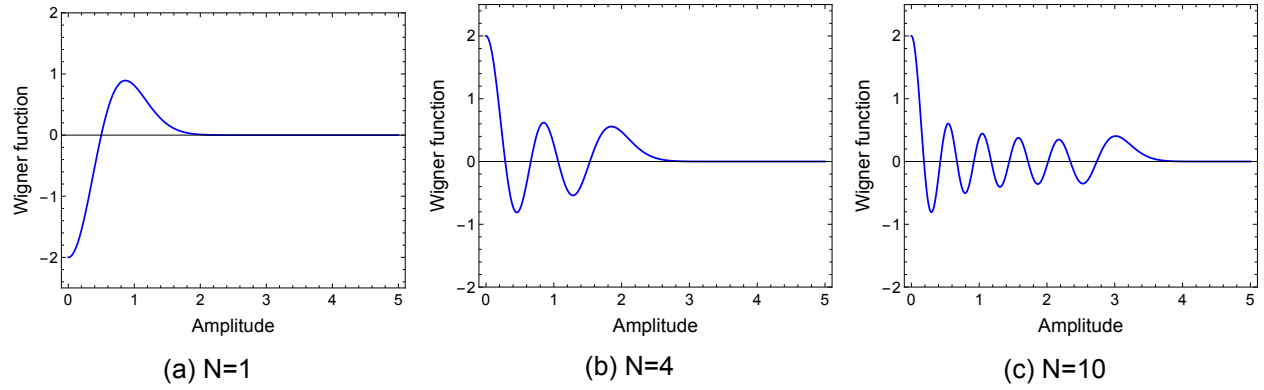


Figure 3.2: Wigner functions of the Fock states at (a)  $N = 1$ , (b)  $N = 4$ , and (c)  $N = 10$ , respectively. The horizontal axis represents the radial direction of the phase space denoted by  $|\alpha|$ .

in which we have used  $\eta_1 = \text{Re}[\eta]$ ,  $\eta_2 = \text{Im}[\eta]$ ,  $\alpha_1 = \text{Re}[\alpha]$ , and  $\alpha_2 = \text{Im}[\alpha]$ . Introducing new variables of integration as

$$z_1 = \frac{\eta_1}{2} - i\alpha_2, \quad z_2 = \frac{\eta_2}{2} + i\alpha_1, \quad (3.55)$$

and noticing the fact that the integration of  $z_1$  ( $z_2$ ) over  $[-\infty - i\alpha_2, \infty - i\alpha_2]$  ( $[-\infty + i\alpha_1, \infty + i\alpha_1]$ ) is equal to the integration at the real axis over  $[-\infty, \infty]$ , we can evaluate the integral as

$$\begin{aligned} W_N(\alpha, \alpha^*) &= \frac{2}{\pi N!} e^{-2|\alpha|^2} \int d^2\tilde{\eta} (2\alpha^* - \tilde{\eta}^*)^N (2\alpha + \tilde{\eta})^N e^{-|\tilde{\eta}|^2}, \\ &= \frac{2}{\pi N!} e^{-2|\alpha|^2} \sum_{n=0}^N \sum_{m=0}^N \int d^2\tilde{\eta} \frac{N!(2\alpha^*)^{N-n}}{(N-n)!n!} \frac{N!(2\alpha)^{N-m}}{(N-m)!m!} (-\tilde{\eta}^*)^n (\tilde{\eta})^m e^{-|\tilde{\eta}|^2} \\ &= \frac{2}{\pi} e^{-2|\alpha|^2} \sum_{n=0}^N \frac{N!(-1)^n}{(N-n)!^2 n!^2} (4|\alpha|^2)^{N-n} \int d^2\tilde{\eta} |\tilde{\eta}|^{2n} e^{-|\tilde{\eta}|^2} \\ &= 2e^{-2|\alpha|^2} (-1)^N L_N(4|\alpha|^2), \end{aligned} \quad (3.56)$$

where

$$L_N(x) = \sum_{r=0}^N (-1)^r \frac{N!}{(N-r)!(r!)^2} x^r \quad (3.57)$$

is the  $N$ -th order Laguerre polynomial. Due to the property of the Laguerre polynomial, the Wigner function of the Fock state is not positive at  $N > 0$ . At  $N = 0$ , the function is positive because it corresponds to the vacuum state. In Fig. 3.2, we present  $W_N(\alpha, \alpha^*)$  at different  $N$ .

### 3.3 Quantum dynamics in the coherent-state phase space

In this section, we formulate dynamics of the Bose fields using the phase-space representation. When the system is isolated from external environments, the dynamics of the system can be governed by the von-Neumann equation

$$i\hbar \frac{\partial}{\partial t} \hat{\rho}(t) = [\hat{H}, \hat{\rho}(t)], \quad (3.58)$$

where  $\hat{H} = \hat{H}^\dagger$  denotes the Hamiltonian and the density operator  $\hat{\rho}(t)$  describes the quantum state of the system at time  $t$ . For pure states, the von-Neumann equation can reduce to the Schrödinger equation, which describes the time evolution of the wave function  $|\psi(t)\rangle$ :

$$i\hbar \frac{\partial}{\partial t} |\psi(t)\rangle = \hat{H} |\psi(t)\rangle. \quad (3.59)$$

The density operator or wave function is assumed to be normalized at  $t = 0$  with a condition  $\text{Tr}[\hat{\rho}(0)] = 1$  or  $\langle \psi(0) | \psi(0) \rangle = 1$ . Since the time evolution described by Eqs. (3.58) or (3.59) is unitary, the normalization condition is preserved in time:  $\text{Tr}[\hat{\rho}(t)] = 1$  or  $\langle \psi(t) | \psi(t) \rangle = 1$  ( $t > 0$ ).

The density operator is able to provide the expectation value of an arbitrary observable  $\hat{\Omega}(\hat{a}, \hat{a}^\dagger)$  at time  $t$ , i.e.,

$$\langle \hat{\Omega}(t) \rangle = \text{Tr}[\hat{\rho}(t) \hat{\Omega}]. \quad (3.60)$$

Using the general relation (3.40), we can translate Eq. (3.60) into a phase-space averaged form weighted with the time-dependent Wigner function  $W(\vec{\alpha}, \vec{\alpha}^*, t) = [\hat{\rho}(t)]_W(\vec{\alpha}, \vec{\alpha}^*)$ :

$$\langle \hat{\Omega}(t) \rangle = \int d\vec{\alpha} d\vec{\alpha}^* \Omega_W(\vec{\alpha}, \vec{\alpha}^*) W(\vec{\alpha}, \vec{\alpha}^*, t). \quad (3.61)$$

In this representation, the dynamics of the system is entirely represented though the time evolution of the classical distribution function on the phase space. Since the condition  $\text{Tr}[\hat{\rho}(0)] = 1$ , the Wigner function at  $t = 0$  is normalized as follows:

$$\int d\vec{\alpha} d\vec{\alpha}^* W(\vec{\alpha}, \vec{\alpha}^*, 0) = 1. \quad (3.62)$$

In addition, the unitarity of the time-evolution equation (3.58) preserves this normalization in time.

The Wigner function evolves in time according to an equation derived from the von-Neumann equation (3.58). Performing the Wigner transform of both sides of Eq. (3.58) and utilizing the Moyal bracket (3.29), we find that the time evolution of the Wigner function is generated by

$$\begin{aligned} i\hbar \frac{\partial W}{\partial t} &= \{H_W, W\}_{\text{M.B.}} \\ &= 2H_W \sinh \left[ \frac{1}{2} \Lambda_c \right] W, \end{aligned} \quad (3.63)$$

where  $H_W = (\hat{H})_W$  is the Weyl symbol of the Hamiltonian. This is a linear equation with respect to  $W$ , and involves complicated differentials of the phase-space variables. If we can solve this equation and obtain an exact Wigner function at each moment, the full quantum dynamics and correct average  $\langle \hat{\Omega}(t) \rangle$  of the system are completely described.

### 3.3.1 Truncated-Wigner approximation

The full information of the quantum dynamics is encoded in the Wigner function  $W(\vec{\alpha}, \vec{\alpha}^*, t)$ , which is obtained as a solution of Eq. (3.63). Nevertheless, solving the time-evolution equation (3.63) and determining  $W(\vec{\alpha}, \vec{\alpha}^*, t)$  with no approximation is generally hard even for small systems with a few degrees of freedom.

When the system is near a semiclassical limit, it is possible to diminish the difficulty associated with determining the time evolution by using a semiclassical expansion. To illustrate our idea, let us formally expand the righthand side of Eq. (3.63) in the symplectic operator  $\Lambda_c$ :

$$i\hbar \frac{\partial W}{\partial t} = H_W \Lambda_c W + \frac{1}{3!2^2} H_W \Lambda_c^3 W + \frac{1}{5!2^4} H_W \Lambda_c^5 W + \dots \quad (3.64)$$

If we truncate higher-order terms of order  $O(\Lambda_c^3)$  from the expansion series, then the time evolution of the Wigner function is effectively generated by the classical Liouville equation

$$i\hbar \frac{\partial W}{\partial t} \approx \{H_W, W\}_{\text{P.B.}} \quad (3.65)$$

Within Eq. (3.65), the Wigner function is conserved along characteristic trajectories, which are solutions of the classical Gross–Pitaevskii equation:

$$i\hbar \frac{\partial \alpha_{\text{cl},j}}{\partial t} = \frac{\partial H_W}{\partial \alpha_{\text{cl},j}^*}, \quad i\hbar \frac{\partial \alpha_{\text{cl},j}^*}{\partial t} = -\frac{\partial H_W}{\partial \alpha_{\text{cl},j}}. \quad (3.66)$$

In classical statistical mechanics, this property is known as the Liouville theorem [123]. Using this theorem, we find that the quantum average  $\langle \hat{\Omega}(t) \rangle$  reduces to a semiclassical form

$$\langle \hat{\Omega}(t) \rangle \approx \int d\vec{\alpha}_0 d\vec{\alpha}_0^* W_0(\vec{\alpha}_0, \vec{\alpha}_0^*) \Omega_W[\vec{\alpha}_{\text{cl}}(\vec{\alpha}_0, \vec{\alpha}_0^*, t), \vec{\alpha}_{\text{cl}}^*(\vec{\alpha}_0, \vec{\alpha}_0^*, t)], \quad (3.67)$$

which is constructed from two ingredients: the classical Gross–Pitaevskii trajectory  $\vec{\alpha}_{\text{cl}}(\vec{\alpha}_0, \vec{\alpha}_0^*, t)$  starting from a point  $\vec{\alpha}_0$  and the Wigner function  $W_0(\vec{\alpha}_0, \vec{\alpha}_0^*) = [\hat{\rho}(0)]_W(\vec{\alpha}_0, \vec{\alpha}_0^*)$  for the initial density operator. Usually, obtaining these is much simpler than directly solving Eq. (3.63). This approximation is called the TWA [48, 49].

Equation (3.67) states that the initial classical field  $\vec{\alpha}_0$  distributes over the phase space according to the Wigner function of the initial quantum state. Within the TWA, the initial conditions of

the classical dynamics fluctuate around a mean configuration, whereas the time evolution itself is entirely deterministic. This *randomness* of the initial configurations describes a leading-order correction to the mean-field solution of dynamics due to quantum fluctuations [49, 51, 129]. Indeed, the mean-field result can be obtained if we formally neglect the width of the Wigner function. Then, the classical field evolves from a fixed configuration  $\alpha_{\text{cl},j}(t = 0) = \langle \hat{a}_j \rangle$ . In Fig. 3.3, we show the difference between the MFA and TWA schematically. It should be emphasized that since the Wigner function is not positive definite, it is not always correct to interpret each trajectory as a randomized sample from a well-defined probability distribution (see also Ref. [49]). Nevertheless, such a rough picture is often useful, and effectively valid for some cases where we are able to find an appropriate Gaussian distribution to approximate the exact Wigner function within the same accuracy of the TWA (for details of the Gaussian approximation, see Chap. 5).

We note that the classical field scales with a square root of the mode occupancy  $n_{\text{ocp}}$ , so that the expansion in  $\Lambda_c$  is characterized by the inverse of  $n_{\text{ocp}}$ . For the Bose–Hubbard model,  $n_{\text{ocp}}$  is equal to the filling factor per site. It is known that the TWA is asymptotically exact at short times, in fact, the valid timescale of the semiclassical approximation becomes longer for larger  $n_{\text{ocp}}$  (see also Ref. [49]). Moreover, if the system is linear or non-interacting, the semiclassical approximation then becomes exact because the higher-order terms exactly vanish. Usually, the TWA offers a good approach for systems where fluctuations are small or the Hamiltonian has a weak non-linearity. Indeed, a small non-linearity seems to produce a small error of the truncation as seen in Eq. (3.64).

### 3.3.2 Semiclassical approximation in phase-space path integrals

The method of characteristic based on the semiclassical expansion is not the unique way to derive the TWA. The semiclassical approximation can also be obtained from a similar approximation of a phase-space path-integral representation of the quantum expectation values [151]. For simplicity, we restrict ourselves to the single-mode case in what follows.

Our starting point is a Heisenberg operator with the unitary time-evolution operator  $\hat{\mathcal{U}}(t, t_0)$ :

$$\hat{\Omega}_{t_0}(t) = \hat{\mathcal{U}}^\dagger(t, t_0) \hat{\Omega}(t) \hat{\mathcal{U}}(t, t_0), \quad (3.68)$$

where the foot index indicates the time at which  $\hat{\Omega}_{t_0}(t)$  coincides with the Schrödinger representation  $\hat{\Omega}(t)$ . In addition, we take into account the explicit dependence of the Schrödinger representation on time. Using the Heisenberg representation, the quantum expectation value of  $\hat{\rho}(t)$  reads

$$\langle \hat{\Omega}(t) \rangle = \text{Tr} \left[ \hat{\rho}(t_0) \hat{\Omega}_{t_0}(t) \right]. \quad (3.69)$$

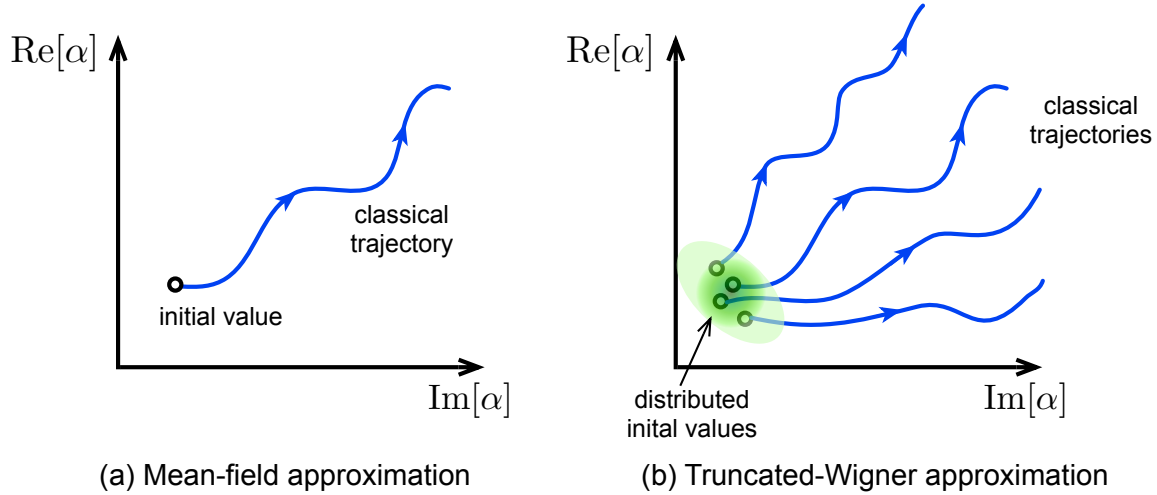


Figure 3.3: Schematic picture of the (a) MFA and (b) TWA. The vertical and horizontal axes indicate the phase-space variable  $\alpha$ . Each line represents the solution of the Gross–Pitaevskii equation.

The next step is to transform this into a phase-space representation. Using Eq. (3.40), it reads

$$\langle \hat{\Omega}(t) \rangle = \int \frac{d^2\alpha_0}{\pi} W(\alpha_0, t_0) [\hat{\Omega}_{t_0}(t)]_W(\alpha_0), \quad (3.70)$$

where  $W(t_0) = [\hat{\rho}(t_0)]_W$ . It can be proved that the time-dependent Weyl symbol  $[\hat{\Omega}_{t_0}(t)]_W(\alpha_0)$  is linearly related with the one at time  $t_0$ :

$$[\hat{\Omega}_{t_0}(t)]_W(\alpha_0) = \int \frac{d^2\alpha}{\pi} \Omega_W(\alpha, t) U_W(\alpha, t; \alpha_0, t_0), \quad (3.71)$$

where  $U_W(\alpha, t; \alpha_0, t_0)$  is given by

$$U_W(\alpha, t; \alpha_0, t_0) = \int \frac{d^2\beta d^2\beta_0}{\pi^2} e^{-\alpha\beta^* + \alpha^*\beta} e^{-\alpha_0\beta_0^* + \alpha_0^*\beta_0} \text{Tr}[\hat{D}^\dagger(\beta) \hat{U}(t, t_0) \hat{D}^\dagger(\beta_0) \hat{U}^\dagger(t, t_0)]. \quad (3.72)$$

Thus, the expectation value is expressed as

$$\langle \hat{\Omega}_{t_0}(t) \rangle = \int \frac{d^2\alpha d^2\alpha_0}{\pi^2} \Omega_W(\alpha, t) U_W(\alpha, t; \alpha_0, t_0) W(\alpha_0, t_0). \quad (3.73)$$

The two point function  $U_W(\alpha, t; \alpha_0, t_0)$  can be regarded as a propagator connecting the initial and end points of the time evolution in the phase space.

Let us explain the important properties of the phase-space propagator  $U_W(\alpha, t; \alpha_0, t_0)$ . Due to the property of the unitary operator, a relation

$$\hat{U}(t, t_1) \hat{U}(t_1, t_0) = \hat{U}(t, t_0). \quad (3.74)$$

holds for  $t_0 \leq t_1 \leq t$ . Inserting this relation into each interval of the unitary operators again, we obtain an iterative relation:

$$\hat{\mathcal{U}}(t, t_N)\hat{\mathcal{U}}(t_N, t_{N-1}) \cdots \hat{\mathcal{U}}(t_2, t_1)\hat{\mathcal{U}}(t_1, t_0) = \hat{\mathcal{U}}(t, t_0), \quad (3.75)$$

for  $t_0 \leq t_1 \leq t_2 \leq \cdots \leq t_{N-1} \leq t_N \leq t$ . There are similar relations in the phase-space propagator. In fact, from direct calculations, we can prove that

$$U_W(\alpha, t; \alpha_0, t_0) = \int \frac{d^2\alpha_1}{\pi} U_W(\alpha, t; \alpha_1, t_1) U_W(\alpha_1, t_1; \alpha_0, t_0) \quad (3.76)$$

for  $t_0 \leq t_1 \leq t$ . Using this relation iteratively, we find that

$$U_W(\alpha, t; \alpha_0, t_0) = \int \prod_{n=1}^N \frac{d^2\alpha_n}{\pi} U_W(\alpha, t; \alpha_N, t_N) U_W(\alpha_N, t_N; \alpha_{N-1}, t_{N-1}) \cdots \\ \times U_W(\alpha_2, t_2; \alpha_1, t_1) U_W(\alpha_1, t_1; \alpha_0, t_0). \quad (3.77)$$

Thus, if the number of steps  $N$  is so large that the time interval is infinitesimal, Eq. (3.73) can be rewritten into a phase-space path-integral form. Notice that the boundary of the path integral is now not fixed by specific phase-space points. In particular, the initial point is weighted with the initial Wigner function  $W(\alpha_0, t_0)$ .

Let us determine the phase-space propagator for the infinitesimal interval. For the purpose, we use the fact that a similar relation to Eq. (3.71) is also true for the Wigner function:

$$W(\alpha, t) = \int \frac{d^2\alpha_0}{\pi} U_W(\alpha, t; \alpha_0, t_0) W(\alpha_0, t_0). \quad (3.78)$$

For a small interval  $\Delta t$ , the Wigner function propagates with satisfying

$$W(\alpha, t + \Delta t) = \int \frac{d^2\alpha_0}{\pi} U_W(\alpha, t + \Delta t; \alpha_0, t) W(\alpha_0, t). \quad (3.79)$$

To obtain the interval propagator  $U_W(\alpha, t + \Delta t; \alpha_0, t)$ , we consider the von-Neumann equation for the interval time step:

$$\hat{\rho}(t + \Delta t) = \hat{\rho}(t) + \frac{\Delta t}{i\hbar} [\hat{H}\hat{\rho}(t) - \hat{\rho}(t)\hat{H}]. \quad (3.80)$$

Using the Moyal product, we obtain from Eq. (3.80) that

$$W(\alpha, t + \Delta t) = W(\alpha, t) + \int \frac{d^2\alpha_0}{\pi} \frac{d^2\sigma}{\pi} e^{\sigma^*(\alpha - \alpha_0) - \sigma(\alpha^* - \alpha_0^*)} \\ \times \left\{ 1 - \frac{\Delta t}{i\hbar} \sum_{n=0}^{\infty} \frac{1}{2^{2n}} \sum_{s_1, s_2=0}^{s_1+s_2=2n+1} \frac{H_W^{(s_1, s_2)}(\alpha_0)}{s_1! s_2!} (\sigma)^{s_1} (\sigma^*)^{s_2} \right\} W(\alpha_0, t), \quad (3.81)$$

where  $H_W^{(s_1, s_2)}(\alpha)$  implies

$$H_W^{(s_1, s_2)}(\alpha) = \frac{\partial^{s_1+s_2} H_W(\alpha)}{\partial \alpha^{s_1} \partial (\alpha^*)^{s_2}}. \quad (3.82)$$

Comparing Eqs. (3.79) and (3.81), it is found that

$$U_W(\alpha, t + \Delta t; \alpha_0, t) = \int \frac{d^2 \sigma}{\pi} e^{\sigma^*(\alpha - \alpha_0) - \sigma(\alpha^* - \alpha_0^*)} \times \left\{ 1 - \frac{\Delta t}{i\hbar} \sum_{n=0}^{\infty} \frac{1}{2^{2n}} \sum_{s_1, s_2=0}^{s_1+s_2=2n+1} \frac{H_W^{(s_1, s_2)}(\alpha_0)}{s_1! s_2!} (\sigma)^{s_1} (\sigma^*)^{s_2} \right\}. \quad (3.83)$$

Notice that  $\alpha$  and  $\alpha_0$  correspond to the mean-field degrees of freedom, whereas  $\sigma$  describes the quantum fluctuations.

Equation (3.83) has no approximation and actually involves the full information of the exact quantum dynamics. If we neglect higher-order terms with respect to the quantum fluctuations, we can obtain again the TWA. Up to the leading order of the  $\sigma$ -field, the infinitesimal propagator becomes a delta function:

$$\begin{aligned} U_W(\alpha, t + \Delta t; \alpha_0, t) &\approx \int \frac{d^2 \sigma}{\pi} e^{\sigma^*(\alpha - \alpha_0) - \sigma(\alpha^* - \alpha_0^*)} \left\{ 1 - \frac{\Delta t}{i\hbar} \frac{\partial H_W}{\partial \alpha_0^*} \sigma^* - \frac{\Delta t}{i\hbar} \frac{\partial H_W}{\partial \alpha_0} \sigma \right\} \\ &\approx \int \frac{d^2 \sigma}{\pi} \exp \left[ \sigma^* \left( \alpha - \alpha_0 - \frac{\Delta t}{i\hbar} \frac{\partial H_W}{\partial \alpha_0^*} \right) - \sigma \left( \alpha^* - \alpha_0^* + \frac{\Delta t}{i\hbar} \frac{\partial H_W}{\partial \alpha_0} \right) \right] \\ &= \pi \delta \left( \alpha - \alpha_0 - \frac{\Delta t}{i\hbar} \frac{\partial H_W}{\partial \alpha_0^*} \right) \delta \left( \alpha^* - \alpha_0^* + \frac{\Delta t}{i\hbar} \frac{\partial H_W}{\partial \alpha_0} \right). \end{aligned} \quad (3.84)$$

Using this result, we finally obtain the TWA formula ( $\Delta t \rightarrow 0$ ):

$$\begin{aligned} \langle \hat{\Omega}_{t_0}(t) \rangle &\approx \int \frac{d^2 \alpha d^2 \alpha_0}{\pi^2} \prod_{n=1}^N \frac{d^2 \alpha_n}{\pi} \Omega_W(\alpha, t) \prod_{m=1}^{N+1} \pi \delta^{(2)} \left( \alpha_m - \alpha_{m-1} - \frac{\Delta t}{i\hbar} \frac{\partial H_W}{\partial \alpha_{m-1}^*} \right) W(\alpha_0, t_0) \\ &= \int d\alpha_0 d\alpha_0^* \Omega_W[\alpha_{cl}(\alpha_0, t)] W(\alpha_0, t_0) \end{aligned} \quad (3.85)$$

where  $\alpha_{N+1} = \alpha$  and  $\alpha_{cl}(\alpha_0, t)$  is the solution of the single-mode Gross–Pitaevskii equation starting from  $\alpha = \alpha_0$  at time  $t_0$ .

Within the leading order, the time evolution is entirely deterministic and described within the classical Gross–Pitaevskii equation. Then, the quantum fluctuation effects are encoded only in the Wigner function at time  $t_0$ . It is worth noting that the higher-order corrections of the fluctuations give rise to infinitesimal jumps of each classical trajectory and lead to perturbative modifications of the TWA expectation value, which can be regarded as non-linear responses to the jumps [49, 129]. However, we do not take into account these higher-order contributions in this thesis.

# Chapter 4

## Response of the Higgs mode in a three dimensional optical lattice

In this Chapter, we investigate responses of the Higgs mode in strongly-correlated Bose gases in a three-dimensional (3D) optical lattice. Our final goal of this chapter is to examine the detectability of the long-lived Higgs modes in real experiments of ultracold gases. In Sec. 4.1, we discuss time-dependent external perturbations to excite the Higgs mode in the optical lattice and formulate the resulting response functions within the linear-response theory. In Sec. 4.2, we generalize the discussion presented in Chap. 2 for the high-filling limit into low-filling cases, and derive interaction vertices between the Higgs and Nambu–Goldstone (NG) modes by evaluating higher-order contributions of the Holstein–Primakoff (HP) expansion. In Sec. 4.3, we compute the response functions using a finite-temperature Green’s function technique based on the Feynman’s diagrammatic perturbation theory. In Sec. 4.4, we numerically evaluate the perturbative formulae and show that the response functions exhibit characteristic signals associated with the Higgs mode. In addition, we deal with a harmonic trap effect on the response function within a local density approximation and discuss the detectability in typical experiments. In Sec. 4.5, we conclude and summarize this chapter. Throughout this chapter, we set  $\hbar = k_B = 1$  and omit the *hat* symbols from operators.

### 4.1 Time-dependent external perturbations and linear responses

The basic idea for exciting the Higgs mode is to modulate the condensate density  $|\Psi|^2$  with a small amplitude of vibration [95]. For the Bose–Hubbard model, this can be performed by modulating a dimensionless ratio  $J/U$ , which determines the order-parameter amplitude of a ground state. A typical method utilized in experiments to modulate it is the optical-lattice amplitude modulation technique [16, 19], which leads to a modulation of the hopping strength  $J$  (its detailed discussions

can be found in some literatures [44, 95, 152]). The experiment of Ref. [19] has achieved periodic modulations of the lattice depth with a sufficiently small vibrational amplitude (3 % of the initial depth) to the extent that the resulting response is in a linear response region.

### 4.1.1 Modulations of the kinetic energy

The response to the  $J$  modulation can be formulated by the linear response theory as follows: Let us assume that the system is in the thermal equilibrium state with the inverse temperature  $\beta = T^{-1}$  at  $t \rightarrow -\infty$ . When we add a small and periodic modulation to the hopping strength  $J$  slowly such that  $J \rightarrow [1 + \Delta_J(t)]J$  where  $\Delta_J(t) = \delta_J \cos(\omega t)$  and  $\delta_J$  is sufficiently small, then the Hamiltonian describing the weak perturbation reads

$$\mathcal{H}_{\text{BH}} \rightarrow \mathcal{H}_{\text{BH}} + \Delta_J(t)K,$$

where  $K \equiv -J \sum_{\langle ij \rangle} a_i^\dagger a_j$  is the kinematic energy. The second term on the righthand side denotes the weak perturbation term. The instantaneous change of the total energy to the small and periodic modulations is proportional to the instantaneous quantum mechanical average of the kinetic energy [95, 152]. Therefore, the response of the system to the modulations is characterized only by the response of the kinetic energy and described by the  $K$ -to- $K$  response function [43, 44]

$$D_{KK}^{\text{R}}(t - t') = -i\Theta(t - t') \langle [K(t), K(t')] \rangle_{\text{eq}}, \quad (4.1)$$

where  $\Theta(t)$  is the step function, which outputs 1 for  $t > 0$  and 0 for  $t < 0$ . Here,  $K(t) = e^{i\mathcal{H}_{\text{BH}}t} K e^{-i\mathcal{H}_{\text{BH}}t}$ . The bracket  $\langle \dots \rangle_{\text{eq}}$  means the normalized ensemble average of the thermal equilibrium state at  $t \rightarrow -\infty$ :  $\langle \dots \rangle_{\text{eq}} \equiv \text{Tr}(e^{-\beta\mathcal{H}_{\text{BH}}} \dots) / \text{Tr} e^{-\beta\mathcal{H}_{\text{BH}}}$ . The imaginary part of the dynamical susceptibility

$$\chi_{KK}(\omega) = \int_{-\infty}^{\infty} D_{KK}^{\text{R}}(t) e^{i\omega t} dt, \quad (4.2)$$

is the spectral function  $S_{KK}(\omega) = -\text{Im}[\chi_{KK}(\omega)]$ , which is proportional to the external energy absorbed by the system for a finite-time period of the modulation [19, 95]. The response function or its susceptibility characterizes the resonance of the Higgs mode in experimental systems [19, 43]. The Max-Planck experiment [19] has obtained  $S_{KK}(\omega)$  at low frequencies by measuring the temperature increase of the system after the lattice-amplitude modulation with a fixed modulation time.

### 4.1.2 Modulations of the onsite-interaction energy

In Sec. 4.1.1, we briefly reviewed the conventional  $J$  modulations and consequent response. On the other hand, one can also modulate the onsite interaction  $U$  to oscillate  $J/U$ . To our knowledge,

this kind of modulation has not been discussed thus far as a probe of the Higgs mode. In this section we explain what types of response function characterize the response to the  $U$  modulations and how one can realize that modulation in experiments with high controllability. Moreover, we will show in detail the relation between the response function and energy absorbed by the system for a period of the  $U$  modulation in Appendix A.

Let us consider a linear response problem to the  $U$  modulation in a similar way to the  $J$  modulation. When we turn on a small and periodic modulation  $U \rightarrow [1 + \Delta_U(t)]U$  where  $\Delta_U(t) = \delta_U \cos(\omega t)$  and  $\delta_U$  is sufficiently small, then the Hamiltonian becomes

$$\mathcal{H}_{\text{BH}} \rightarrow \mathcal{H}_{\text{BH}} + \Delta_U(t)O,$$

where  $O \equiv \frac{U}{2} \sum_i (n_i - n_0)^2$  is the onsite-interaction energy. In a similar manner to the  $J$  modulations, the instantaneous change rate of the total energy is proportional to the quantum mechanical average of the onsite energy (for details, see Appendix A). Thus, within the linear response theory, the consequent response can be described by the  $O$ -to- $O$  response function

$$D_{OO}^{\text{R}}(t - t') = -i\Theta(t - t') \langle [O(t), O(t')] \rangle_{\text{eq}}, \quad (4.3)$$

where  $O(t) = e^{i\mathcal{H}_{\text{BH}}t} O e^{-i\mathcal{H}_{\text{BH}}t}$ . The imaginary part of the dynamical susceptibility

$$\chi_{OO}(\omega) = \int_{-\infty}^{\infty} D_{OO}^{\text{R}}(t) e^{i\omega t} dt, \quad (4.4)$$

is the spectral function  $S_{OO}(\omega) = -\text{Im}[\chi_{OO}(\omega)]$ , which is proportional to the external energy absorbed by the system for a finite-time period of the modulation (see Appendix A). We expect that this response function or its susceptibility also characterizes the resonance of the Higgs mode.

Recent experimental developments in the fields of ultracold gases enable one to control the onsite interaction by using highly controlled optical techniques, such as *the optical Feshbach resonance* [153–155] and *the optically induced Feshbach resonance* [156, 157]. In contrast to the conventional magnetic Feshbach resonance, these techniques allow for fast temporal modulation of  $U$  with a frequency on the order of 1 to 10 kHz, which is supposed to be comparable to a typical resonance frequency of the Higgs mode.

## 4.2 Interactions between collective modes

The main purpose of this chapter is to analyze the dynamical susceptibilities (4.2) and (4.4), respectively for the (grand-canonical) 3D Bose–Hubbard model (2.20) in the strongly-interacting regime in which the Higgs and NG modes can appear as dominant low-energy excitations. To

do that, we utilize the effective pseudospin-1 mapping explained in Chap. 2 for simplifying the original Bose–Hubbard model. Especially, in order to deal with an experimental situation where the atomic occupation is tuned to unity, the modified effective model (2.45) is mainly used. An entirely similar analysis based on the high-filling effective model is also performed to compare two results at different fillings (see Sec. 4.4.1).

In this section, before going to our main analysis of the susceptibilities, we derive an approximate *spin-wave* Hamiltonian, which describes the mean-field dispersion relations of the Higgs and NG modes and interactions among them. To perform that, we apply the HP expansion to the effective pseudospin-1 model at low fillings (2.45). Although a similar expansion up to the quadratic order (no interaction) was discussed by Huber et al. in Ref. [92], we present its derivation in details because our analysis successfully gives higher-order corrections beyond their result, i.e. transition or interaction effects among different eigenfunctions obtained within the quadratic order. The subsequent corrections give rise to a finite lifetime of the collective modes. This is nothing but our main focus of this study.

### 4.2.1 Fluctuations from the mean-field ground state

Let us start again from considering the fluctuations around the mean-field superfluid state derived from the Gutzwiller’s ansatz in Chap. 2. Substituting the canonical transformation (2.55) into the low-filling effective model (2.45), we obtain the Hamiltonian describing the collective fluctuations around the mean field. The resulting Hamiltonian consists of five parts:

$$\mathcal{H}_{\text{eff}} = \mathcal{H}_{\text{eff}}^{(0)} + \mathcal{H}_{\text{eff}}^{(1)} + \mathcal{H}_{\text{eff}}^{(2)} + \mathcal{H}_{\text{eff}}^{(3)} + \mathcal{H}_{\text{eff}}^{(4)}, \quad (4.5)$$

where each term contained in  $\mathcal{H}_{\text{eff}}^{(l)}$  ( $l = 0, 1, 2, 3, 4$ ) has  $l$  numbers of the fluctuation operator  $b_{m,i}^\dagger, b_{m,i}$  ( $m = 1, 2$ ). The explicit forms of  $\mathcal{H}_{\text{eff}}^{(0)}$  and  $\mathcal{H}_{\text{eff}}^{(1)}$  are given by

$$\begin{aligned} \mathcal{H}_{\text{eff}}^{(0)} &= \sum_{\langle ij \rangle} \frac{1}{z} A_0 b_{0,i}^\dagger b_{0,i} b_{0,j}^\dagger b_{0,j} + \sum_i \tilde{A}_0 b_{0,i}^\dagger b_{0,i}, \\ \mathcal{H}_{\text{eff}}^{(1)} &= \sum_{\langle ij \rangle} \frac{1}{z} A_1 b_{0,i}^\dagger b_{0,i} b_{1,j}^\dagger b_{0,j} + \sum_{\langle ij \rangle} \frac{1}{z} B_1 b_{0,i}^\dagger b_{0,i} b_{2,j}^\dagger b_{0,j} + \sum_i \tilde{A}_1 b_{1,i}^\dagger b_{0,i} + \sum_i \tilde{B}_1 b_{2,i}^\dagger b_{0,i} + \text{H.c.} \end{aligned}$$

The quadratic term  $\mathcal{H}_{\text{eff}}^{(2)}$  is presented by

$$\begin{aligned} \mathcal{H}_{\text{eff}}^{(2)} &= \sum_{\langle ij \rangle} \frac{1}{2z} A_2 b_{0,i}^\dagger b_{0,i} b_{1,j}^\dagger b_{1,j} + \sum_{\langle ij \rangle} \frac{1}{z} B_2 b_{0,i}^\dagger b_{0,i} b_{1,j}^\dagger b_{2,j} + \sum_{\langle ij \rangle} \frac{1}{z} D_2 b_{1,i}^\dagger b_{0,i} b_{1,j}^\dagger b_{0,j} + \sum_{\langle ij \rangle} \frac{1}{2z} E_2 b_{1,i}^\dagger b_{0,i} b_{0,j}^\dagger b_{1,j} \\ &+ \sum_{\langle ij \rangle} \frac{1}{z} F_2 b_{1,i}^\dagger b_{0,i} b_{0,j}^\dagger b_{2,j} + \sum_{\langle ij \rangle} \frac{1}{z} G_2 b_{1,i}^\dagger b_{0,i} b_{2,j}^\dagger b_{0,j} + \sum_{\langle ij \rangle} \frac{1}{z} H_2 b_{0,i}^\dagger b_{2,i} b_{0,j}^\dagger b_{2,j} + \sum_{\langle ij \rangle} \frac{1}{2z} I_2 b_{0,i}^\dagger b_{2,i} b_{2,j}^\dagger b_{0,j} \\ &+ \sum_i \frac{1}{2} \tilde{A}_2 b_{1,i}^\dagger b_{1,i} + \sum_i \tilde{B}_2 b_{1,i}^\dagger b_{2,i} + \sum_i \frac{1}{2} \tilde{C}_2 b_{2,i}^\dagger b_{2,i} + \text{H.c.} \end{aligned}$$

Moreover, the remaining terms  $\mathcal{H}_{\text{eff}}^{(3)}$  and  $\mathcal{H}_{\text{eff}}^{(4)}$  are given by

$$\begin{aligned}\mathcal{H}_{\text{eff}}^{(3)} &= \sum_{\langle ij \rangle} \frac{1}{z} A_3 b_{1,i}^\dagger b_{1,i} b_{1,j}^\dagger b_{0,j} + \sum_{\langle ij \rangle} \frac{1}{z} B_3 b_{1,i}^\dagger b_{1,i} b_{2,j}^\dagger b_{0,j} + \sum_{\langle ij \rangle} \frac{1}{z} C_3 b_{1,i}^\dagger b_{0,i} b_{2,j}^\dagger b_{1,j} + \sum_{\langle ij \rangle} \frac{1}{z} D_3 b_{1,i}^\dagger b_{0,i} b_{1,j}^\dagger b_{2,j} \\ &+ \sum_{\langle ij \rangle} \frac{1}{z} E_3 b_{0,i}^\dagger b_{2,i} b_{2,j}^\dagger b_{1,j} + \sum_{\langle ij \rangle} \frac{1}{z} F_3 b_{0,i}^\dagger b_{2,i} b_{1,j}^\dagger b_{2,j} + \text{H.c.}, \\ \mathcal{H}_{\text{eff}}^{(4)} &= \sum_{\langle ij \rangle} \frac{1}{2z} A_4 b_{1,i}^\dagger b_{1,i} b_{1,j}^\dagger b_{1,j} + \sum_{\langle ij \rangle} \frac{1}{z} B_4 b_{1,i}^\dagger b_{2,i} b_{1,j}^\dagger b_{2,j} \\ &+ \sum_{\langle ij \rangle} \frac{1}{z} C_4 b_{1,i}^\dagger b_{2,i} b_{1,j}^\dagger b_{1,j} + \sum_{\langle ij \rangle} \frac{1}{2z} D_4 b_{1,i}^\dagger b_{2,i} b_{2,j}^\dagger b_{1,j} + \text{H.c.}\end{aligned}$$

In the above representations, the coefficients such as  $A_0, \tilde{A}_0, A_1, B_1, \dots$  depend on  $J$  and  $\mu$  via the variational parameter  $\theta_{\text{mf}}$ . The explicit forms are summarized in Appendix B. Notice again that  $z = 2d = 6$  is the coordination number at three dimensions.

### 4.2.2 Holstein–Primakoff expansion

As a next step, we expand  $\mathcal{H}_{\text{eff}}^{(l)}$  with respect to the fluctuations using the Holstein–Primakoff (HP) expansion (2.57):

$$b_{m,i}^\dagger b_{0,j} \approx b_{m,i}^\dagger - \frac{1}{2} b_{m,i}^\dagger b_{1,j}^\dagger b_{1,j} - \frac{1}{2} b_{m,i}^\dagger b_{2,j}^\dagger b_{2,j} + \dots$$

Eliminating  $b_{0,i}^\dagger b_{0,i}$  in the Hamiltonian (4.5) by using the constraint  $\sum_n b_n^\dagger b_n = 1$ , and substituting the HP expansion (2.57) into the Hamiltonian (4.5), we obtain the following series

$$\mathcal{H}_{\text{eff}} \approx \mathcal{H}_{\text{SW}}^{(0)} + \mathcal{H}_{\text{SW}}^{(1)} + \mathcal{H}_{\text{SW}}^{(2)} + \mathcal{H}_{\text{SW}}^{(3)} + \mathcal{H}_{\text{SW}}^{(4)} \dots, \quad (4.6)$$

where each term  $\mathcal{H}_{\text{SW}}^{(l)}$  (for  $l = 0, 1, 2, 3, 4, \dots$ ) describes processes involving  $l$  collective-mode operators. The control parameter of the HP expansion is characterized by the inverse of the spin magnitude  $S$ . In fact, each term  $\mathcal{H}_{\text{SW}}^{(l)}$  is of order  $O(S^{2-l/2})$ . In this work, in order to evaluate the lowest order effects on the response to the  $J$  and  $U$  modulations, we deal with fluctuation effects on the response functions up to order  $O(S^0)$ . Hence, the expansion (4.6) is stopped at  $l = 4$ . A similar analysis of another quantum spin system has been made in Ref. [158].

Let us explain details of the terms  $\mathcal{H}_{\text{SW}}^{(0)}$ ,  $\mathcal{H}_{\text{SW}}^{(1)}$ ,  $\mathcal{H}_{\text{SW}}^{(2)}$ , and  $\mathcal{H}_{\text{SW}}^{(3)}$  in the HP expansion (4.6), respectively. First of all, the zeroth order term  $\mathcal{H}_{\text{SW}}^{(0)}$  is equal to the ground state energy with no fluctuation

$$\begin{aligned}\mathcal{H}_{\text{SW}}^{(0)} &= N(A_0 + \tilde{A}_0) \\ &= NE^{\text{MF}}(\theta_{\text{mf}}),\end{aligned}$$

where  $E^{\text{MF}}(\theta_{\text{mf}})$  is the mean-field energy (2.47) of the ground state (see Sec. 2.5.4). Notice that we use  $N$  as the total lattice number throughout this Chapter.

Next, the linear term  $\mathcal{H}_{\text{SW}}^{(1)} = O(S^{3/2})$  is given by

$$\mathcal{H}_{\text{SW}}^{(1)} = \sqrt{N}(A_1 + \tilde{A}_1)(b_{1,0}^\dagger + b_{1,0}) + \sqrt{N}(B_1 + \tilde{B}_1)(b_{2,0}^\dagger + b_{2,0}). \quad (4.7)$$

For the mean-field ground state, we can easily verify that  $\mathcal{H}_{\text{SW}}^{(1)} = 0$ .

The quadratic term  $\mathcal{H}_{\text{SW}}^{(2)} = O(S)$  can be written as a matrix form

$$\mathcal{H}_{\text{SW}}^{(2)} = \delta E_2 + \sum_{\lambda=1}^4 \sum_{\nu=1}^4 \sum_{\mathbf{k} \in \Lambda_0} b_{\lambda,\mathbf{k}}^\dagger (\mathbf{H}_{\mathbf{k}})_{\lambda\nu} b_{\nu,\mathbf{k}}, \quad (4.8)$$

where  $\vec{b}_{\mathbf{k}} = (b_{1,\mathbf{k}}, b_{2,\mathbf{k}}, b_{3,\mathbf{k}}, b_{4,\mathbf{k}})^T$  and  $(b_{3,\mathbf{k}}, b_{4,\mathbf{k}}) = (b_{1,-\mathbf{k}}^\dagger, b_{2,-\mathbf{k}}^\dagger)$ . The four dimensional square matrix  $\mathbf{H}_{\mathbf{k}}$  is

$$\mathbf{H}_{\mathbf{k}} = \begin{pmatrix} f_{11}(\mathbf{k}) & f_{12}(\mathbf{k}) & g_{11}(\mathbf{k}) & g_{12}(\mathbf{k}) \\ f_{21}(\mathbf{k}) & f_{22}(\mathbf{k}) & g_{21}(\mathbf{k}) & g_{22}(\mathbf{k}) \\ g_{11}(\mathbf{k}) & g_{12}(\mathbf{k}) & f_{11}(\mathbf{k}) & f_{12}(\mathbf{k}) \\ g_{21}(\mathbf{k}) & g_{22}(\mathbf{k}) & f_{21}(\mathbf{k}) & f_{22}(\mathbf{k}) \end{pmatrix}. \quad (4.9)$$

The matrix elements of  $\mathbf{H}_{\mathbf{k}}$  are given by

$$\begin{aligned} f_{11}(\mathbf{k}) &= (A_2 + \tilde{A}_2 - 2A_0 - \tilde{A}_0 + E_2\gamma_{\mathbf{k}})/2, \\ f_{12}(\mathbf{k}) &= f_{21}(\mathbf{k}) = (B_2 + \tilde{B}_2 + F_2\gamma_{\mathbf{k}})/2, \\ f_{22}(\mathbf{k}) &= (\tilde{C}_2 - 2A_0 - \tilde{A}_0 + I_2\gamma_{\mathbf{k}})/2, \\ g_{11}(\mathbf{k}) &= D_2\gamma_{\mathbf{k}}, \\ g_{12}(\mathbf{k}) &= g_{21}(\mathbf{k}) = G_2\gamma_{\mathbf{k}}/2, \\ g_{22}(\mathbf{k}) &= H_2\gamma_{\mathbf{k}}, \end{aligned}$$

where  $\gamma_{\mathbf{k}} = (\cos k_x + \cos k_y + \cos k_z)/3$ . At  $n_0 \gg 1$ ,  $f_{12}(\mathbf{k}) = f_{21}(\mathbf{k}) = g_{12}(\mathbf{k}) = g_{21}(\mathbf{k}) = 0$ . Thus,  $\mathcal{H}_{\text{SW}}^{(2)}$  has no mixing term such as  $b_{1,\mathbf{k}}^\dagger b_{2,\mathbf{k}}$ , and we can treat each part labeled by 1 or 2 as an independent branch on each other. This feature stems from the explicit particle-hole symmetry of the effective pseudospin-one model for  $n_0 \gg 1$  (see also Sec. 2.5.2). Indeed, terms with an odd number of  $b_{2,\mathbf{k}}$  are forbidden by the particle-hole symmetry because an exchange between a particle  $t_{1,i}$  and hole  $t_{-1,i}$  leads to a change of the sign of  $b_{2,\mathbf{k}}$  while such a transformation remains the sign of  $b_{1,\mathbf{k}}$ . On the other hand, at lower filling rates, there is no reason that the mixing terms disappear.

Note that we can regard the constant part  $\delta E_2 = -\sum_{\mathbf{k} \in \Lambda_0} (f_{11}(\mathbf{k}) + f_{22}(\mathbf{k}))$  as a quantum fluctuation correction to the mean-field energy of the ground state  $\mathcal{H}_{\text{SW}}^{(0)}(\theta_{\text{mf}}, \chi_{\text{mf}})$ . The detailed discussion will be presented in Sec. 4.2.4.

The cubic term  $\mathcal{H}_{\text{SW}}^{(3)}$  can be also written as a simple form

$$\mathcal{H}_{\text{SW}}^{(3)} = \frac{1}{\sqrt{N}} \prod_{i=1}^3 \sum_{\lambda_i=1}^4 \sum_{\mathbf{k}_i \in \Lambda_0} C_{p_{\lambda_1} \mathbf{k}_1, p_{\lambda_2} \mathbf{k}_2, p_{\lambda_3} \mathbf{k}_3}^{(\lambda_1 \lambda_2 \lambda_3)} \delta_{\mathbf{k}_1 + \mathbf{k}_2 + \mathbf{k}_3, \mathbf{0}} b_{\lambda_1, \mathbf{k}_1} b_{\lambda_2, \mathbf{k}_2} b_{\lambda_3, \mathbf{k}_3}, \quad (4.10)$$

where  $p_\lambda = 1$  (for  $\lambda = 1, 2$ ) or  $p_\lambda = -1$  (for  $\lambda = 3, 4$ ). In addition,  $\delta_{\mathbf{k}_1 + \mathbf{k}_2 + \mathbf{k}_3, \mathbf{0}}$  is the momentum conservation law satisfied under scattering processes among the three spin waves. The coefficients of the vertices  $C_{\mathbf{k}_1, \mathbf{k}_2, \mathbf{k}_3}^{(\lambda_1 \lambda_2 \lambda_3)}$  which characterize properties of the scattering of the spin wave are given by

$$\begin{aligned} C_{\mathbf{k}_1, \mathbf{k}_2, \mathbf{k}_3}^{(331)} &= C_{\mathbf{k}_1, \mathbf{k}_2, \mathbf{k}_3}^{(131)} = (A_3 - A_1) \gamma_{\mathbf{k}_1}, \\ C_{\mathbf{k}_1, \mathbf{k}_2, \mathbf{k}_3}^{(342)} &= C_{\mathbf{k}_1, \mathbf{k}_2, \mathbf{k}_3}^{(142)} = -A_1 \gamma_{\mathbf{k}_1}, \\ C_{\mathbf{k}_1, \mathbf{k}_2, \mathbf{k}_3}^{(431)} &= C_{\mathbf{k}_1, \mathbf{k}_2, \mathbf{k}_3}^{(231)} = (B_3 - B_1) \gamma_{\mathbf{k}_1}, \\ C_{\mathbf{k}_1, \mathbf{k}_2, \mathbf{k}_3}^{(442)} &= C_{\mathbf{k}_1, \mathbf{k}_2, \mathbf{k}_3}^{(242)} = -B_1 \gamma_{\mathbf{k}_1}, \\ C_{\mathbf{k}_1, \mathbf{k}_2, \mathbf{k}_3}^{(341)} &= C_{\mathbf{k}_1, \mathbf{k}_2, \mathbf{k}_3}^{(132)} = C_3 \gamma_{\mathbf{k}_1}, \\ C_{\mathbf{k}_1, \mathbf{k}_2, \mathbf{k}_3}^{(332)} &= C_{\mathbf{k}_1, \mathbf{k}_2, \mathbf{k}_3}^{(141)} = D_3 \gamma_{\mathbf{k}_1}, \\ C_{\mathbf{k}_1, \mathbf{k}_2, \mathbf{k}_3}^{(432)} &= C_{\mathbf{k}_1, \mathbf{k}_2, \mathbf{k}_3}^{(241)} = E_3 \gamma_{\mathbf{k}_1}, \\ C_{\mathbf{k}_1, \mathbf{k}_2, \mathbf{k}_3}^{(441)} &= C_{\mathbf{k}_1, \mathbf{k}_2, \mathbf{k}_3}^{(232)} = F_3 \gamma_{\mathbf{k}_1}, \end{aligned}$$

and the others are identically zero. At  $n_0 \gg 1$ ,  $C_{\mathbf{k}_1, \mathbf{k}_2, \mathbf{k}_3}^{(431)} = C_{\mathbf{k}_1, \mathbf{k}_2, \mathbf{k}_3}^{(231)} = C_{\mathbf{k}_1, \mathbf{k}_2, \mathbf{k}_3}^{(442)} = C_{\mathbf{k}_1, \mathbf{k}_2, \mathbf{k}_3}^{(242)} = C_{\mathbf{k}_1, \mathbf{k}_2, \mathbf{k}_3}^{(341)} = C_{\mathbf{k}_1, \mathbf{k}_2, \mathbf{k}_3}^{(132)} = C_{\mathbf{k}_1, \mathbf{k}_2, \mathbf{k}_3}^{(332)} = C_{\mathbf{k}_1, \mathbf{k}_2, \mathbf{k}_3}^{(141)} = 0$  because each vertex characterized by the corresponding coefficient has an odd number of  $b_{2, \mathbf{k}}$ .

Finally, we mention a note on the quartic term  $\mathcal{H}_{\text{SW}}^{(4)}$ . In this work, the quartic term does not enter into the practical analysis of the response functions. The reason is explained in Sec. 4.2.4.

### 4.2.3 Bogoliubov transformation

In the previous section we have performed the HP expansion of the Hamiltonian (4.5) and discussed properties of each part  $\mathcal{H}_{\text{SW}}^{(l)}$ . In this section we discuss a Bogoliubov transformation of the quadratic Hamiltonian  $\mathcal{H}_{\text{SW}}^{(2)}$  and consider the resulting transformation of  $\mathcal{H}_{\text{SW}}^{(3)}$ .

Let us define a Bogoliubov transformation

$$\vec{b}_{\mathbf{k}} = \mathbf{W}_{\mathbf{k}} \vec{\beta}_{\mathbf{k}}, \quad \vec{\beta}_{\mathbf{k}} = \mathbf{W}_{\mathbf{k}}^{-1} \vec{b}_{\lambda, \mathbf{k}}, \quad (4.11)$$

where  $\vec{\beta}_{\mathbf{k}} = (\beta_{1, \mathbf{k}}, \beta_{2, \mathbf{k}}, \beta_{3, \mathbf{k}}, \beta_{4, \mathbf{k}})^T$ ,  $\beta_{3, \mathbf{k}} \equiv \beta_{1, -\mathbf{k}}^\dagger$ ,  $\beta_{4, \mathbf{k}} \equiv \beta_{2, -\mathbf{k}}^\dagger$ ,  $[\beta_{m, \mathbf{k}}, \beta_{n, \mathbf{k}'}^\dagger] = \delta_{m, n} \delta_{\mathbf{k}, \mathbf{k}'}$  (for  $m, n = 1, 2$ ),

and  $[\beta_{m,\mathbf{k}}, \beta_{n,\mathbf{k}'}] = [\beta_{m,\mathbf{k}}^\dagger, \beta_{n,\mathbf{k}'}^\dagger] = 0$ . In general, the matrix elements of  $W_{\mathbf{k}}$  can be written as

$$W_{\mathbf{k}} = \begin{pmatrix} u_{11}(\mathbf{k}) & u_{12}(\mathbf{k}) & v_{11}(\mathbf{k}) & v_{12}(\mathbf{k}) \\ u_{21}(\mathbf{k}) & u_{22}(\mathbf{k}) & v_{21}(\mathbf{k}) & v_{22}(\mathbf{k}) \\ v_{11}^*(-\mathbf{k}) & v_{12}^*(-\mathbf{k}) & u_{11}^*(-\mathbf{k}) & u_{12}^*(-\mathbf{k}) \\ v_{21}^*(-\mathbf{k}) & v_{22}^*(-\mathbf{k}) & u_{21}^*(-\mathbf{k}) & u_{22}^*(-\mathbf{k}) \end{pmatrix}. \quad (4.12)$$

The transformation  $W_{\mathbf{k}}$  fulfills a condition

$$W_{\mathbf{k}} g W_{\mathbf{k}}^\dagger = W_{\mathbf{k}}^\dagger g W_{\mathbf{k}} = g, \quad (4.13)$$

where  $g = \text{diag}(1, 1, -1, -1)$  is the metric tensor in the Minkowski space  $\mathbb{M}^{2\otimes 2}$ , because of the Bose statistics of the new operators. In addition, in order to diagonalize  $\mathcal{H}_{\text{SW}}^{(2)}$  so that

$$\mathcal{H}_{\text{SW}}^{(2)} = \delta E_2 + \sum_{\lambda=1}^4 \sum_{\nu=1}^4 \sum_{\mathbf{k} \in \Lambda_0} \beta_{\lambda,\mathbf{k}}^\dagger (D_{\mathbf{k}})_{\lambda\nu} \beta_{\nu,\mathbf{k}}, \quad (4.14)$$

where  $D_{\mathbf{k}} = \text{diag}(e_1(\mathbf{k}), e_2(\mathbf{k}), e_3(\mathbf{k}), e_4(\mathbf{k}))$  is a diagonal matrix, we impose on the matrix  $W_{\mathbf{k}}$  a condition

$$W_{\mathbf{k}}^{-1} (g H_{\mathbf{k}}) W_{\mathbf{k}} = g D_{\mathbf{k}}. \quad (4.15)$$

Solving the eigenvalue problem of the non-Hermite matrix  $g H_{\mathbf{k}}$  defined by Eqs (4.13) and (4.15), we obtain the specific form of  $W_{\mathbf{k}}$  and dispersion relations  $\mathcal{E}_{1,\mathbf{k}} = e_1(\mathbf{k}) + e_3(\mathbf{k})$  of  $\beta_{1,\mathbf{k}}$  and  $\mathcal{E}_{2,\mathbf{k}} = e_2(\mathbf{k}) + e_4(\mathbf{k})$  of  $\beta_{2,\mathbf{k}}$ . Notice that the dispersions  $\mathcal{E}_{1,\mathbf{k}}$  and  $\mathcal{E}_{2,\mathbf{k}}$  correspond to the Higgs and NG modes, respectively. For more details of the eigenvalue problem of  $g H_{\mathbf{k}}$ , see Ref. [92].

At  $n_0 \gg 1$ , the different sectors labeled by 1 or 2 are completely decoupled, so that we can easily diagonalize  $g H_{\mathbf{k}}$  and obtain the dispersion relations of the collective modes and coefficient matrix  $W_{\mathbf{k}}$  as analytical forms. Indeed, taking this limit, we obtain again Eqs. (2.59) and (2.60):

$$W_{\mathbf{k}} \rightarrow \begin{pmatrix} u_{1,\mathbf{k}} & 0 & v_{1,\mathbf{k}} & 0 \\ 0 & u_{2,\mathbf{k}} & 0 & v_{2,\mathbf{k}} \\ v_{1,-\mathbf{k}}^* & 0 & u_{1,-\mathbf{k}}^* & 0 \\ 0 & v_{2,-\mathbf{k}}^* & 0 & u_{2,-\mathbf{k}}^* \end{pmatrix}. \quad (4.16)$$

On the other hand, at lower filling rates, to compute  $W_{\mathbf{k}}$  and the dispersion relations is possible but more complicated than the large filling case. In this paper, we calculate them by a numerical diagonalization of the non-Hermite matrix  $g H_{\mathbf{k}}$ . The analytic expressions of the dispersion relations in the superfluid phase at an arbitrary filling rate have been obtained in Ref. [92].

After the Bogoliubov transformation of the quadratic part  $\mathcal{H}_{\text{SW}}^{(2)}$ , the cubic term  $\mathcal{H}_{\text{SW}}^{(3)}$  becomes

$$\mathcal{H}_{\text{SW}}^{(3)} = \frac{1}{\sqrt{N}} \prod_{i=1}^3 \sum_{\lambda_i=1}^4 \sum_{\mathbf{k}_i \in \Lambda_0} M_{p_{\lambda_1 \mathbf{k}_1}, p_{\lambda_2 \mathbf{k}_2}, p_{\lambda_3 \mathbf{k}_3}}^{(\lambda_1 \lambda_2 \lambda_3)} \delta_{\mathbf{k}_1 + \mathbf{k}_2 + \mathbf{k}_3, \mathbf{0}} \beta_{\lambda_1, \mathbf{k}_1} \beta_{\lambda_2, \mathbf{k}_2} \beta_{\lambda_3, \mathbf{k}_3}. \quad (4.17)$$

Here, the new coefficients  $M_{\mathbf{k}_1, \mathbf{k}_2, \mathbf{k}_3}^{(\lambda_1, \lambda_2, \lambda_3)}$  are related to  $C_{\mathbf{k}_1, \mathbf{k}_2, \mathbf{k}_3}^{(\lambda_1, \lambda_2, \lambda_3)}$  by a relation

$$M_{p_{\lambda_1} \mathbf{k}_1, p_{\lambda_2} \mathbf{k}_2, p_{\lambda_3} \mathbf{k}_3}^{(\lambda_1, \lambda_2, \lambda_3)} = \sum_{\nu_1, \nu_2, \nu_3=1}^4 C_{p_{\nu_1} \mathbf{k}_1, p_{\nu_2} \mathbf{k}_2, p_{\nu_3} \mathbf{k}_3}^{(\nu_1, \nu_2, \nu_3)} (W_{\mathbf{k}_1})_{\nu_1}^{\lambda_1} (W_{\mathbf{k}_2})_{\nu_2}^{\lambda_2} (W_{\mathbf{k}_3})_{\nu_3}^{\lambda_3}. \quad (4.18)$$

The coefficients  $M_{\mathbf{k}_1, \mathbf{k}_2, \mathbf{k}_3}^{(\lambda_1, \lambda_2, \lambda_3)}$  characterize the interactions among the three collective modes of the diagonalized basis. For  $n_0 \gg 1$ , processes with an odd number of the NG modes are prohibited due to the explicit particle-hole symmetry of the effective model (2.44). On the other hand, the effective model at lower filling rates (2.45) has no longer such a symmetry, thus, permits not only the even-NG processes but also the odd-NG processes. As we will see in Sec. 4.3.3 in contrast to the large filling case, new types of contribution to the response properties emerge due to the physical background.

#### 4.2.4 Normal ordering

So far we have discussed the Bogoliubov transformation of the spin-wave Hamiltonian  $\mathcal{H}_{\text{SW}}$ . Obviously, the resulting Hamiltonian after the Bogoliubov transformation is not normal ordered with respect to the Bogoliubov operators  $\beta_{m, \mathbf{k}}$ . In Sec. 4.3, we will apply the field theoretical methods for the spin-wave Hamiltonian in order to calculate the response functions. Therefore, it is necessary to obtain a normal ordered form of  $\mathcal{H}_{\text{SW}}$ .

Let us consider the normal ordering of the quadratic spin-wave Hamiltonian,  $\mathcal{H}_{\text{SW}}^{(2)}$ . In the following discussion, a notation  $: \cdot :$  represents a normal ordered operator with respect to the Bogoliubov operators. In the quadratic Hamiltonian, each out of normal ordered term produces a constant shift after permutations between the canonical operators  $\beta_{m, \mathbf{k}}$  and  $\beta_{m, \mathbf{k}}^\dagger$ . Thus the quadratic Hamiltonian can be rewritten as

$$\mathcal{H}_{\text{SW}}^{(2)} = \delta E_2 + \delta \tilde{E}_2 + : \tilde{\mathcal{H}}_{\text{SW}}^{(2)} :,$$

where  $\delta \tilde{E}_2$  is the resulting constant shift arising after  $\tilde{\mathcal{H}}_{\text{SW}}^{(2)}$  is normal ordered. In a similar way, the cubic and quartic Hamiltonians,  $\mathcal{H}_{\text{SW}}^{(3)}$  and  $\mathcal{H}_{\text{SW}}^{(4)}$ , become

$$\begin{aligned} \mathcal{H}_{\text{SW}}^{(3)} &= : \mathcal{H}_{\text{SW}}^{(3)} : + \delta \mathcal{H}_{\text{SW}}^{(1)}, \\ \mathcal{H}_{\text{SW}}^{(4)} &= \delta E_4 + : \delta \mathcal{H}_{\text{SW}}^{(2)} : + : \mathcal{H}_{\text{SW}}^{(4)} :, \end{aligned}$$

where  $\delta \mathcal{H}_{\text{SW}}^{(1)}$ ,  $\delta E_4$ , and  $: \delta \mathcal{H}_{\text{SW}}^{(2)} :$  are the resulting linear, constant, and quadratic shifts arising after making the cubic and quartic Hamiltonians normal ordered.

The total shift  $\delta E_2 + \delta \tilde{E}_2 + \delta E_4$  can be interpreted as a fluctuation correction to the mean-field energy of the ground state  $\mathcal{H}_{\text{SW}}^{(0)}$  [92]. The first two terms represent  $1/S$  corrections to the

ground-state energy and the last term is a higher order correction of order  $1/S^2$ . To minimize the modified ground-state energy with respect to  $\theta$  and  $\chi$  leads to a renormalization of the variational parameters of the mean-field configuration:  $\theta_{\text{mf}} \rightarrow \theta_{\text{ren}} = \theta_{\text{mf}} + \delta\theta_{\text{cor}}$  and  $\chi_{\text{mf}} \rightarrow \chi_{\text{ren}} = \chi_{\text{mf}} + \delta\chi_{\text{cor}}$ . This corresponds to a reduction of the order-parameter amplitude induced by quantum and thermal fluctuations. At the renormalized configuration, the linear term including the shift from the cubic Hamiltonian  $\mathcal{H}_{\text{SW}}^{(3)}$  becomes zero:  $\mathcal{H}_{\text{SW}}^{(1)} + \delta\mathcal{H}_{\text{SW}}^{(1)} = 0$ . Moreover, the renormalized parameters and additional quadratic term :  $\delta\mathcal{H}_{\text{SW}}^{(2)}$  : stemming from the quartic Hamiltonian  $\mathcal{H}_{\text{SW}}^{(4)}$  modify the band energies  $\mathcal{E}_{1,\mathbf{k}}$  and  $\mathcal{E}_{2,\mathbf{k}}$  calculated within the mean-field approximation.

Although it is naively expected that inclusion of the renormalization effect induced by fluctuations should make the results more quantitative, it leads to a theoretical difficulty concerned with spectral properties of the NG mode. If we deal with the renormalization effect on the basis of our perturbative scheme around the mean-field ground state, then we are confronted with a situation in which a finite energy gap opens in the NG mode branch. In general, the gap of the NG mode must vanish in the symmetry broken phase, so that the appearance of the finite gap is an artifact of our naive perturbative approach. Moreover, whether the finite gap exists or not in the low energy sector of the NG mode spectrum strongly affects the decay processes of the Higgs mode because the possible scattering channels are restricted by the on-shell energy-momentum conservation laws between the low-energy collective modes [46]. Thus, in order to describe the stability of the Higgs mode corresponding to experiments, we need to eliminate the finite gap from the NG mode branch.

The similar problem also appears in the Hartree–Fock–Bogoliubov approximation of single component dilute Bose gases [68, 159–161]. In this scheme, the artificial energy gap of the NG or Bogoliubov mode is often eliminated by the conventional Popov–Shohnho prescription [68, 161, 162] in which an anomalous average of boson operators is detuned so that the artificial gap vanishes. Our bosons in the current problem have two components, so that the application of the similar prescription for our case is not straightforward. Therefore, in this work, we do neglect the modification of the mean-field variational parameters as a simpler prescription. Our prescription here is similar in spirit to the standard Bogoliubov approximation for dilute Bose gases [121], and is expected to be better as the spatial dimension of the system increases and the temperature decreases.

In addition to the prescription, we also neglect the normal-ordered quartic term :  $\mathcal{H}_{\text{SW}}^{(4)}$  : throughout our analysis. Within our lowest order  $O(S^0)$ , the term only generates a shift of the peak position of the Higgs mode but no contribution to the peak width. Moreover, the shift is expected to be rather small at sufficiently low temperatures. Thus it makes no important difference whether the quartic term exists or not, as far as the problem of the stability of the Higgs mode is

concerned.

Finally, the above discussions are summarized as the following normal-ordered Hamiltonian:

$$\mathcal{H}_{\text{SW}} = \text{const.} + : \tilde{\mathcal{H}}_{\text{SW}}^{(2)} : + : \mathcal{H}_{\text{SW}}^{(3)} : . \quad (4.19)$$

In the next section, we will compute the fluctuation corrections to the response functions practically by using the final Hamiltonian (4.19).

## 4.3 Linear response analysis

In this section, we analyze the response functions (4.1) and (4.3) combining the methods developed in Sec. 4.2 and finite-temperature Green's function theory. The basis of this theory is explained in Refs. [163–165].

### 4.3.1 Response functions

We express the  $K$ -to- $K$  response function (4.1) in terms of the Bogoliubov operators  $\beta_{m,\mathbf{k}}$ . Using the HP expansion (2.57) and Bogoliubov transformation, the kinetic energy  $K$  becomes

$$K = NA_0 + \sqrt{N}\Upsilon_1(\beta_{1,0}^\dagger + \beta_{1,0}) + \dots, \quad (4.20)$$

where the coefficient  $\Upsilon_1$  is defined by

$$\Upsilon_1 = A_1[u_{11}(\mathbf{0}) + v_{11}(\mathbf{0})] + B_1[u_{21}(\mathbf{0}) + v_{21}(\mathbf{0})]. \quad (4.21)$$

It should be noted that  $\dots$  in Eq. (4.20) includes the term proportional to  $\beta_{2,0} + \beta_{2,0}^\dagger$ . Here  $\beta_{2,0}$  corresponds to the zero energy mode of the system. We can easily check that the coefficient of  $\beta_{2,0} + \beta_{2,0}^\dagger$  should be zero because of the eigenvalue equation of  $(u_{12}(\mathbf{0}), v_{12}(\mathbf{0}), u_{22}(\mathbf{0}), v_{22}(\mathbf{0}))$  extracted from Eq. (4.15).

Therefore the zero mode contribution is eliminated in our analysis. Substituting (4.20) into the definition of  $D_{KK}^{\text{R}}(t-t')$  and keeping only leading order terms, we obtain

$$D_{KK}^{\text{R}}(t-t') = N|\Upsilon_1|^2 \left\{ G_{13,0}^{\text{R}}(t-t') + G_{31,0}^{\text{R}}(t-t') + G_{11,0}^{\text{R}}(t-t') + G_{33,0}^{\text{R}}(t-t') \right\}, \quad (4.22)$$

where we have introduced four types of retarded Green's function of the zero-momentum Higgs mode  $\beta_{1,0}$ ,

$$\begin{aligned} G_{13,0}^{\text{R}}(t-t') &= -i\Theta(t-t')\langle [\beta_{1,0}(t), \beta_{1,0}^\dagger(t')] \rangle_{\text{eq}}, \\ G_{11,0}^{\text{R}}(t-t') &= -i\Theta(t-t')\langle [\beta_{1,0}(t), \beta_{1,0}(t')] \rangle_{\text{eq}}, \\ G_{31,0}^{\text{R}}(t-t') &= -i\Theta(t-t')\langle [\beta_{1,0}^\dagger(t), \beta_{1,0}(t')] \rangle_{\text{eq}}, \\ G_{33,0}^{\text{R}}(t-t') &= -i\Theta(t-t')\langle [\beta_{1,0}^\dagger(t), \beta_{1,0}^\dagger(t')] \rangle_{\text{eq}}. \end{aligned}$$

Thus, up to the leading order, evaluating the response function  $D_{KK}^R(t-t')$  results in calculating these retarded functions of the Higgs mode. The Fourier transformation with respect to  $t-t'$  gives the dynamical susceptibility  $\chi_{KK}(\omega)$ , which characterizes the stability of the Higgs mode [see Eq. (4.2)].

Similarly, we can obtain the  $O$ -to- $O$  response function (4.3) written in terms of the Bogoliubov operators. Using the HP expansion (2.57) and Bogoliubov transformation, the onsite interaction energy  $O$  becomes

$$O = N\tilde{A}'_0 + \sqrt{N}\Upsilon_2(\beta_{1,\mathbf{0}}^\dagger + \beta_{1,\mathbf{0}}) + \dots, \quad (4.23)$$

where the coefficient  $\Upsilon_2$  is defined by

$$\Upsilon_2 = \tilde{A}'_1[u_{11}(\mathbf{0}) + v_{11}(\mathbf{0})], \quad (4.24)$$

and the constants  $\tilde{A}'_0$  and  $\tilde{A}'_1$  are given by

$$\tilde{A}'_0 = \frac{1}{2}s_1^2, \quad \tilde{A}'_1 = -\frac{1}{2}s_1c_1. \quad (4.25)$$

For the same reason of the zero-mode coefficient vanishing in  $K$ , the onsite energy  $O$  has also no term of  $\beta_{2,\mathbf{0}} + \beta_{2,\mathbf{0}}^\dagger$ .

Substituting (4.23) into the definition of  $D_{OO}^R(t-t')$  and keeping only leading order terms, we obtain

$$D_{OO}^R(t-t') = N|\Upsilon_2|^2 \left\{ G_{13,\mathbf{0}}^R(t-t') + G_{31,\mathbf{0}}^R(t-t') + G_{11,\mathbf{0}}^R(t-t') + G_{33,\mathbf{0}}^R(t-t') \right\}. \quad (4.26)$$

The dynamical susceptibility  $\chi_{OO}(\omega)$  is given by the Fourier transformation of this quantity [see Eq. (4.4)].

Within the leading order, the  $O$ -to- $O$  response function has the same form as the  $K$ -to- $K$  response function except for its coefficients  $|\Upsilon_1|^2$  and  $|\Upsilon_2|^2$ . In Fig. 4.1, we show the chemical potential dependence of the coefficients at  $\bar{n} = n_0 = 1$  and  $u = 1$ . The point indicated by a solid arrow in Fig. 4.1 is at the commensurate filling rate  $n_0$ , and the corresponding chemical potential is expressed by  $\mu_{n_0}$  whose explicit form is presented by Eq. (2.53). As shown in Fig. 4.1, the coefficients are found to completely coincide with each other for any  $\mu$ , so that there is no difference between two response functions, at least, within our approximate calculation. Notice that the similar coincidence occurs for other values of  $n_0$  and  $u$ .

### 4.3.2 Imaginary-time Green's functions

In this paper, we calculate the response functions by means of perturbative methods of the imaginary-time Green's functions. Let us define three time-ordered *normal* or *anomalous* Green's functions

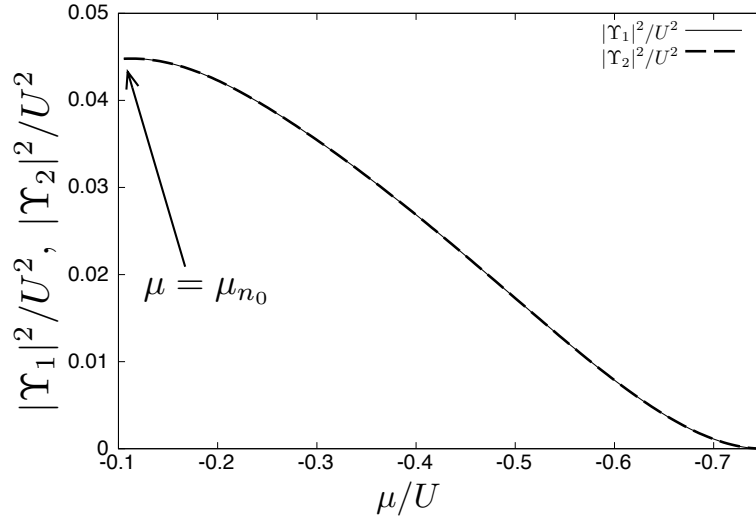


Figure 4.1: Chemical potential dependence of the coefficients  $|\Upsilon_1|^2$  and  $|\Upsilon_2|^2$ . We choose the specific parameters  $n_0 = 1$  and  $u = 1$  ( $zJ/U = 0.25$ ). The solid and dashed lines represent  $|\Upsilon_1|^2/U^2$  and  $|\Upsilon_2|^2/U^2$ , which characterize the response magnitude of the hopping and onsite-interaction modulations, respectively. The point indicated by the solid arrow corresponds to the unit filling rate  $\bar{n} = n_0 = 1$ . The mean filling rate  $\bar{n}$  decreases as the chemical potential  $\mu$  decreases. After decreasing below  $\mu \approx -0.75$ ,  $\bar{n}$  becomes zero.

on an imaginary time axis [163–165]:

$$\begin{aligned} G_{1,\mathbf{k}}(\tau - \tau') &= -\langle T_\tau \beta_{1,\mathbf{k}}(\tau) \beta_{1,\mathbf{k}}^\dagger(\tau') \rangle_{\text{eq}} + \langle \beta_{1,0}(0) \rangle_{\text{eq}} \langle \beta_{1,0}^\dagger(0) \rangle_{\text{eq}}, \\ F_{1,\mathbf{k}}(\tau - \tau') &= -\langle T_\tau \beta_{1,\mathbf{k}}(\tau) \beta_{1,-\mathbf{k}}(\tau') \rangle_{\text{eq}} + \langle \beta_{1,0}(0) \rangle_{\text{eq}}^2, \\ F_{1,\mathbf{k}}^\dagger(\tau - \tau') &= -\langle T_\tau \beta_{1,-\mathbf{k}}^\dagger(\tau) \beta_{1,\mathbf{k}}^\dagger(\tau') \rangle_{\text{eq}} + \langle \beta_{1,0}^\dagger(0) \rangle_{\text{eq}}^2. \end{aligned}$$

Here  $T_\tau$  is the imaginary-time ordering operator and  $\tau, \tau' \in [0, \beta]$ . These functions are periodic with respect to the inverse temperature  $\beta$  [163–165]. Thus the Fourier components are given by

$$\begin{aligned} \mathcal{G}_{1,\mathbf{k}}(i\omega_n) &= \int_0^\beta d\tau G_{1,\mathbf{k}}(\tau) e^{i\omega_n \tau}, \\ \mathcal{F}_{1,\mathbf{k}}(i\omega_n) &= \int_0^\beta d\tau F_{1,\mathbf{k}}(\tau) e^{i\omega_n \tau}, \\ \mathcal{F}_{1,\mathbf{k}}^\dagger(i\omega_n) &= \int_0^\beta d\tau F_{1,\mathbf{k}}^\dagger(\tau) e^{i\omega_n \tau}, \end{aligned}$$

where  $\omega_n = 2\pi n/\beta$  ( $n \in \mathbb{N}$ ) is the Matsubara frequency [163–165]. It should be noted that a relation  $\mathcal{F}_{1,\mathbf{k}}^\dagger(i\omega_n) = \mathcal{F}_{1,\mathbf{k}}(-i\omega_n)$  holds for any  $n$ , at least, within our leading order  $O(S^0)$ . In fact, this is verified by a straightforward calculation based on the perturbative expansion. According to more general consideration [164], this relation is expected to be true at any order of the perturbative expansion.

For a fixed  $\omega_n$ , the imaginary-time Green's functions  $\mathcal{G}(i\omega_n)$  and  $\mathcal{F}(i\omega_n)$  fulfill the Dyson's equations [163, 164]

$$\begin{aligned}\mathcal{G}_{1,0}(i\omega_n) &= \mathcal{G}_{1,0}^{(0)}(i\omega_n) + \mathcal{G}_{1,0}^{(0)}(i\omega_n)\Sigma_{11}(i\omega_n)\mathcal{G}_{1,0}(i\omega_n) + \mathcal{G}_{1,0}^{(0)}(i\omega_n)\Sigma_{02}(i\omega_n)\mathcal{F}_{1,0}(-i\omega_n), \\ \mathcal{F}_{1,0}(i\omega_n) &= \mathcal{G}_{1,0}^{(0)}(i\omega_n)\Sigma_{11}(i\omega_n)\mathcal{F}_{1,0}(i\omega_n) + \mathcal{G}_{1,0}^{(0)}(i\omega_n)\Sigma_{02}(i\omega_n)\mathcal{G}_{1,0}(-i\omega_n),\end{aligned}$$

where  $\Sigma_{11}(i\omega_n)$  and  $\Sigma_{02}(i\omega_n)$  are the self-energy functions of the normal and anomalous Green's functions. Here,  $\mathcal{G}_{1,0}^{(0)}(i\omega_n) = 1/(i\omega_n - \Delta)$  is the free propagator of the Higgs mode with its energy gap  $\Delta$  at zero momentum. The formal solutions [163, 164] are

$$\begin{aligned}\mathcal{G}_{1,0}(i\omega_n) &= -\frac{1}{D} \left\{ \left[ \mathcal{G}_{1,0}^{(0)}(-i\omega_n) \right]^{-1} - \Sigma_{11}(-i\omega_n) \right\}, \\ \mathcal{F}_{1,0}(i\omega_n) &= -\frac{1}{D} \Sigma_{02}(i\omega_n),\end{aligned}$$

where its denominator  $D$  is given by

$$D = [\Sigma_{02}(i\omega_n)]^2 - [i\omega_n - \Delta - \Sigma_{11}(i\omega_n)] [-i\omega_n - \Delta - \Sigma_{11}(-i\omega_n)].$$

In terms with the Fourier components of the Green's functions, the dynamical susceptibilities  $\chi_{KK}(\omega)$  and  $\chi_{OO}(\omega)$  read

$$\chi_{KK}(\omega) = N|\Upsilon_1|^2 \left\{ g(\omega) + f(\omega) + \bar{g}(\omega) + \bar{f}(\omega) \right\}, \quad (4.27)$$

$$\chi_{OO}(\omega) = N|\Upsilon_2|^2 \left\{ g(\omega) + f(\omega) + \bar{g}(\omega) + \bar{f}(\omega) \right\}. \quad (4.28)$$

The analytically continued functions

$$\begin{aligned}g(\omega) &= \mathcal{G}_{1,0}(i\omega_n)|_{i\omega_n \rightarrow \omega+i\epsilon}, \quad f(\omega) = \mathcal{F}_{1,0}(i\omega_n)|_{i\omega_n \rightarrow \omega+i\epsilon}, \\ \bar{g}(\omega) &= \mathcal{G}_{1,0}(-i\omega_n)|_{i\omega_n \rightarrow \omega+i\epsilon}, \\ \bar{f}(\omega) &= \mathcal{F}_{1,0}^\dagger(i\omega_n)|_{i\omega_n \rightarrow \omega+i\epsilon} = \mathcal{F}_{1,0}(-i\omega_n)|_{i\omega_n \rightarrow \omega+i\epsilon},\end{aligned}$$

are nothing but the retarded (real time) Green's functions  $G_{13,0}^R(\omega)$ ,  $G_{11,0}^R(\omega)$ ,  $G_{31,0}^R(\omega)$ , and  $G_{33,0}^R(\omega)$ . Here  $\epsilon$  is an infinitesimal and positive number. Thus we can obtain the dynamical susceptibilities when the self-energy functions  $\Sigma_{11}(i\omega_n)$  and  $\Sigma_{02}(i\omega_n)$  are known for all of  $n > 0$ .

### 4.3.3 Self-energy functions

At the level of the formal solutions of the Dyson's equations, the self-energy functions are still unknown. Here we compute them through a perturbative approximation of the normal and anomalous Green's functions. The lowest order contributions to the self-energy functions arise from the

$$\begin{aligned}
\mathcal{G}_{1,0}(i\omega_n) = & \leftarrow^{k=0, i\omega_n} \\
& + \left. \begin{array}{l}
\begin{array}{c} \text{Diagram 1} \\ \text{Diagram 2} \\ \text{Diagram 3} \end{array} \\
\begin{array}{c} \text{Diagram 4} \\ \text{Diagram 5} \\ \text{Diagram 6} \\ \text{Diagram 7} \end{array}
\end{array} \right\} \mathcal{G}_{1,0}(i\omega_n) \Sigma_{11}^{(a)} \mathcal{G}_{1,0}(i\omega_n) \\
& + \left. \begin{array}{l}
\begin{array}{c} \text{Diagram 8} \\ \text{Diagram 9} \\ \text{Diagram 10} \end{array} \\
\begin{array}{c} \text{Diagram 11} \\ \text{Diagram 12} \\ \text{Diagram 13} \end{array}
\end{array} \right\} \mathcal{G}_{1,0}(i\omega_n) \Sigma_{11}^{(b)} \mathcal{G}_{1,0}(i\omega_n) \\
& + \left. \begin{array}{l}
\begin{array}{c} \text{Diagram 14} \\ \text{Diagram 15} \end{array} \\
\begin{array}{c} \text{Diagram 16} \\ \text{Diagram 17} \end{array}
\end{array} \right\} \mathcal{G}_{1,0}(i\omega_n) \Sigma_{11}^{(c)} \mathcal{G}_{1,0}(i\omega_n) \\
& + \left. \begin{array}{l}
\begin{array}{c} \text{Diagram 18} \\ \text{Diagram 19} \\ \text{Diagram 20} \\ \text{Diagram 21} \end{array} \\
\begin{array}{c} \text{Diagram 22} \\ \text{Diagram 23} \\ \text{Diagram 24} \\ \text{Diagram 25} \end{array}
\end{array} \right\} \mathcal{G}_{1,0}(i\omega_n) \Sigma_{11}^{(d)} \mathcal{G}_{1,0}(i\omega_n)
\end{aligned}$$

Figure 4.2: Leading one-loop order contributions to the normal Green's function  $\mathcal{G}_{1,0}(i\omega_n)$ . The variables  $\mathbf{k}_1$  and  $i\omega_{n_1}$  added near the internal line implies the internal summation over the possible momentum and Matsubara frequency. The solid arrow denotes the propagator of the free Higgs mode while the dashed arrow denotes the propagator of the free NG mode. The self-energy function of each diagram is obtained by picking off its two external lines. The left arrow in the first column represents the zeroth order Green's function. The diagrams in each column form an individual group labeled by  $\Sigma_{11}^{(a)}(i\omega_n)$ ,  $\Sigma_{11}^{(b)}(i\omega_n)$ ,  $\Sigma_{11}^{(c)}(i\omega_n)$ , or  $\Sigma_{11}^{(d)}(i\omega_n)$ .

second order perturbation with respect to :  $\mathcal{H}_{\text{SW}}^{(3)}$  :. If we stop the expansion up to the lowest one-loop order, i.e.,  $O(S^0)$ , each self-energy function then contains twelve number of distinct contributions.

Let us compute the normal self-energy function  $\Sigma_{11}(i\omega_n)$ . In Fig. 4.2, we show the corresponding Feynman diagrams up to the one-loop order corrections. The contributions to the full self-energy function can be categorized into four parts,  $\Sigma_{11}(i\omega_n) = \Sigma_{11}^{(a)}(i\omega_n) + \Sigma_{11}^{(b)}(i\omega_n) + \Sigma_{11}^{(c)}(i\omega_n) + \Sigma_{11}^{(d)}(i\omega_n)$ . Within the lowest order each partial self-energy function is given by

$$\begin{aligned} \Sigma_{11}^{(a)}(i\omega_n) &= \frac{-1}{2N} \sum_{\mathbf{k}_1 \in \Lambda_0} M_{\mathbf{0}, \mathbf{k}_1, -\mathbf{k}_1}^{[333]} M_{\mathbf{k}_1, -\mathbf{k}_1, \mathbf{0}}^{[111]} \frac{1 + 2n_B[\mathcal{E}_{1, \mathbf{k}_1}]}{i\omega_n + 2\mathcal{E}_{1, \mathbf{k}_1}} - \frac{1}{2N} \sum_{\mathbf{k}_1 \in \Lambda_0} M_{\mathbf{0}, \mathbf{k}_1, -\mathbf{k}_1}^{[344]} M_{\mathbf{k}_1, -\mathbf{k}_1, \mathbf{0}}^{[221]} \frac{1 + 2n_B[\mathcal{E}_{2, \mathbf{k}_1}]}{i\omega_n + 2\mathcal{E}_{2, \mathbf{k}_1}} \\ &\quad - \frac{1}{N} \sum_{\mathbf{k}_1 \in \Lambda_0} M_{\mathbf{0}, \mathbf{k}_1, -\mathbf{k}_1}^{[334]} M_{-\mathbf{k}_1, \mathbf{k}_1, \mathbf{0}}^{[211]} \frac{1 + n_B[\mathcal{E}_{1, \mathbf{k}_1}] + n_B[\mathcal{E}_{2, \mathbf{k}_1}]}{i\omega_n + \mathcal{E}_{1, \mathbf{k}_1} + \mathcal{E}_{2, \mathbf{k}_1}}, \\ \Sigma_{11}^{(b)}(i\omega_n) &= \frac{1}{2N} \sum_{\mathbf{k}_1 \in \Lambda_0} M_{\mathbf{0}, \mathbf{k}_1, -\mathbf{k}_1}^{[311]} M_{\mathbf{k}_1, -\mathbf{k}_1, \mathbf{0}}^{[331]} \frac{1 + 2n_B[\mathcal{E}_{1, \mathbf{k}_1}]}{i\omega_n - 2\mathcal{E}_{1, \mathbf{k}_1}} + \frac{1}{2N} \sum_{\mathbf{k}_1 \in \Lambda_0} M_{\mathbf{0}, \mathbf{k}_1, -\mathbf{k}_1}^{[322]} M_{\mathbf{k}_1, -\mathbf{k}_1, \mathbf{0}}^{[441]} \frac{1 + 2n_B[\mathcal{E}_{2, \mathbf{k}_1}]}{i\omega_n - 2\mathcal{E}_{2, \mathbf{k}_1}} \\ &\quad + \frac{1}{N} \sum_{\mathbf{k}_1 \in \Lambda_0} M_{\mathbf{0}, \mathbf{k}_1, -\mathbf{k}_1}^{[312]} M_{\mathbf{k}_1, -\mathbf{k}_1, \mathbf{0}}^{[341]} \frac{1 + n_B[\mathcal{E}_{1, \mathbf{k}_1}] + n_B[\mathcal{E}_{2, \mathbf{k}_1}]}{i\omega_n - \mathcal{E}_{1, \mathbf{k}_1} - \mathcal{E}_{2, \mathbf{k}_1}}, \\ \Sigma_{11}^{(c)}(i\omega_n) &= -\frac{1}{N} \sum_{\mathbf{k}_1 \in \Lambda_0} M_{\mathbf{0}, \mathbf{k}_1, \mathbf{k}_1}^{[332]} M_{\mathbf{k}_1, \mathbf{k}_1, \mathbf{0}}^{[411]} \frac{n_B[\mathcal{E}_{2, \mathbf{k}_1}] - n_B[\mathcal{E}_{1, \mathbf{k}_1}]}{i\omega_n + \mathcal{E}_{1, \mathbf{k}_1} - \mathcal{E}_{2, \mathbf{k}_1}} - \frac{1}{N} \sum_{\mathbf{k}_1 \in \Lambda_0} M_{\mathbf{0}, \mathbf{k}_1, \mathbf{k}_1}^{[341]} M_{\mathbf{k}_1, \mathbf{k}_1, \mathbf{0}}^{[321]} \frac{n_B[\mathcal{E}_{1, \mathbf{k}_1}] - n_B[\mathcal{E}_{2, \mathbf{k}_1}]}{i\omega_n + \mathcal{E}_{2, \mathbf{k}_1} - \mathcal{E}_{1, \mathbf{k}_1}}, \\ \Sigma_{11}^{(d)}(i\omega_n) &= -\frac{1}{N} \sum_{\mathbf{k}_1 \in \Lambda_0} M_{\mathbf{0}, \mathbf{0}, \mathbf{0}}^{[331]} M_{\mathbf{k}_1, \mathbf{0}, \mathbf{k}_1}^{[311]} \frac{1}{\Delta} n_B[\mathcal{E}_{1, \mathbf{k}_1}] - \frac{1}{N} \sum_{\mathbf{k}_1 \in \Lambda_0} M_{\mathbf{0}, \mathbf{0}, \mathbf{0}}^{[311]} M_{\mathbf{0}, \mathbf{k}_1, \mathbf{k}_1}^{[331]} \frac{1}{\Delta} n_B[\mathcal{E}_{1, \mathbf{k}_1}] \\ &\quad - \frac{1}{N} \sum_{\mathbf{k}_1 \in \Lambda_0} M_{\mathbf{0}, \mathbf{0}, \mathbf{0}}^{[331]} M_{\mathbf{k}_1, \mathbf{0}, \mathbf{k}_1}^{[412]} \frac{1}{\Delta} n_B[\mathcal{E}_{2, \mathbf{k}_1}] - \frac{1}{N} \sum_{\mathbf{k}_1 \in \Lambda_0} M_{\mathbf{0}, \mathbf{0}, \mathbf{0}}^{[311]} M_{\mathbf{k}_1, \mathbf{0}, \mathbf{k}_1}^{[432]} \frac{1}{\Delta} n_B[\mathcal{E}_{2, \mathbf{k}_1}]. \end{aligned}$$

Here the function  $n_B(x) = (e^{\beta x} - 1)^{-1}$  is the Bose distribution function. We have defined a symmetrized third-order vertex coefficient

$$M_{\mathbf{k}_1, \mathbf{k}_2, \mathbf{k}_3}^{[l_1 l_2 l_3]} = M_{\mathbf{k}_1, \mathbf{k}_2, \mathbf{k}_3}^{(l_1 l_2 l_3)} + M_{\mathbf{k}_1, \mathbf{k}_3, \mathbf{k}_2}^{(l_1 l_3 l_2)} + M_{\mathbf{k}_2, \mathbf{k}_1, \mathbf{k}_3}^{(l_2 l_1 l_3)} + M_{\mathbf{k}_2, \mathbf{k}_3, \mathbf{k}_1}^{(l_2 l_3 l_1)} + M_{\mathbf{k}_3, \mathbf{k}_1, \mathbf{k}_2}^{(l_3 l_1 l_2)} + M_{\mathbf{k}_3, \mathbf{k}_2, \mathbf{k}_1}^{(l_3 l_2 l_1)}. \quad (4.29)$$

Most dominant contributions to the decay of the Higgs mode stem from  $\Sigma_{11}^{(b)}(i\omega_n)$ . The partial function describes the Beliaev damping processes where one Higgs mode with zero momentum collapses into two NG modes with opposite momenta  $\mathbf{k}$  and  $-\mathbf{k}$  with satisfying the on-shell energy-momentum conservation of  $\mathcal{E}_{1, \mathbf{0}} - \mathcal{E}_{2, \mathbf{k}} - \mathcal{E}_{2, -\mathbf{k}}$ . The Beliaev damping of the Higgs mode in the Bose–Hubbard systems has been studied in some literatures through calculations of its damping rate for  $n_0 \gg 1$  at zero temperature [26] and at finite temperatures [46].

In our previous study based on the imaginary-time Green’s function theory [46], we have calculated the damping rate  $\Gamma \equiv -\text{Im}\Sigma_{11}(i\omega_n)|_{i\omega_n \rightarrow \omega + i\epsilon}$  only at  $\omega = \mathcal{E}_{1, \mathbf{0}} = \Delta$  in order to obtain a qualitative measure of the stability of the Higgs mode. Our analysis of the present paper generalizes it such that the real and imaginary parts of the self-energy functions are taken into account at

$$\begin{aligned}
\mathcal{F}_{1,0}(i\omega_n) = & \left. \begin{array}{c} \text{Diagram 1} + \text{Diagram 2} + \text{Diagram 3} \\ \text{Diagram 4} + \text{Diagram 5} + \text{Diagram 6} \\ \text{Diagram 7} + \text{Diagram 8} \\ \text{Diagram 9} + \text{Diagram 10} + \text{Diagram 11} + \text{Diagram 12} \end{array} \right\} \mathcal{G}_{1,0}(i\omega_n) \Sigma_{02}^{(a)} \mathcal{G}_{1,0}(-i\omega_n) \\
& \left. \begin{array}{c} \text{Diagram 13} + \text{Diagram 14} + \text{Diagram 15} \\ \text{Diagram 16} + \text{Diagram 17} + \text{Diagram 18} \\ \text{Diagram 19} + \text{Diagram 20} \end{array} \right\} \mathcal{G}_{1,0}(i\omega_n) \Sigma_{02}^{(b)} \mathcal{G}_{1,0}(-i\omega_n) \\
& \left. \begin{array}{c} \text{Diagram 21} + \text{Diagram 22} \\ \text{Diagram 23} + \text{Diagram 24} \end{array} \right\} \mathcal{G}_{1,0}(i\omega_n) \Sigma_{02}^{(c)} \mathcal{G}_{1,0}(-i\omega_n) \\
& \left. \begin{array}{c} \text{Diagram 25} + \text{Diagram 26} + \text{Diagram 27} + \text{Diagram 28} \end{array} \right\} \mathcal{G}_{1,0}(i\omega_n) \Sigma_{02}^{(d)} \mathcal{G}_{1,0}(-i\omega_n)
\end{aligned}$$

Figure 4.3: Leading one-loop order contributions to the anomalous Green's function  $\mathcal{F}_{1,0}(i\omega_n)$ . The variables  $\mathbf{k}_1$  and  $i\omega_{n_1}$  added near the internal line implies the internal summation over the possible momentum and Matsubara frequency. The self-energy function of each diagram is obtained by picking off its two external lines. The diagrams in each column form an individual group labeled by  $\Sigma_{02}^{(a)}(i\omega_n)$ ,  $\Sigma_{02}^{(b)}(i\omega_n)$ ,  $\Sigma_{02}^{(c)}(i\omega_n)$ , or  $\Sigma_{02}^{(d)}(i\omega_n)$ .

general frequencies. In particular, the real part is important because it characterizes a renormalization effect of the mean-field Higgs gap, which stems from interactions between the collective excitations.

The diagrams in Fig. 4.2 include processes with an odd number of NG modes. Such a contribution vanishes for a large filling rate  $n_0 \gg 1$  due to the explicit particle-hole symmetry of the effective model  $\mathcal{H}_{\text{eff}}^{n_0 \gg 1}$ . In particular, the contribution of  $\Sigma_{11}^{(c)}$  can emerge only at  $n_0 \sim 1$  and provides purely thermal effects on the damping properties of the Higgs mode. This process can be regarded as a Landau-type damping of the Higgs mode with absorbing one NG mode from a *thermal cloud* and emitting one Higgs mode. In Ref. [46], it has been reported that the NG mode with a non-zero momentum can exhibit a similar Landau damping into a single Higgs mode at finite temperatures via interactions with the NG modes in a thermal cloud. For basic explanations of the Landau damping of collective excitations, see, e.g., Ref. [68].

We next calculate the anomalous self-energy function  $\Sigma_{02}(i\omega_n)$ . In Fig. 4.3, we depict the lowest order corrections to  $\mathcal{F}_{1,0}(i\omega_n)$  by using the Feynman diagrams. The contributions to the anomalous self-energy function  $\Sigma_{02}(i\omega_n)$  are also categorized into four groups as in the case of  $\Sigma_{11}(i\omega_n)$ ;  $\Sigma_{02}(i\omega_n) = \Sigma_{02}^{(a)}(i\omega_n) + \Sigma_{02}^{(b)}(i\omega_n) + \Sigma_{02}^{(c)}(i\omega_n) + \Sigma_{02}^{(d)}(i\omega_n)$ . Each diagram in  $\Sigma_{02}(i\omega_n)$  has the same structure as the corresponding diagram in  $\Sigma_{11}(i\omega_n)$  except for the interaction vertex on the righthand side at which the right external line connects with two internal lines. The analytic

expressions of the anomalous self-energy function are given as follows:

$$\begin{aligned}
\Sigma_{02}^{(a)}(i\omega_n) &= -\frac{1}{2N} \sum_{\mathbf{k}_1 \in \Lambda_0} M_{\mathbf{0},\mathbf{k}_1,-\mathbf{k}_1}^{[333]} M_{\mathbf{0},\mathbf{k}_1,-\mathbf{k}_1}^{[311]} \frac{1 + 2n_B[\mathcal{E}_{1,\mathbf{k}_1}]}{i\omega_n + 2\mathcal{E}_{1,\mathbf{k}_1}} - \frac{1}{2N} \sum_{\mathbf{k}_1 \in \Lambda_0} M_{\mathbf{0},\mathbf{k}_1,-\mathbf{k}_1}^{[344]} M_{\mathbf{0},\mathbf{k}_1,-\mathbf{k}_1}^{[322]} \frac{1 + 2n_B[\mathcal{E}_{2,\mathbf{k}_1}]}{i\omega_n + 2\mathcal{E}_{2,\mathbf{k}_1}} \\
&\quad - \frac{1}{N} \sum_{\mathbf{k}_1 \in \Lambda_0} M_{\mathbf{0},\mathbf{k}_1,-\mathbf{k}_1}^{[334]} M_{\mathbf{0},\mathbf{k}_1,-\mathbf{k}_1}^{[312]} \frac{1 + n_B[\mathcal{E}_{1,\mathbf{k}_1}] + n_B[\mathcal{E}_{2,\mathbf{k}_1}]}{i\omega_n + \mathcal{E}_{1,\mathbf{k}_1} + \mathcal{E}_{2,\mathbf{k}_1}}, \\
\Sigma_{02}^{(b)}(i\omega_n) &= \frac{1}{2N} \sum_{\mathbf{k}_1 \in \Lambda_0} M_{\mathbf{0},\mathbf{k}_1,-\mathbf{k}_1}^{[311]} M_{\mathbf{0},\mathbf{k}_1,-\mathbf{k}_1}^{[333]} \frac{1 + 2n_B[\mathcal{E}_{1,\mathbf{k}_1}]}{i\omega_n - 2\mathcal{E}_{1,\mathbf{k}_1}} + \frac{1}{2N} \sum_{\mathbf{k}_1 \in \Lambda_0} M_{\mathbf{0},\mathbf{k}_1,-\mathbf{k}_1}^{[322]} M_{\mathbf{0},\mathbf{k}_1,-\mathbf{k}_1}^{[344]} \frac{1 + 2n_B[\mathcal{E}_{2,\mathbf{k}_1}]}{i\omega_n - 2\mathcal{E}_{2,\mathbf{k}_1}} \\
&\quad + \frac{1}{N} \sum_{\mathbf{k}_1 \in \Lambda_0} M_{\mathbf{0},\mathbf{k}_1,-\mathbf{k}_1}^{[312]} M_{\mathbf{0},\mathbf{k}_1,-\mathbf{k}_1}^{[334]} \frac{1 + n_B[\mathcal{E}_{1,\mathbf{k}_1}] + n_B[\mathcal{E}_{2,\mathbf{k}_1}]}{i\omega_n - \mathcal{E}_{1,\mathbf{k}_1} - \mathcal{E}_{2,\mathbf{k}_1}}, \\
\Sigma_{02}^{(c)}(i\omega_n) &= -\frac{1}{N} \sum_{\mathbf{k}_1 \in \Lambda_0} M_{\mathbf{0},\mathbf{k}_1,\mathbf{k}_1}^{[332]} M_{\mathbf{0},\mathbf{k}_1,\mathbf{k}_1}^{[341]} \frac{n_B[\mathcal{E}_{1,\mathbf{k}_1}] - n_B[\mathcal{E}_{2,\mathbf{k}_1}]}{i\omega_n + \mathcal{E}_{2,\mathbf{k}_1} - \mathcal{E}_{1,\mathbf{k}_1}} - \frac{1}{N} \sum_{\mathbf{k}_1 \in \Lambda_0} M_{\mathbf{0},\mathbf{k}_1,\mathbf{k}_1}^{[341]} M_{\mathbf{0},\mathbf{k}_1,\mathbf{k}_1}^{[332]} \frac{n_B[\mathcal{E}_{2,\mathbf{k}_1}] - n_B[\mathcal{E}_{1,\mathbf{k}_1}]}{i\omega_n + \mathcal{E}_{1,\mathbf{k}_1} - \mathcal{E}_{2,\mathbf{k}_1}}, \\
\Sigma_{02}^{(d)}(i\omega_n) &= -\frac{1}{N} \sum_{\mathbf{k}_1 \in \Lambda_0} M_{\mathbf{0},\mathbf{0},\mathbf{0}}^{[333]} M_{\mathbf{k}_1,\mathbf{k}_1,\mathbf{0}}^{[311]} \frac{1}{\Delta} n_B[\mathcal{E}_{1,\mathbf{k}_1}] - \frac{1}{N} \sum_{\mathbf{k}_1 \in \Lambda_0} M_{\mathbf{0},\mathbf{0},\mathbf{0}}^{[331]} M_{\mathbf{0},\mathbf{k}_1,\mathbf{k}_1}^{[331]} \frac{1}{\Delta} n_B[\mathcal{E}_{1,\mathbf{k}_1}] \\
&\quad - \frac{1}{N} \sum_{\mathbf{k}_1 \in \Lambda_0} M_{\mathbf{0},\mathbf{0},\mathbf{0}}^{[333]} M_{\mathbf{k}_1,\mathbf{k}_1,\mathbf{0}}^{[421]} \frac{1}{\Delta} n_B[\mathcal{E}_{2,\mathbf{k}_1}] - \frac{1}{N} \sum_{\mathbf{k}_1 \in \Lambda_0} M_{\mathbf{0},\mathbf{0},\mathbf{0}}^{[331]} M_{\mathbf{k}_1,\mathbf{k}_1,\mathbf{0}}^{[423]} \frac{1}{\Delta} n_B[\mathcal{E}_{2,\mathbf{k}_1}].
\end{aligned}$$

Here we should mention how to evaluate the momentum summations appearing in the self-energy functions. In our analysis, we have numerically computed the retarded self-energy functions such as  $\Sigma_{11}^R(\omega) = \Sigma_{11}(i\omega_n)|_{i\omega_n \rightarrow \omega + i\epsilon}$  for a fixed frequency after replacing the summations by the corresponding integral, i.e.,  $\sum_{\mathbf{k}_1 \in \Lambda_0} \rightarrow \int_{-\pi}^{\pi} \int_{-\pi}^{\pi} \int_{-\pi}^{\pi} dk_x dk_y dk_z / (2\pi)^3$ . From the self-energy functions obtained numerically, we can construct the dynamical susceptibilities  $\chi_{KK}(\omega)$  and  $\chi_{OO}(\omega)$  according to the formulae (4.27) and (4.28).

## 4.4 Results

Using the formulations explained in the previous sections, we are able to obtain the dynamical susceptibilities. In this section, we compute the imaginary part of the susceptibility as a function of frequency  $\omega$  and discuss the stability of the Higgs mode in 3D optical lattices.

### 4.4.1 Response functions in the uniform system

We analyze the response functions (dynamical susceptibilities) with no trapping potential in order to discuss the broadening of the resonance peak solely due to quantum and thermal fluctuations. In Fig. 4.4, we show  $\text{Im}[\chi_{KK}(\omega)]$  at the unit filling rate and at zero temperature. Notice that the two response functions  $\chi_{KK}(\omega)$  and  $\chi_{OO}(\omega)$  are equal as mentioned in Sec. 4.3. In Fig. 4.4, we see a sufficiently sharp resonance peak corresponding to the Higgs mode, which forms a Lorentzian-like curve. The center of the peak defines a renormalized Higgs gap and the width provides a

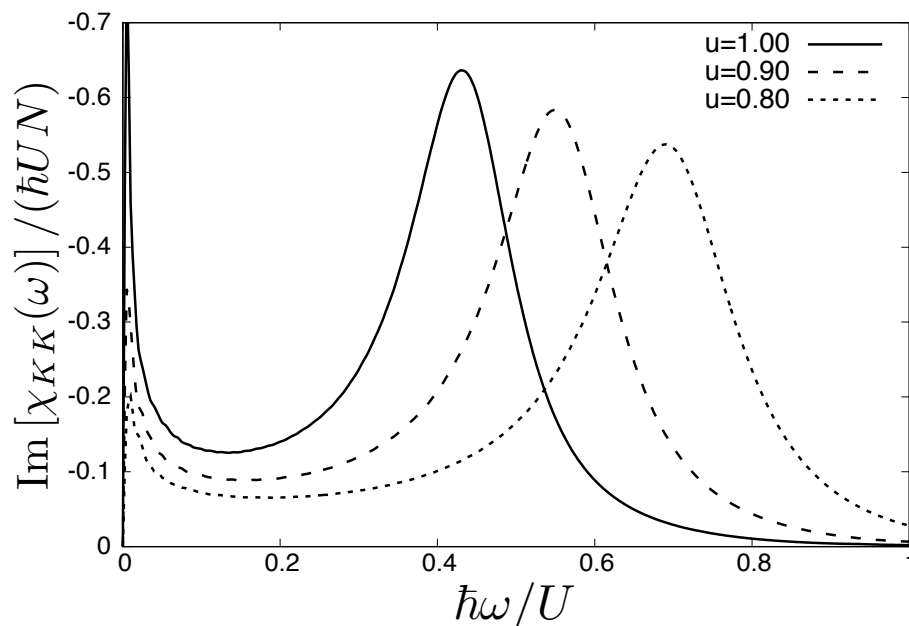


Figure 4.4: Susceptibility at the unit filling rate  $n_0 = 1$  and at zero temperature. The position of the resonance peak increases away from the critical point  $u_c \approx 1.457$ .

damping rate of the mode. The existence of the sharp resonance peak implies that the Higgs mode is stable in the 3D system within the lowest order of the quantum fluctuation. In addition, the position of the peak shifts to the high- $\omega$  side as  $u$  leaves from the critical point  $u = u_c$ . Table 4.1 shows each value of the renormalized Higgs gap  $\Delta_*$  scaled by the corresponding Mott gap  $\Delta_{\text{MI}}$ , which has a same relative distance from the critical point,  $\bar{u}_{\text{rel}} = |u - u_c|/u_c$ , as that of the Higgs gap. As the energy scale, we used the mean-field Mott gap  $\Delta_{\text{MI}} = \sqrt{U^2 - 2JzU(2n_0 + 1) + (Jz)^2}$ , which is derived in Ref. [92].

We also see the similar behavior at a large filling rate  $n_0 \gg 1$ . In Fig. 4.5, we show  $\text{Im}[\chi_{KK}(\omega)]$  at a large filling rate and at zero temperature. The peak width approximately coincides with the

Table 4.1: Values of the renormalized Higgs gap  $\Delta_*$  scaled by the Mott gap  $\Delta_{\text{MI}}$ .  $\Delta_*$  and  $\Delta_{\text{MI}}$  locate at a same relative distance  $\bar{u}_{\text{rel}}$  from the critical point  $u_c \approx 1.457$ .  $u_o$  and  $u_d$  are the corresponding values of  $u$  at a given  $\bar{u}_{\text{rel}} = |u - u_c|/u_c$  in the ordered side and disordered side, respectively.

| $\Delta_*/\Delta_{\text{MI}}$ | $\Delta/\Delta_{\text{MI}}$ | $\bar{u}_{\text{rel}}$ | $u_o$ | $u_d$ |
|-------------------------------|-----------------------------|------------------------|-------|-------|
| 0.890                         | 1.081                       | 0.314                  | 1.000 | 1.914 |
| 1.057                         | 1.206                       | 0.382                  | 0.900 | 2.014 |
| 1.251                         | 1.359                       | 0.451                  | 0.800 | 2.114 |

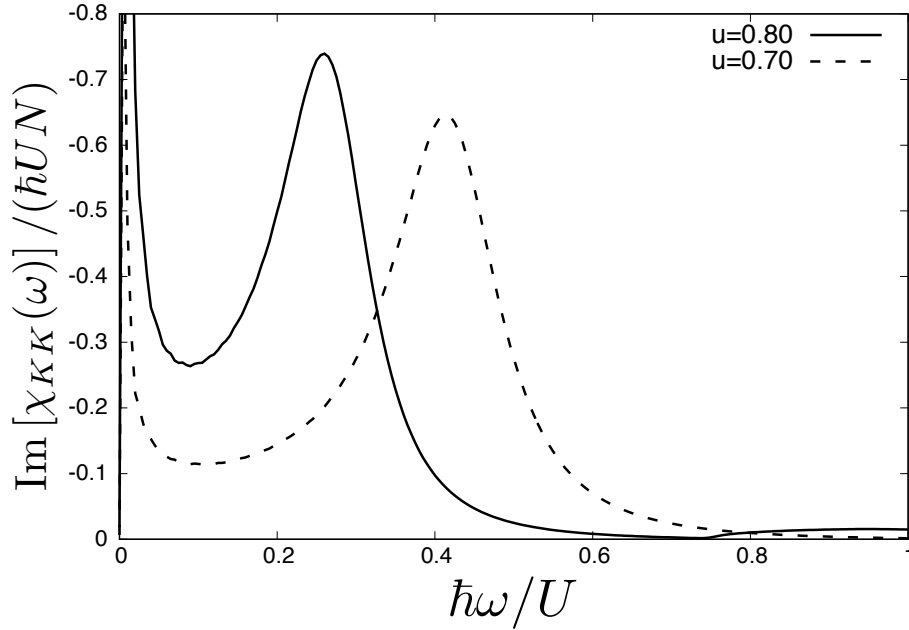


Figure 4.5: Susceptibility at a large filling rate  $n_0 \gg 1$  and at zero temperature. The peak position corresponding to the Higgs mode gap increases away from the critical point  $u_c = 1$ .

damping rate of the Higgs mode evaluated in three dimensions and at a large filling rate [26]. It should be noted that we see another peak near  $\omega = 0$ . Such an additional peak near  $\omega = 0$  also appears in Fig. 4.4. The additional peak can be interpreted as an artifact of our perturbative method. In fact, the real parts of the self-energy functions become as large as the mean-field Higgs gap near  $\omega = 0$ . This means that the perturbative corrections to the Higgs gap are no longer small compared with the zeroth-order gap itself, i.e., the perturbative approximation breaks down near  $\omega = 0$ . Nevertheless, the perturbative corrections are sufficiently small compared to the Higgs gap  $\Delta$  around  $\omega = \Delta_*$ , meaning that our perturbative approach is valid there. The emergence of this additional peak is related to the logarithmic infrared divergence of the self-energy functions of the  $(3 + 1)$ -dimensional relativistic  $O(N)$  scalar model [166]. Notice that in contrast to the infrared divergence of the self-energy function, our naive perturbation approach fails to describe the logarithmic corrections that appear as a result of renormalization of the marginal terms [167], which is ignored in our analysis.

Next, we consider finite-temperature effects on the response functions. In Fig. 4.6, we show the temperature dependence of the susceptibility at  $u = 1$ . The results show that the thermal fluctuation only makes the peak width slightly broader, so that the resonance peak is quite robust against the thermal fluctuations up to  $T = 2J$ . Considering that the typical temperature in real experiments is of order  $J$ , we conclude that the Higgs resonance peak survives even at typical

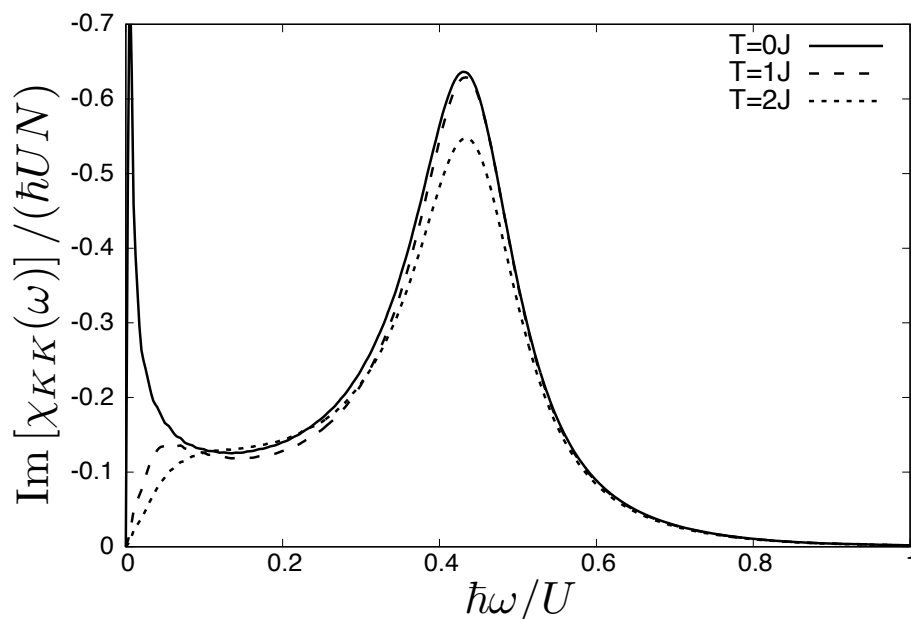


Figure 4.6: Susceptibility at the unit filling rate  $n_0 = 1$  and at typical temperatures. We have chosen the specific parameter  $u = 1$  ( $zJ/U = 0.25$ ).

temperatures and at the unit filling rate. Our result is in contrast to the case of the 2D Bose–Hubbard model computed by the quantum Monte-Carlo simulations [43]. The result of Ref. [43] implies that the resonance of the Higgs mode becomes rather broad due to the quantum and thermal fluctuations even when the system is uniform.

It is worth noting that the damping rate of the zero-momentum Higgs mode at a large filling rate, which is computed in the similar way of our approaches used in this paper, also shows that the Higgs mode is sufficiently stable at typical temperatures of order  $J$  [46]. Our result presented in Fig. 4.6 generalizes the result obtained in the virtual large-filling case [46] into a more realistic case with unit filling rate corresponding to actual experiments.

#### 4.4.2 Effects of a trapping potential

We include the trapping-potential effects within the local density approximation. As a specific shape of the potential, we assume a parabolic and isotropic potential

$$V_{\text{trap}}(r) = \frac{m\omega_0^2}{2}r^2, \quad (4.30)$$

where  $m$  is the atomic mass and  $\omega_0$  is the frequency of the potential. According to the conventional local density approximation (LDA) [121], the effect of the inhomogeneity is described by the

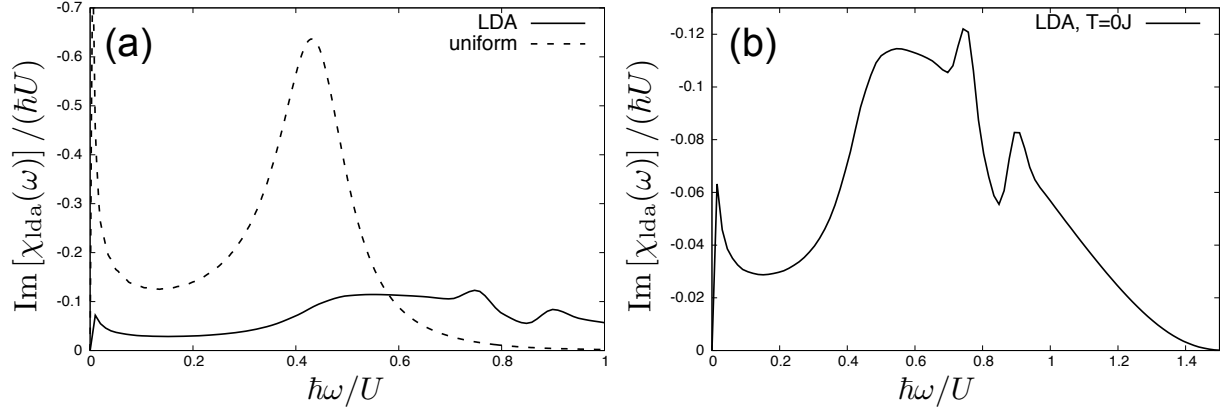


Figure 4.7: (a) Dynamical susceptibility of the trapped system (the solid line) versus the one in the homogeneous system (the dashed line) at  $T = 0$  and  $u = 1$ . At the center of the trap, the density of the system is tuned to unity, i.e.,  $n_0 = 1$ . (b) Magnifying the dynamical susceptibility of the trapped system at zero temperature. In order to obtain a smooth line from LDA data, we used the spline interpolation.

general formula

$$\chi_{\text{lda}}(\omega) = 4\pi \int_0^R dr r^2 \bar{n}'[\mu(r)] \chi_{\text{unif}}(\omega, \mu(r)), \quad (4.31)$$

where  $\chi_{\text{unif}}(\omega, \mu)$  is the bulk susceptibility [Eqs. (4.2) or (4.4) divided by the factor  $N$ ] at the fixed chemical potential  $\mu$  and  $\mu(r) = \mu_{n_0} - V_{\text{trap}}(r)$  is the local chemical potential.  $\bar{n}'[\mu]$  is the normalized density defined by

$$\bar{n}'[\mu(r)] = \frac{\bar{n}[\mu(r)]}{4\pi \int_0^R dr r^2 \bar{n}[\mu(r)]}. \quad (4.32)$$

$R$  denotes the radius of the spherical region, in which atoms are perturbed by the temporal modulation of  $J$  or  $U$ . When the modulation perturbs the entire system,  $R$  is equal to the Thomas–Fermi radius  $R_{\text{TF}}$ , at which the density vanishes. We assume that at the trap center the density  $\bar{n}[\mu_{n_0}]$  is tuned to  $n_0 = 1$ .

#### 4.4.3 Response functions at $R = R_{\text{TF}}$

We analyze the response function to the modulation applied globally to the entire system. In this case the radial integral in Eq. (4.31) is taken up to the Thomas–Fermi radius from the spatial center of the trapping potential:  $R = R_{\text{TF}}$ .

In Fig. 4.7 (a), we show  $\text{Im}[\chi_{\text{lda}}(\omega)]$  together with the one in the absence of the potential (4.30). We assume that  $T = 0$  and  $u = 1$ , at which a sharp resonance peak survives when the

system is homogeneous. In Fig. 4.7 (b), we plot the same LDA susceptibility in a magnified scale in order to see its detailed structure. There we see that the resonance peak, which would be rather sharp without the trapping potential, is significantly broadened due to the inhomogeneity effect so that the peak width is as large as the Higgs gap  $\Delta$ . In this sense, one can no longer regard the response as a well-defined resonance peak.

The broadening of the resonance peak can be attributed to the following reason. When we apply the modulation globally to the entire system, all the subsystems corresponding to  $\bar{n} \in [0, 1]$  contribute to the resulting response. Specifically, the gap at  $\bar{n} < 1$  is larger than that at  $\bar{n} = 1$  and the high-energy contributions far from the trapping center obscure the well-defined Higgs resonance.

In Fig. 4.7 (b), we also find a fine structure of the response in the region of  $0.7U < \omega < 1.0U$ . This structure means that the response of the bulk gapful mode at a certain value of  $\mu$ , which gives  $\Delta \simeq 0.75U$  ( $0.85U$ ), is locally strong (weak). It is interesting to examine in future experiments whether or not the emergence of the fine structure is an artifact of LDA.

While the resonance peak structure in the response is smeared out, a characteristic feature of the Higgs mode in the bulk is still visible in the susceptibility of the trapped system. Specifically, the onset frequency of the response is almost equal to the bulk Higgs gap  $\Delta$  at  $\bar{n} = 1$ . This property has been found also in 2D [43] and indeed utilized to measure  $\Delta$  in experiment [19].

#### 4.4.4 Responses around the trapping center

We analyze the response to a partial modulation, which acts only on atoms inside the spherical region with  $R < R_{\text{TF}}$  around the trap center. In this way, we eliminate the contributions from the low-density region that broaden the resonance peak and expect to see a sharp resonance peak as long as  $R$  is sufficiently small. A similar analysis at 2D has been presented in Ref. [44]. In what follows, we set  $u = 1$ .

We define the radius for the partial modulation as  $R_{\text{mod}}$ . In the unit of the Thomas-Fermi radius  $R_{\text{TF}}$ , the modulation radius  $R_{\text{mod}}$  reads

$$\frac{R_{\text{mod}}}{R_{\text{TF}}} = \sqrt{\frac{\mu_{n_0} - \mu_{\text{mod}}}{\mu_{n_0} - \mu_{\text{TF}}}}, \quad (4.33)$$

where  $\mu_{\text{mod}} = \mu(R_{\text{mod}})$  and  $\mu_{\text{TF}} = \mu(R_{\text{TF}})$ . In particular, one can easily see that  $\mu_{\text{TF}} = -0.75U$  for  $u = 1$ . The calculation of the LDA is performed just by making  $R = R_{\text{mod}}$  in Eq. (4.31).

In Fig. 4.8, we show  $\text{Im}[\chi_{\text{lda}}(\omega)]$  at zero temperature for different values of  $R_{\text{mod}}$ . When  $R_{\text{mod}}/R_{\text{TF}} = 0.49$ , the modulation is added to a subregion of  $\bar{n} \geq 0.90$ . In this case, the shape of the resonance peak in the resulting response function is well approximated as a Lorentzian function

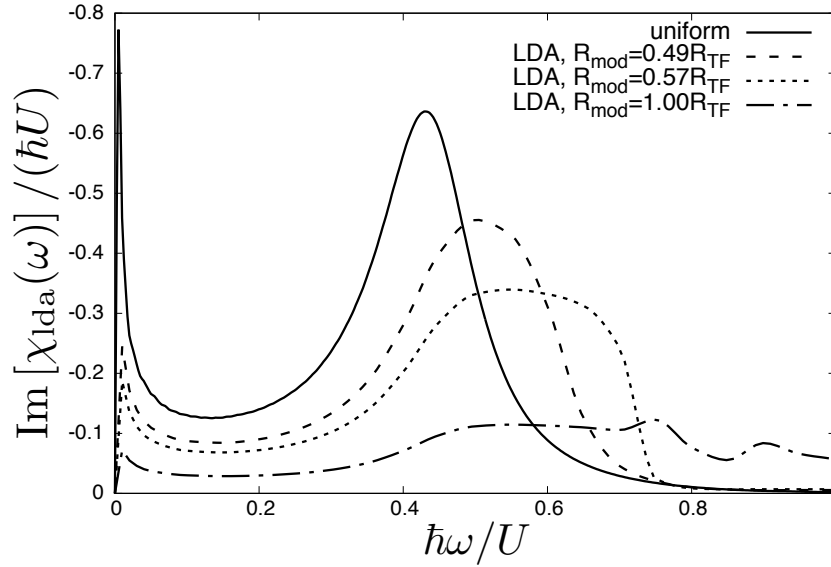


Figure 4.8: Averaged dynamical susceptibilities in the trapped system modulated partially. The dashed, dotted, and dash-dotted lines correspond to  $R_{\text{mod}}/R_{\text{TF}} = 0.49, 0.57, 1.00$ , respectively. The susceptibility approaches the uniform result (solid line) in the limit of  $R_{\text{mod}} \rightarrow 0$ . Here  $u = 1$  ( $zJ/U = 0.25$ ) and  $T/J = 0$ . The filling factor at the trapping center is tuned to unity, i.e.,  $n_0 = 1$ .

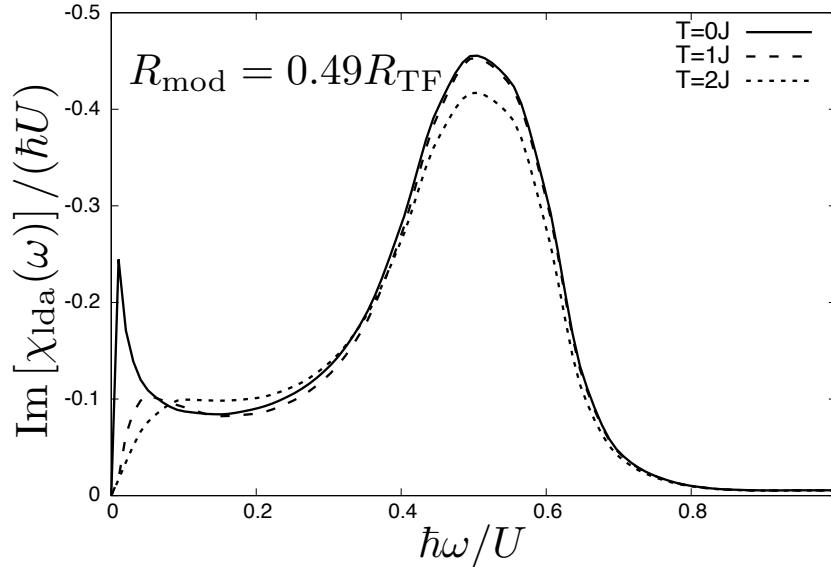


Figure 4.9: Finite temperature effects on the susceptibilities of the trapped system at  $u = 1$  and  $R_{\text{mod}}/R_{\text{TF}} = 0.49$ . The solid, dashed, and dotted lines represent  $T/J = 0, 1, 2$ , respectively. At the center of the trap, the density of the system is tuned to unity, i.e.,  $n_0 = 1$ .

and the peak width is clearly smaller than the peak position. Thus, the response exhibits a sharp resonance peak. We also find that the peak position is slightly shifted to the high-energy side due to the contribution from the low-density region.

When  $R_{\text{mod}}/R_{\text{TF}}$  is increased, the response becomes broader to approach the result at  $R_{\text{mod}} = R_{\text{TF}}$  (See the dash-dotted line in Fig. 4.8). When  $R_{\text{mod}}/R_{\text{TF}} = 0.57$ , at which a subregion of  $\bar{n}(r) \geq 0.85$  is modulated, the response is significantly broader than that of  $R_{\text{mod}}/R_{\text{TF}} = 0.49$  and the shape of the response function noticeably deviates from a Lorentzian function. Thus, our results indicate that the condition that  $R_{\text{mod}} < 0.5R_{\text{TF}}$  is required for a sharp resonance peak to be observed.

For the case of  $R_{\text{mod}}/R_{\text{TF}} = 0.49$ , let us consider finite-temperature effects on the LDA susceptibility of the partial modulation. Figure 4.9 shows the results at different temperatures. Our results reveal that the resonance peak is robust against thermal fluctuations at typical experimental temperatures of order  $J$ . The robustness of the response is not related with the specific choice of  $R_{\text{mod}}$  because the similar feature can be found in the uniform cases. According to the results in Fig. 4.9, it is expected to be able to detect the well-defined Higgs-mode resonance in typical three-dimensional experiments with a parabolic potential. The detection procedure requires a partial modulation of  $J$  or  $U$  over a radius  $R_{\text{mod}} \leq R_{\text{TF}}$ , and it is, in principle, possible in experiments. We emphasize that the temperature dependence in 3D systems is distinct from that in 2D systems [44]. In 2D systems, the response function significantly depends on the temperature so that the Higgs peak is smeared out due to thermal fluctuations when  $T > J$  even for partial modulations.

## 4.5 Summary of this chapter

In conclusion of this chapter, we analyzed the effects of quantum and thermal fluctuations, and spatial inhomogeneity due to a trapping potential on the response functions of the 3D Bose–Hubbard model both for the hopping strength and onsite-interaction strength modulations, respectively. At the unit filling rate and in the absence of the trapping potential, our results showed that the Higgs mode can exist as a sharp resonance peak in the dynamical susceptibilities at typical temperatures. We included the effect of a trapping potential within the local density approximation and indicated that the resonance peak is significantly broadened due to the trapping potential when the modulations are applied globally to the entire system. In order to extract a sharp resonance peak from the smeared response, we discussed partial modulations around the trap center. The results with a modulation radius  $R_{\text{mod}} < 0.5R_{\text{TF}}$  showed that a well-defined resonance peak of the Higgs mode can survive at typical temperatures.

# Chapter 5

## Semiclassical quench dynamics of Bose gases in optical lattices

In this chapter, we apply the truncated-Wigner approximation (TWA) to some problems of quantum-quench dynamics in optical lattices. In Sec. 5.1, we briefly present the semiclassical representation of dynamics of the Bose–Hubbard model. In Sec. 5.2, we simulate redistribution dynamics of the kinetic and interaction energies after a sudden quench in the three-dimensional (3D) Bose–Hubbard model starting from a strongly-correlated Mott-insulator state. There, we discuss direct comparison between the TWA and experimental results and examine the accuracy and power of our semiclassical technique in the 3D experimental system. In Sec. 5.3, generalizing the technique used in Sec. 5.2, we analyze non-local spreading of an equal-time correlation function in the two-dimensional (2D) Bose–Hubbard model. Especially, we focus on how the correlation spreading depends on the initial quantum state. In Sec. 5.4, we conclude and summarize this chapter.

### 5.1 Semiclassical dynamics of the Bose–Hubbard model

In this chapter, we discuss far-from-equilibrium dynamics of the Bose–Hubbard model, which describes ultracold Bose gases tightly trapped by an optical-lattice potential:

$$\hat{H} = -J \sum_{\langle j,k \rangle} (\hat{a}_j^\dagger \hat{a}_k + \text{h.c.}) + \frac{U}{2} \sum_j \hat{a}_j^\dagger \hat{a}_j^\dagger \hat{a}_j \hat{a}_j. \quad (5.1)$$

Once we admit the results derived in Chap. 3, we immediately obtain the TWA formula for the quantum average of an arbitrary operator  $\hat{\Omega}[\hat{a}_i, \hat{a}_i^\dagger]$  with respect to the quantum state at time  $t$ :

$$\langle \hat{\Omega}(t) \rangle \approx \int d\vec{\alpha}_0 d\vec{\alpha}_0^* W_0(\vec{\alpha}_0, \vec{\alpha}_0^*) \Omega_W[\vec{\alpha}_{\text{cl}}(t), \vec{\alpha}_{\text{cl}}^*(t)], \quad (5.2)$$

where  $\vec{\alpha}_{\text{cl}}(t)$  is a solution of the Gross–Pitaevskii equation for an initial classical field  $\vec{\alpha}_0$ . The initial classical fields distribute over the phase space according to the Wigner function of the

initial quantum state  $W_0(\vec{\alpha}, \vec{\alpha}^*)$ . Here we note that the classical field scales with a square root of the filling factor  $\bar{n} = N_{\text{tot}}/M$  ( $N_{\text{tot}}$  is the total number of atoms). Hence, the semiclassical expansion of the TWA is characterized by the inverse of  $\bar{n}$  [49].

As already mentioned in Chap. 3, the semiclassical approximation used in Eq. (5.2) yields a quantum-fluctuation correction to a mean-field solution of dynamics within the lowest order [129]. In a weakly fluctuating regime, where an interaction parameter  $\lambda \equiv U\bar{n}/J$  is far from the quantum phase transition point  $\lambda_c$ , i.e.,  $\lambda \ll \lambda_c$ , the TWA quantitatively describes time evolution of the system until the time  $t$  approaches a characteristic timescale  $t_c$  [49–51]. When  $\lambda$  is close to the critical value  $\lambda_c$ , which corresponds to the quantum phase transition point, the semiclassical treatment breaks down at short time due to the strong fluctuations. Since  $\lambda_c \propto \bar{n}^2$ , larger  $\bar{n}$  and/or smaller  $U/J$  means larger  $t_c$  [50, 51]. Especially at  $U/J = 0$  or  $\bar{n} = \infty$ , the semiclassical approximation becomes exact.

In typical experiments including the 3D experiment [35, 36], which we discuss in Sec. 5.2,  $\bar{n}$  is tuned to unity and  $\lambda$  is  $O(1)$ . If one computes time evolution of the 1D Bose–Hubbard model with  $\bar{n} = 1$  and  $\lambda \sim 1$  within the TWA, it fails in much shorter time than  $O(\hbar/J)$  because of rather small  $\lambda_c (= 3.367)$  [93]. In contrast, for the 3D case with the same parameters, it is expected that the TWA is able to simulate the dynamics up to  $t \sim \hbar/J$ , because  $\lambda$  of  $O(1)$  is sufficiently far from  $\lambda_c = 29.34$  [81]. As we will see in Sec. 5.2, the TWA can reproduce characteristic early-time dynamics observed in the experiment [36] until  $t \sim \hbar/J$ .

## 5.2 Redistribution of the kinetic and interaction energies

In this section, we apply the formalism of TWA for simulating the non-equilibrium dynamics of Bose gases in the cubic optical lattice observed in the experiment [35, 36]. Using the TWA for the 3D Bose–Hubbard model, we numerically compute the time evolution of the kinetic and interaction energies after a sudden quench from a singly-occupied Mott-insulator state into a weakly interacting regime.

### 5.2.1 Experimental setup

In the experiment of Refs. [35, 36], a gas of  $^{174}\text{Yb}$  atoms (bosons) is confined in a cubic optical lattice with lattice spacing  $d_{\text{lat}} = 266$  nm. The typical energy scale of this system is given by the recoil energy  $E_R/\hbar = 2\pi \times 4021.18$  Hz. The experimental protocol for studying quantum quench dynamics is summarized as follows:

(i) The optical lattice depth  $V_0$  is slowly ramped up to  $V_0 = 15E_R$ , at which  $U/J = 99.4$ , in order to prepare a singly-occupied Mott insulator.

(ii) The lattice depth is abruptly ramped down from  $V_0 = 15E_R$  to  $V_0 = 5E_R$  in the ramp-down time  $t_f = 0.1$  ms in order to prepare a state far from equilibrium. At the final depth, implying that  $U/J = 3.41$ , the ground state is deeply in the superfluid regime [81].

(iii) After the ramp-down process, the time evolution of ensemble averages of the kinetic and onsite interaction energies, i.e.,

$$\hat{K} = -J \sum_{\langle j,k \rangle} (\hat{a}_j^\dagger \hat{a}_k + \text{h.c.}), \quad \hat{O} = \frac{U}{2} \sum_j \hat{a}_j^\dagger \hat{a}_j^\dagger \hat{a}_j \hat{a}_j, \quad (5.3)$$

is measured. The kinetic and interaction energies are extracted from the time-of-flight imaging and the high-resolution atom-number-projection spectroscopy, respectively [168].

It is worth noting that although there is a parabolic trapping potential in the real experiment [36], we neglect it in our TWA calculations for the following reason. At the initial Mott-insulator state, the particle density of the system is almost uniform in space so that the initial quantum state is well approximated as a direct-product wave function, which is spatially uniform and composed of a local Fock state (see Sec. 5.2.2). The trapping potential gives no noticeable effect on the quench dynamics within the time window  $t \lesssim \hbar/J$ , in which the experiment was performed, because the trap frequency is much smaller than  $J/\hbar$ .

### 5.2.2 Application of TWA to the quench experiment

Within the framework of TWA, the time-dependent quantum average of the kinetic and interaction energies is approximated to a semiclassical form:

$$\begin{aligned} \langle \hat{K}(t) \rangle &\approx \int d\vec{\alpha}_0 d\vec{\alpha}_0^* W(\vec{\alpha}_0, \vec{\alpha}_0^*) K_W[\vec{\alpha}_{\text{cl}}(t), \vec{\alpha}_{\text{cl}}^*(t)], \\ \langle \hat{O}(t) \rangle &\approx \int d\vec{\alpha}_0 d\vec{\alpha}_0^* W(\vec{\alpha}_0, \vec{\alpha}_0^*) O_W[\vec{\alpha}_{\text{cl}}(t), \vec{\alpha}_{\text{cl}}^*(t)], \end{aligned}$$

where  $K_W(\vec{\alpha}, \vec{\alpha}^*)$  and  $O_W(\vec{\alpha}, \vec{\alpha}^*)$  are the Weyl symbols of  $\hat{K}$  and  $\hat{O}$ , respectively. The classical time evolution is generated by the Weyl symbol of the Bose–Hubbard Hamiltonian, which is equal to the sum of  $K_W(\vec{\alpha}, \vec{\alpha}^*)$  and  $O_W(\vec{\alpha}, \vec{\alpha}^*)$ :

$$H_W(\vec{\alpha}, \vec{\alpha}^*) = K_W(\vec{\alpha}, \vec{\alpha}^*) + O_W(\vec{\alpha}, \vec{\alpha}^*), \quad (5.4)$$

$$K_W(\vec{\alpha}, \vec{\alpha}^*) = -J \sum_{\langle j,k \rangle} [\alpha_j^* \alpha_k + \text{c.c.}], \quad (5.5)$$

$$O_W(\vec{\alpha}, \vec{\alpha}^*) = \frac{U}{2} \sum_j \left[ |\alpha_j|^4 - 2|\alpha_j|^2 + \frac{1}{2} \right]. \quad (5.6)$$

These classical functions can be derived by means of, e.g., the Bopp-operator representation of the bosonic operators  $\hat{a}_j$  and  $\hat{a}_j^\dagger$  as explained in the previous chapter.

The initial state before the quench in the experiment can be represented by a product-state wave function  $|\Psi_{\text{ini}}\rangle = \prod_j |\bar{n}\rangle_j$ , where  $|\bar{n}\rangle_j$  is a local Fock state characterized by  $\hat{n}_j|\bar{n}\rangle_j = \bar{n}|\bar{n}\rangle_j$ . The corresponding Wigner function  $W_{\text{mott}}(\vec{\alpha}, \vec{\alpha}^*)$  is given by a direct product of the local Wigner function of the Fock-state vector  $|\bar{n}\rangle_j$  at each site, which was presented in Chap. 3. Thus, the Wigner function of the initial state reads [48, 51, 169, 170]

$$W_{\text{mott}}(\vec{\alpha}, \vec{\alpha}^*) = \prod_j 2e^{-2|\alpha_j|^2} (-1)^{\bar{n}} L_{\bar{n}}(4|\alpha_j|^2), \quad (5.7)$$

where  $L_n(x) = \sum_{r=0}^n (-1)^r \frac{n!}{(n-r)! (r!)^2} x^r$  is the Laguerre polynomial of order  $n$ . Here we parametrize the classical field as  $\alpha_j = |\alpha_j| e^{i\varphi_j}$ . This Wigner function is not positive definite along a direction of the amplitude degrees of freedom  $|\alpha_j|$ , except for a trivial case  $\bar{n} = 0$ . The phase of the classical field  $\varphi_j$  distributes uniformly in  $[0, 2\pi]$ . The Wigner function has an explicit U(1) symmetry reflecting the restored symmetry inside the Mott-insulator state. In fact, a general phase shift of the phase-space variables,  $\alpha_j \rightarrow \alpha_j e^{i\varphi_j}$ , does not change in the value of the Wigner function.

The negativity of Eq. (5.7) makes it difficult to obtain converged results in numerically evaluating the phase-space integration weighted by the Wigner function. For this reason, in our numerical simulations, we adopt a Gaussian approximation for the exact Wigner function of a Fock state [169, 170]. Repeating the discussions in the previous literatures [169, 170], the Gaussian-Wigner function corresponding to a Fock-state vector  $|\bar{n}\rangle$  has a general form as

$$W_g(n) = \frac{1}{\sqrt{2\pi\sigma^2}} e^{-\frac{1}{2\sigma^2}(n-n_0)^2}, \quad (5.8)$$

where  $n = |\alpha|^2$ . The mean  $n_0$  and covariance  $\sigma$  are free parameters determined from the consistency that the Gaussian function should exactly recover the first and second order local moments of the density, i.e.,  $\langle \hat{n}_j \rangle$  and  $\langle \hat{n}_j^2 \rangle$ . From direct calculations, we find that the optimal choice is  $n_0 = \bar{n} + \frac{1}{2}$  and  $\sigma = \frac{1}{2}$ . It is worth noting that the (rescaled) higher-order moments  $\bar{n}^{-m} \langle \hat{n}_j^m \rangle$  for  $m > 2$  computed by the Gaussian function agree with the exact ones up to  $O(\bar{n}^{-2})$  [170]. While the normalized Gaussian function can give rise to an unphysical negative density, however, it does not affect the phase-space average itself because the probability, which corresponds to the Gaussian tail, is sufficiently small even at  $\bar{n} = 1$ . In addition, a similar Gaussian approximation is often used in literatures of TWA studies [51, 119, 134, 139, 148, 169, 170] and manifests its validity in the semiclassical descriptions of short time dynamics.

Now we summarize what should be analyzed in the TWA: We solve time evolutions of a time-dependent Bose–Hubbard model  $\hat{H}[\lambda(t)]$  by using the TWA. At  $t = 0$ , the Hamiltonian has  $\lambda = \lambda_i = 99.4$  corresponding to  $V_0 = 15E_R$ . In the ramp-down process,  $\lambda(t)$  decreases with  $V_0(t)$ , which declines linearly. Recall that the duration of the ramp-down process is  $t_f = 0.1$  ms in

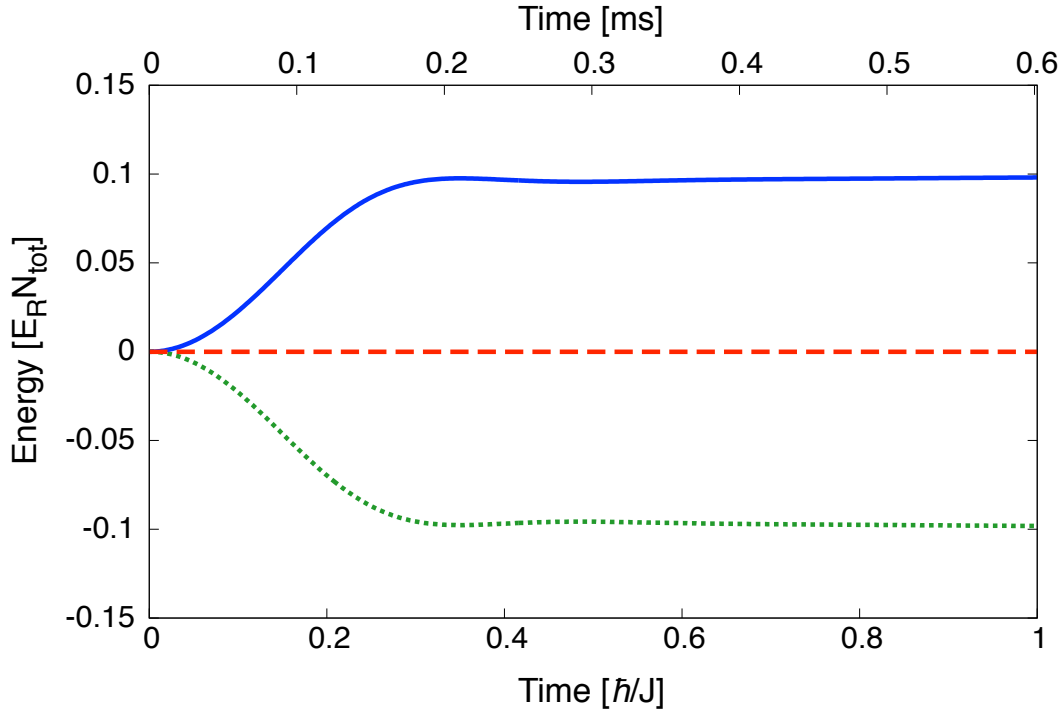


Figure 5.1: Semiclassical time evolution of the kinetic and onsite-interaction energies (green-dotted and blue-solid lines) after the sudden quench from the singly-occupied Mott-insulator state. We do not deal with finite-time effects of the ramp down process, i.e.,  $t_f = 0$ . The red-dashed line represents the total sum of these energies. In the numerical simulation, we set  $N_{\text{tot}} = M = 12^3$  and  $\lambda_f = 3.41$ . In the current setup,  $0.6 \text{ ms} \approx \hbar/J$ , where  $J$  corresponds to the final lattice depth. In this TWA simulation, we sampled  $n_{\text{mc}} = 100000$  random initial conditions of the classical field according to Eq. (5.8). Throughout this paper, we omit the standard error of the Monte-Carlo sampling, which scales with  $1/\sqrt{n_{\text{mc}}}$ , because for each simulation the error is sufficiently small to be neglected.

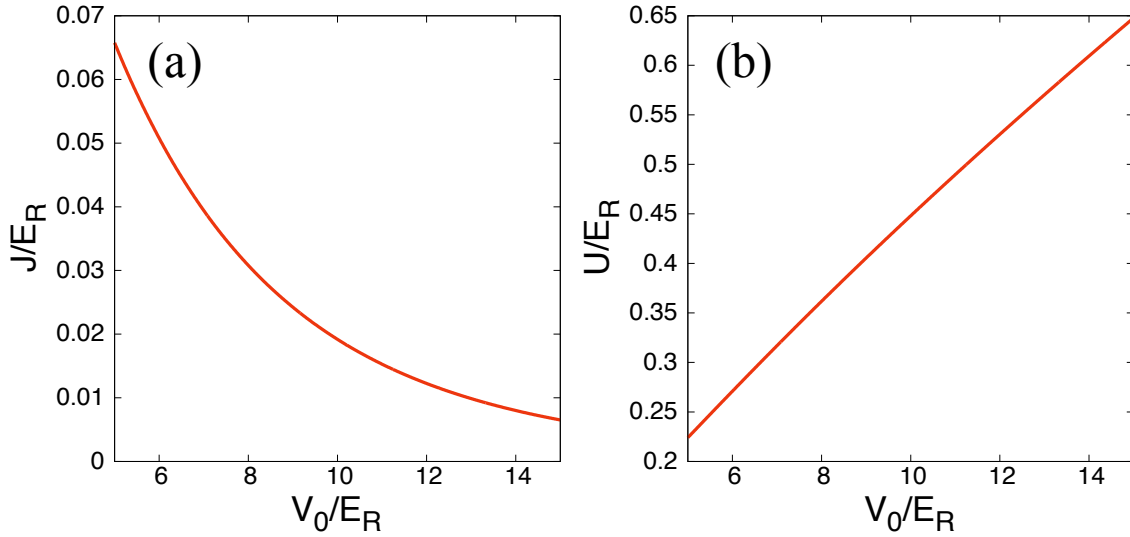


Figure 5.2: Dependence of (a) the hopping strength  $J$  and (b) the onsite-interaction strength  $U$  on the lattice depth  $V_0$ . These quantities are measured in the unit of the recoil energy  $E_R$ .

the experiment. At  $t = t_f$ , the lattice depth reaches  $V_0 = 5E_R$ , which implies  $\lambda = \lambda_f = 3.41$ . At  $t > t_f$ , the system evolves in time under the time-independent Hamiltonian  $\hat{H}[\lambda_f]$ . The phase-space averaging with the Wigner function is evaluated by using the Monte-Carlo integration, where each initial configuration of the classical fields,  $\vec{\alpha}_{\text{cl}}(0)$ , is randomly chosen from the Gaussian-Wigner function (5.8).

Before proceeding to a numerical simulation corresponding to the experimental setup, we discuss a simpler problem, i.e., an infinitesimal-time limit of the ramp-down process ( $t_f = 0$ ). In this case, the Hamiltonian is always independent of time at  $t > 0$ . Figure 5.1 depicts a numerical simulation of the kinetic and interaction energies within TWA for  $t_f = 0$ , where we set  $N_{\text{tot}} = M = 12^3$  and assume an open boundary condition. We clearly see that the semiclassical approach captures fast redistribution of the kinetic and interaction energies. The timescale of the redistribution is on the order of 0.1 ms and comparable to the experimental result. In addition, the sum of the energies, i.e.,  $E_{\text{tot}} = \langle \hat{K}(t) \rangle + \langle \hat{O}(t) \rangle$  completely maintains its initial value because the Hamiltonian of the system is independent on time. We emphasize that the redistribution dynamics presented in Fig. 5.1 cannot be recreated by means of naive mean-field theories without fluctuations from a classical configuration, such as the Gross–Pitaevskii theory and the Gutzwiller variational method.

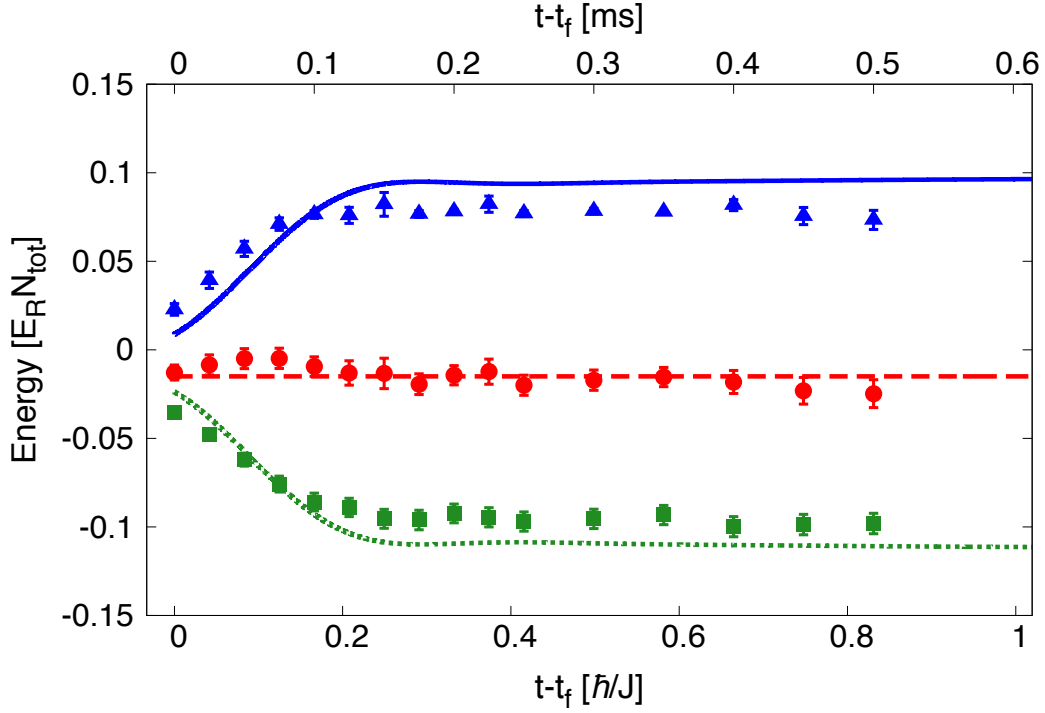


Figure 5.3: Semiclassical time evolution of the kinetic and onsite-interaction energies (green-dotted and blue-solid lines) including the ramp-down process from the singly-occupied Mott-insulator state. The red-dashed line represents the total sum of these energies. In the numerical simulation, we set  $N_{\text{tot}} = M = 30^3$  and  $\lambda_f = 3.41$ . The horizontal axis starts from  $t = t_f$ . In the TWA simulation, we sampled  $n_{\text{mc}} = 10000$  initial conditions according to Eq. (5.8). The green-square, blue-triangular, and red-circle points represent the corresponding experimental data of the ensemble-averaged kinetic, onsite-interaction, and total energies. The vertical bar for each point indicates an experimental error.

### 5.2.3 TWA versus experimental results

Here we take into account the finite-time ramp-down process in  $V_0(t)$ . The hopping strength  $J$  and the onsite-interaction strength  $U$  vary with  $V_0(t)$  as depicted in Fig. 5.2. We note again that  $V_0(t)$  linearly decreases in time from  $V_0(0) = 15E_R$  to  $V_0(t_f) = 5E_R$  where  $t_f = 0.1$  ms. In this process, the system passes through the Mott-insulating and the quantum critical regimes where the quantitative validity of TWA is justified only in rather short time  $t \ll O(\hbar/J)$ . Nevertheless, our approach is expected to be able to explain the redistribution dynamics after the quench because the system actually leaves away from these regimes in the short time.

In Fig. 5.3, we show  $\langle \hat{K}(t) \rangle$  and  $\langle \hat{O}(t) \rangle$  including the ramp-down process. The numerical simulation is performed with an open boundary condition and at  $M = N_{\text{tot}} = 30^3$ , which is comparable to the size of the actual system. Compared with the previous calculation in Subsec. 5.2.2, the

ramp-down process significantly modifies the value of each energy at  $t = t_f$ . The total energy  $E_{\text{tot}}$  decreases from zero. In addition, the timescale for the saturation toward each quasi-steady value is slightly diminished. Due to such modifications, the semiclassical result including the ramp-down process agrees very well with the experimental one, which is presented by points with error bars in Fig. 5.3, without any fitting parameter. The original experimental data are extracted from Ref. [35]. The detailed experimental setup will be provided in Ref. [36] (unpublished).

We conclude this section by making comments on the limitation of our semiclassical approach to the experimental system at intermediate final interactions and at unit filling. Although the experiment is able to access a long-time regime  $t \gg \hbar/J$ , our approach is limited to simulate a short time dynamics up to  $t \sim \hbar/J$ . To develop an efficient tool which allows one to study the long-time dynamics, e.g., a relaxation dynamics toward a thermal equilibrium state, remains to be an open and challenging issue.

### 5.3 Spatial-correlation spreading after a sudden quench

In Sec. 5.2, we corroborated the quantitative validity of the TWA method for quantum quench dynamics of the 3D Bose–Hubbard model in a weakly interacting regime ( $\lambda \gg \lambda_c$ ) starting with a Mott-insulator state. In this section, we next apply our approach to investigate time evolutions of spatial correlation spreading after sudden quenches in the 2D Bose–Hubbard model. Especially, we consider two different initial states, i.e., a coherent state, which corresponds to the ground state at  $\lambda = 0$ , and a Mott-insulator state. We discuss their difference emerging in the resulting dynamics after a sudden quench into a weakly interacting regime.

In order to characterize spatial-correlation spreading, we specifically deal with a density-density equal-time correlation function defined by

$$C_d(t) = \frac{1}{M\bar{n}^2} \sum_j \langle \hat{n}_j(t) \hat{n}_{j+d}(t) \rangle_c, \quad (5.9)$$

where  $d = (d_x, d_y)$  is a 2D relative vector between two different sites. In the definition of the correlation function,  $\langle \cdots \rangle_c$  denotes a connected correlation function, i.e.,  $\langle \hat{n}_j(t) \hat{n}_{j+d}(t) \rangle_c = \langle \hat{n}_j(t) \hat{n}_{j+d}(t) \rangle - \langle \hat{n}_j(t) \rangle \langle \hat{n}_{j+d}(t) \rangle$ . Within TWA, the connected correlator is approximated to

$$\langle \hat{n}_j(t) \hat{n}_{j+d}(t) \rangle_c \approx \overline{n_W^{(j)}(t) n_W^{(j+d)}(t)} - \overline{n_W^{(j)}(t)} \cdot \overline{n_W^{(j+d)}(t)}, \quad (5.10)$$

where the overline in the right-hand side means the phase-space average by use of the Wigner function of initial quantum states. The  $c$ -number quantity  $n_W^{(j)}$  represents the Wigner–Weyl transform of the local density  $\hat{n}_j$ , i.e.,  $n_W^{(j)} = |\alpha_j|^2 - \frac{1}{2}$ . In cold-atom experiments, the time evolution of

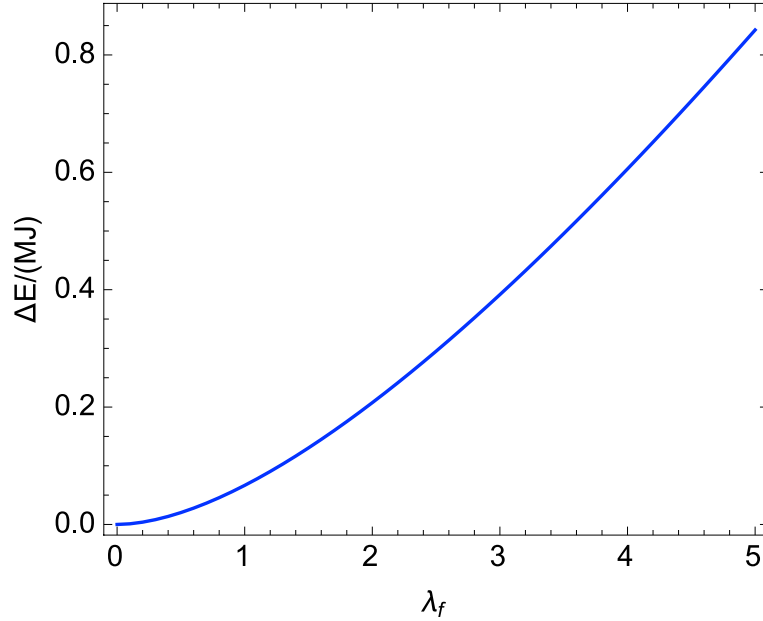


Figure 5.4: Energy deviation per site  $\Delta E/(MJ)$  of the coherent state from the ground state energy within the Bogoliubov approximation as a function of  $\lambda_f$ , where  $\bar{n} = 10$ .

the non-local density-density correlation is measurable by utilizing the quantum-gas microscope technique [12] or measuring spatial-noise correlations in a time-of-flight interference pattern of expanding gases [171, 172].

### 5.3.1 Sudden quench from a coherent state

We start from analyzing density-density correlation spreading inside a superfluid regime assuming that the system is initially in a direct-product state composed of the local coherent states  $|\bar{\alpha}\rangle_j = e^{\bar{\alpha}\hat{a}_j^\dagger - \bar{\alpha}^*\hat{a}_j}|0\rangle$ :

$$|\Psi_{\text{ini}}\rangle = \prod_j |\bar{\alpha}\rangle_j. \quad (5.11)$$

Here,  $\bar{\alpha} = \sqrt{\bar{n}}e^{i\bar{\varphi}}$  parametrizes each coherent-state vector. Calculating the Wigner–Weyl transform of this wave function (5.11), we can obtain the corresponding Wigner function as follows [49] (see also Chap. 3):

$$W_{\text{coh}}(\vec{\alpha}, \vec{\alpha}^*) = \prod_j \left\{ 2e^{-2|\alpha_j - \bar{\alpha}|^2} \right\}. \quad (5.12)$$

This Wigner function can take on non-negative values for arbitrary  $\alpha_j$ , so that there is no difficulty in the Monte-Carlo sampling of the TWA. In the following discussions, we set  $\bar{\varphi} = 0$  for simplicity.

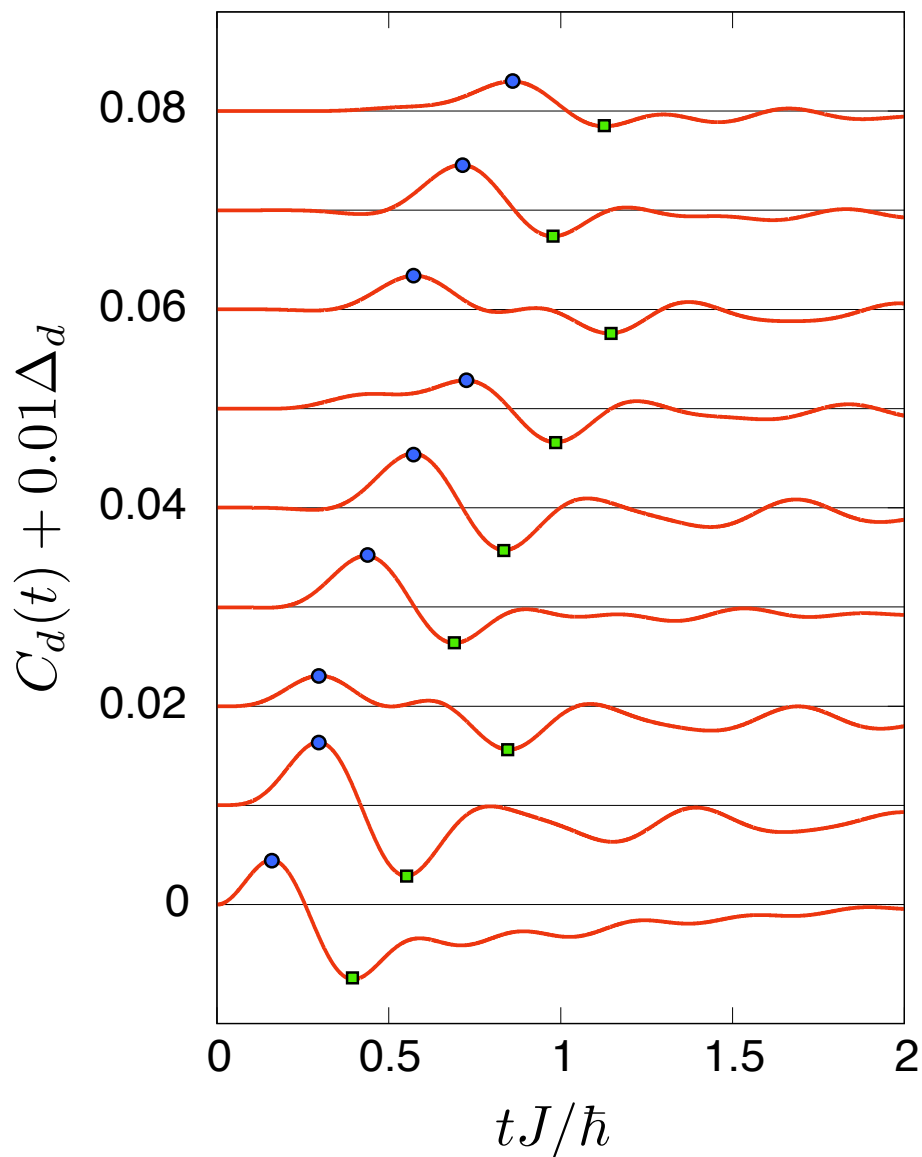


Figure 5.5: Density-density correlation spreading after the sudden quench from the coherent state at  $\lambda_f = 2$ . The blue circle and green square indicate the maximum and minimum values of the correlation function within  $tJ/\hbar \leq 3$ . The relative vector  $d = (d_x, d_y)$ , Euclidean distance  $d_E$ , and offset of correlation  $\Delta_d$  take values of  $(d_x, d_y; d_E; \Delta_d) = (0, 1; 1.00; 0)$ ,  $(1, 1; 1.41; 1)$ ,  $(0, 2; 2.00; 2)$ ,  $(1, 2; 2.24; 3)$ ,  $(2, 2; 2.83; 4)$ ,  $(0, 3; 3.00; 5)$ ,  $(1, 3; 3.16; 6)$ ,  $(2, 3; 3.617; 7)$ ,  $(0, 4; 4.00; 8)$  from the bottom to top, respectively. In the TWA simulation, we sampled  $n_{mc} = 40000$  initial conditions according to Eq. (5.12).

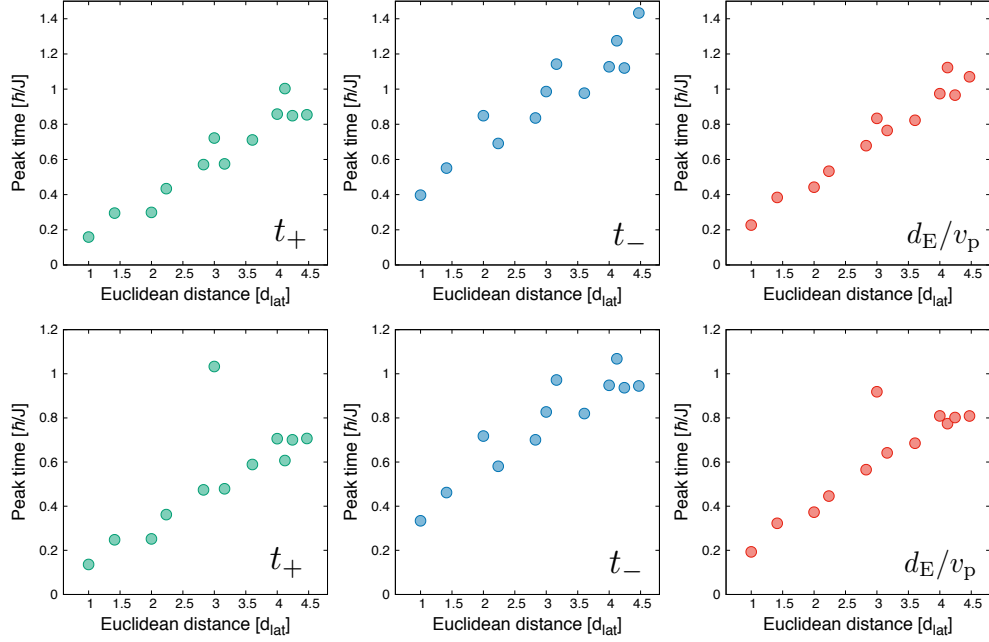


Figure 5.6: Maximum (left column), minimum (center column) and averaged (right column) peak times extracted from the TWA simulations. The vertical and horizontal axes express the peak time and Euclidean distance. The upper and lower rows correspond to  $\lambda_f = 2$  and  $\lambda_f = 4$ , respectively.

In order to keep the accuracy of TWA for a relatively long timescale, here we choose  $\bar{n} = 10$  in numerical simulations. In addition, we impose periodic boundary conditions on the system. Throughout this section, we suppose that the quench is abruptly done for an infinitesimal time, for simplicity.

Before proceeding to our main results, we calculate the energy deviation per site defined by

$$\frac{1}{M}\Delta E = \frac{1}{M} \left[ \langle \Psi_{\text{ini}} | \hat{H}_f | \Psi_{\text{ini}} \rangle - \langle \hat{H}_f \rangle_{\text{g}} \right], \quad (5.13)$$

where  $\hat{H}_f$  is the Hamiltonian at  $\lambda = \lambda_f$  and  $\langle \hat{H}_f \rangle_{\text{g}}$  means the ground-state energy of  $\hat{H}_f$ . We evaluate  $\langle \hat{H}_f \rangle_{\text{g}}$  within the standard Bogoliubov approximation for the Bose–Hubbard model as follows:

$$\langle \hat{H}_f \rangle_{\text{g}} \approx M \left[ \mathcal{E}_0 + \frac{1}{2M} \sum_{\mathbf{p} \neq 0} (E_{\mathbf{p}} - \hbar\omega_{\mathbf{p}}) \right], \quad (5.14)$$

where  $\mathbf{p} = (p_x, p_y)$  is a momentum in the first Brillouin zone,  $\mathcal{E}_0 = -4J\bar{n} + U\bar{n}^2/2$ , and  $\hbar\omega_{\mathbf{p}} = U\bar{n} + 4J \sum_{j=x,y} \sin^2[p_j d_{\text{lat}}/(2\hbar)]$ . In addition,  $E_{\mathbf{p}} = \sqrt{(\hbar\omega_{\mathbf{p}})^2 - (\bar{n}U)^2}$  is the energy of the elementary excitations (for more details, see Ref. [173]). Figure 5.4 shows  $\Delta E/(MJ)$  of the coherent state as a function of  $\lambda_f$ . Because  $\Delta E/M$  is less than the typical energy scale  $J$  over a wide range of  $\lambda_f$ ,

the dynamics after the quench from the coherent state is dominated by the low-energy elementary excitations from the ground state, i.e., the Bogoliubov quasiparticles.

Figure 5.5 monitors how density-density correlations propagate over the square lattice. In the numerical simulation, we set  $\lambda_f = 2$  and  $M = 20^2$  at  $\bar{n} = 10$ . In addition, we characterize the correlation spreading by means of the usual Euclidean distance defined by  $d_E \equiv (d_x^2 + d_y^2)^{1/2}$ . In the time evolution, we observe that a characteristic signal of correlation, i.e., a wave packet enveloping maximum (blue circle) and minimum (green square) peaks of a fine oscillation propagates over the square lattice in time. Such a fine oscillation can be interpreted as a quasi-coherent oscillation reflecting that a few elementary excitations are created by the quench.

To quantify the correlation spreading, we extract a propagation velocity of the wave packet from the numerical results in the following manner. Let us denote the peak times of the maximum and minimum values of the correlation as  $t_+$  and  $t_-$ , which are represented by the blue circles and the green squares in Fig. 5.5. For a given Euclidean distance  $d_E$ , we can define a reasonable (instantaneous) propagation velocity  $v_p$  as a harmonic average of these peak times such that

$$v_p \equiv \frac{d_E}{2} \left( \frac{1}{t_+} + \frac{1}{t_-} \right), \quad (5.15)$$

where  $d_E/v_p$  is regarded as an averaged peak time. In Fig. 5.6, we indicate  $t_+$ ,  $t_-$ , and  $d_E/v_p$  for different relative distances at  $\lambda_f = 2$  and  $\lambda_f = 4$ , respectively. It is found that the averaged peak time almost linearly increases with  $d_E$ . A linear fitting of the averaged peak times gives a mean propagation velocity,  $\bar{v}_p$ , of the wave packet. In order to compute  $\bar{v}_p$ , we take into account early twelve peaks in a timescale of  $t \sim \hbar/J$ , which are found in  $C_d(t)$  with  $d_E < 5d_{\text{lat}}$ .

Figure 5.7 shows the mean propagation velocity  $\bar{v}_p$  as a function of the final interaction  $\lambda_f$ . In the same figure, we also display twice the maximum and sound velocities of the Bogoliubov excitations,  $2v_m$  and  $2v_s$ , which are expressed as

$$v_m = \max_{\mathbf{p}} \left\{ \sqrt{\left( \frac{\partial E_{\mathbf{p}}}{\partial p_x} \right)^2 + \left( \frac{\partial E_{\mathbf{p}}}{\partial p_y} \right)^2} \right\},$$

$$v_s = \lim_{\mathbf{p} \rightarrow \mathbf{0}} \left\{ \sqrt{\left( \frac{\partial E_{\mathbf{p}}}{\partial p_x} \right)^2 + \left( \frac{\partial E_{\mathbf{p}}}{\partial p_y} \right)^2} \right\}.$$

Note that  $v_m$  coincides with  $v_s$  in the limit that  $\lambda_f \gg 1$ . It is clearly observed in Fig. 5.7 that  $\bar{v}_p$  is bounded by twice the maximum velocity  $2v_m$  over a range of  $\lambda_f \in [1, 5]$ . This numerical result is consistent with the general one of the Lieb–Robinson bound [60]. Furthermore, in the range of  $1 \leq \lambda_f \leq 3$ , the propagation velocity increases with  $\lambda_f$  in such a way that the points come close to  $2v_s$ . This feature can be attributed to the fact that the quench actually creates some elementary

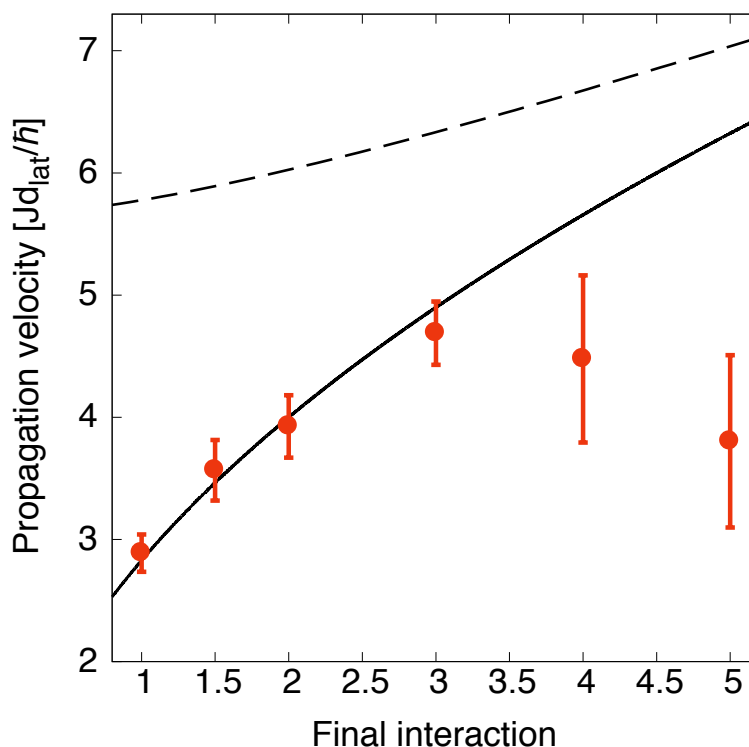


Figure 5.7: Final interaction dependence of the mean propagation velocity  $\bar{v}_p$  (circle). The solid and dashed lines represent twice the sound ( $2v_s$ ) and maximum ( $2v_m$ ) velocities of the Bogoliubov excitation, respectively. The horizontal axis expresses the final interaction  $\lambda_f$ . The vertical bar indicates the normal estimation error of the mean propagation velocity in the linear fitting (see also Fig. 5.6).

excitations at  $E_p \ll J$ , where the Bogoliubov excitations behave as phonons, because the energy deviation is relatively small (see Fig. 5.4).

In contrast, in the range of  $3 < \lambda_f \leq 5$ , the mean propagation velocity significantly deviates from  $2v_s$ . In this regime, elementary excitations with  $E_p \sim J$  can be generated because the energy deviation per particle is comparable to  $J$  as seen in Fig. 5.4. In addition, the computed propagation velocity has a large estimation error of the linear fitting. The large error is actually due to an exceptional point in, e.g.,  $C_d(t)$  at  $d_E = 3$  and  $\lambda_f = 4$  (see Fig. 5.6) that the maximum peak arises after the growth of the minimum one. Similar points also appear at  $\lambda_f = 5$ .

We conclude this subsection with comments on a previous study on similar quench dynamics of the 2D Bose–Hubbard model, which uses a time-dependent variational Monte-Carlo approach [61]. In Ref. [61], Carleo and coworkers calculated the density-density correlation function in a weakly-interacting regime starting from a superfluid ground state at  $\bar{n} = 1$ . Figure 2(b) of Ref. [61] implies an unphysical result that the propagation velocity is much greater than twice the

maximum one of the elementary excitation in the regime. While it seems to contradict the Lieb–Robinson bound, the crucial reason of such a fast propagation has not been mentioned in their paper. To characterize the wavefront motion of the correlation on the square lattice, in Ref. [61], the propagation velocity was evaluated in terms of the Manhattan distance  $d_M \equiv |d_x| + |d_y|$  [61, 174]. It is worth emphasizing that if we redefine  $\bar{v}_p$  by the Manhattan distance instead of the Euclidean one in our TWA results, it leads to a similar fast propagation as in Ref. [61]. Hence, we argue that the fast propagation beyond twice the maximum velocity seen in Ref. [61] is actually due to the unsuitable choice of the distance to define a propagation velocity.

### 5.3.2 Quench from a Mott-insulator state across a quantum phase transition

We now discuss a sudden quench from a Mott-insulator state and keep track of density-density correlation spreading, which occurs inside a weakly interacting regime. Note that the initial state corresponds to the ground state of the system at  $\lambda = \infty$ .

Figure 5.8 displays the TWA simulation of the density-density correlation after the sudden quench from the Mott-insulator state with  $\bar{n} = 10$  at  $\lambda_f = 2$  and  $M = 20^2$ . For the simulation, we utilize the approximate Wigner function (5.8). In the result, we can observe a different behavior from the case of the coherent state that a wave packet propagates as a single-peak signal with no fine oscillation in the correlation function. In this case, the velocity of the wave packet can be directly estimated from the activation time of the minimum peak itself. In Fig. 5.9, we extract the peak times from the correlation signals at  $\lambda_f = 2$  and  $\lambda_f = 4$ , respectively. In Fig. 5.10, we show the propagation velocity  $\bar{v}_p$  extracted from Fig. 5.9 as a function of  $\lambda_f$  and compare it with the results for the coherent state. Figure 5.10 reveals that  $\bar{v}_p$  is approximately independent of  $\lambda_f$  in contrast to the coherent-state case.

This qualitative difference can be understood as follows. The Mott insulator state has much larger energy deviation than that of the coherent state as shown in Fig. 5.11. This means that the Bogoliubov excitations, which are elementary excitations of the system in the presence of condensates, are no longer relevant to such high-energy dynamics. The sudden quench kicks single-particle excitations with various momenta from the initial density configuration of the Mott insulator state. The absence of the fine oscillation inside the wave packet can be regarded as reflecting an incoherent motion joined by many single-particle excitations. In addition, the single-particle picture can also explain the nearly constant velocity of the correlation spreading. Specifically, within the Hartree–Fock approximation (HFA) for the Bose particles, the group velocity of the single-particle excitation is independent of  $U$  because the interaction effect poses only a constant shift to the non-interacting band [68].

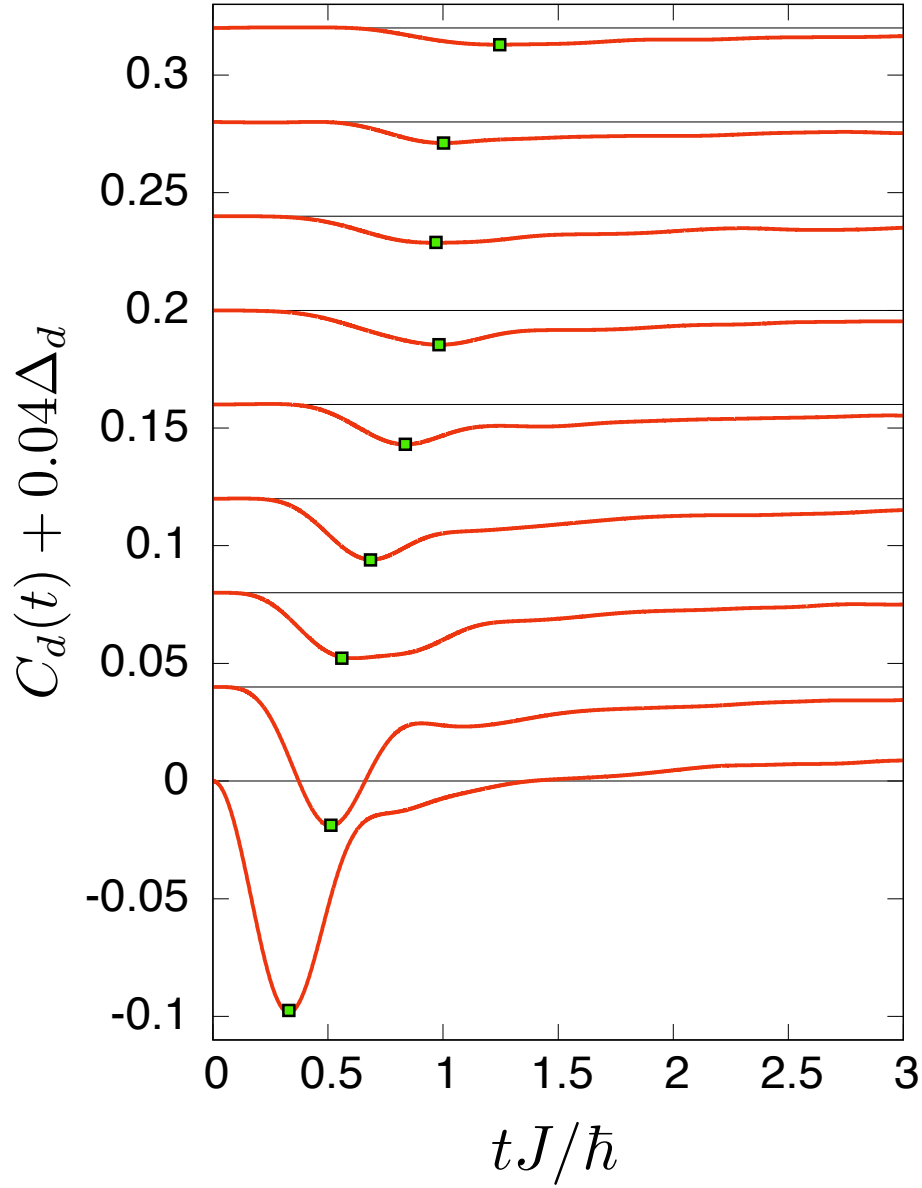


Figure 5.8: Density-density correlation spreading after the sudden quench from the Mott-insulator state at  $\lambda_f = 2$ . The green square indicates the minimum peak of the correlation signal. The relative vector  $d = (d_x, d_y)$ , Euclidean distance  $d_E$ , and offset of correlation  $\Delta_d$  take values of  $(d_x, d_y; d_E; \Delta_d) = (0, 1; 1.00; 0)$ ,  $(1, 1; 1.41; 1)$ ,  $(0, 2; 2.00; 2)$ ,  $(1, 2; 2.24; 3)$ ,  $(2, 2; 2.83; 4)$ ,  $(0, 3; 3.00; 5)$ ,  $(1, 3; 3.16; 6)$ ,  $(2, 3; 3.61; 7)$ ,  $(0, 4; 4.00; 8)$  from the bottom to the top, respectively. In the TWA simulation, we sampled  $n_{\text{mc}} = 10000$  initial conditions according to Eq. (5.8).

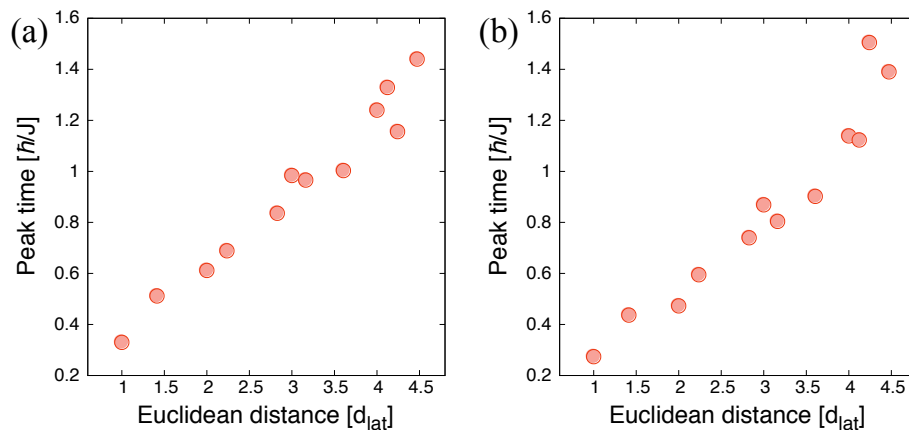


Figure 5.9: Extracted peak times from the correlation signals at (a)  $\lambda_f = 2$  and (b)  $\lambda_f = 4$  quenched from the Mott-insulator state. The vertical and horizontal axes indicate the peak time and Euclidean distance, respectively.

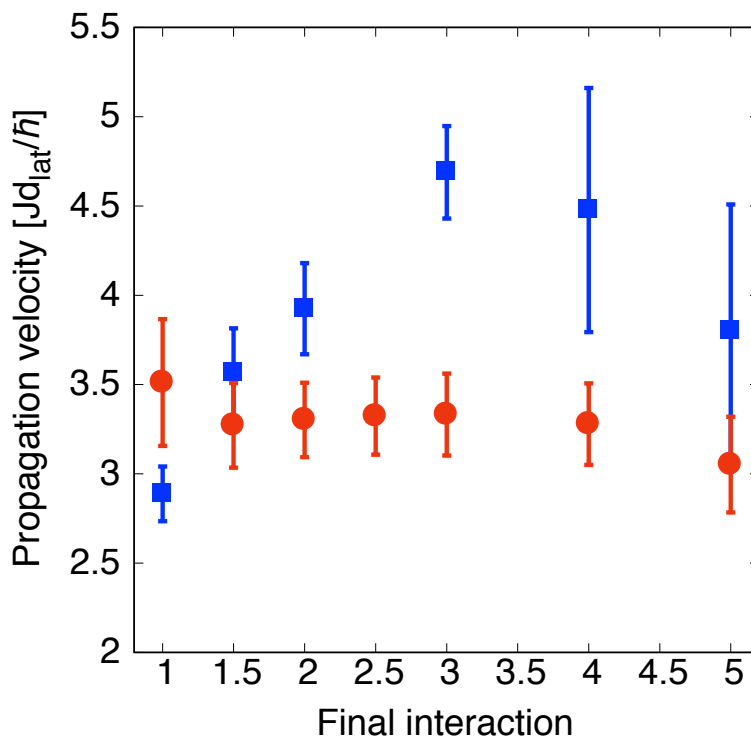


Figure 5.10: Final interaction dependence of the mean propagation velocity  $\bar{v}_p$  (red circle). The blue square represents the result of the case of the coherent state shown in Fig. 5.6. The vertical bar indicates the normal estimation error of the linear fitting of the peak times.

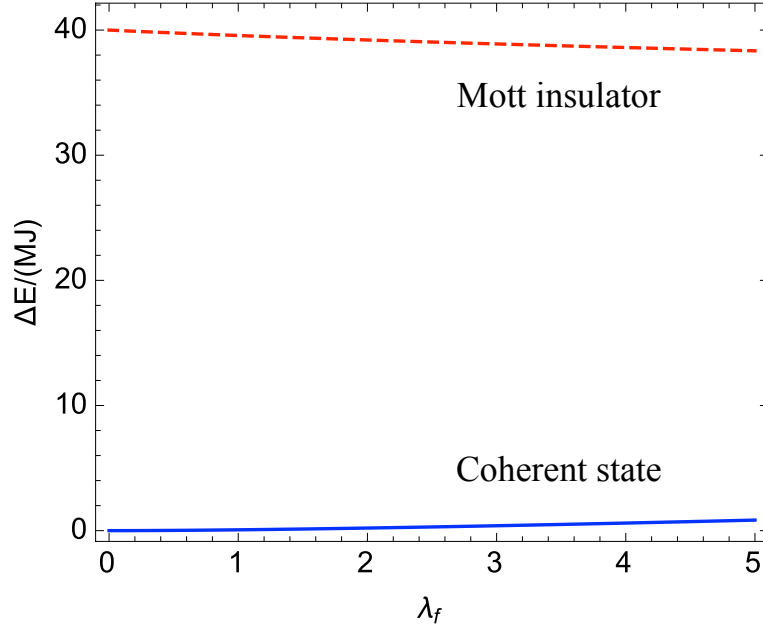


Figure 5.11: Energy deviation  $\Delta E/(MJ)$  of the Mott-insulator state from the ground state energy per site of the Hamiltonian at  $\lambda = \lambda_f$  (red-dashed line). The blue-solid line (same as the one in Fig. 5.4) represents the energy deviation when the system is initially prepared in the coherent state.

In order to verify the property of the spreading velocity in practice, we apply the HFA to the two-particle Green's function in the Bose–Hubbard model. Let us consider the one- and two-particle Green's function of the lattice bosons,

$$G_{j,j'}(t,t') = \frac{1}{i} \left\langle T \left\{ \hat{a}_j(t) \hat{a}_{j'}^\dagger(t') \right\} \right\rangle,$$

$$G_{j_1,j_2,j'_1,j'_2}^{(2)}(t_1,t_2,t'_1,t'_2) = \frac{1}{i^2} \left\langle T \left\{ \hat{a}_{j_1}(t_1) \hat{a}_{j_2}(t_2) \hat{a}_{j'_2}^\dagger(t'_2) \hat{a}_{j'_1}^\dagger(t'_1) \right\} \right\rangle,$$

where  $T \{ \dots \}$  indicates a chronological-time ordering for operator products inside the bracket. In what follows, we deal with the one-dimensional case for simplicity. From the Heisenberg equation for  $\hat{a}_j(t)$ ,  $G_{j,j'}(t,t')$  obeys the following equation of motion:

$$i\hbar \frac{\partial}{\partial t} G_{j,j'}(t,t') + JG_{j+1,j'}(t,t') + JG_{j-1,j'}(t,t') - iU G_{j,j',j}^{(2)}(t,t_1,t',t_1 + \delta) \Big|_{t_1=t} = \hbar\delta(t-t')\delta_{j,j'},$$

where  $\delta$  is a positive and infinitesimal shift. In the HFA,  $G_{j,j',j}^{(2)}(t,t_1,t',t_1 + \delta)$  is factorized into two parts as follows [175]:

$$G_{j,j',j}^{(2)}(t,t_1,t',t_1 + \delta) = G_{j,j'}(t,t')G_{j,j}(t_1,t_1 + \delta) + G_{j,j}(t,t_1 + \delta)G_{j,j'}(t_1,t'). \quad (5.16)$$

This treatment can be regarded as a mean-field approximation, where any correlations between two indistinguishable bosons are neglected [175]. At  $t_1 = t$ , we find that

$$G_{j,j}(t, t_1 + \delta) = G_{j,j}(t_1, t_1 + \delta) = -i\langle \hat{n}_j(t) \rangle = -i\bar{n}. \quad (5.17)$$

Thus, the equation of motion results in a closed equation:

$$\left\{ i\hbar \frac{\partial}{\partial t} - 2U\bar{n} \right\} G_{j,j'}(t, t') + JG_{j+1,j'}(t, t') + JG_{j-1,j'}(t, t') = \hbar\delta(t - t')\delta_{j,j'}. \quad (5.18)$$

This equation means a constant shift of the pole of the one-particle Green's function as

$$\epsilon_{\text{free}}(p) \rightarrow \epsilon_{\text{free}}(p) + 2U\bar{n}, \quad (5.19)$$

where  $\epsilon_{\text{free}}(p) = -2J\cos(pd_{\text{lat}}/\hbar)$  is the single-particle dispersion at  $U = 0$ . This result says that the interaction does not change the group velocity of the single-particle excitation within the HFA. Notice that this result is valid for the 2D case because the dimensionality enters only into the free dispersion.

## 5.4 Summary of this chapter

In conclusion of this chapter, we studied the time evolution of the 2D and 3D Bose–Hubbard models after a sudden quench to a weakly interacting regime by using the semiclassical TWA method. We applied the TWA to analyze the redistribution dynamics of the kinetic and onsite-interaction energies after a quench from the singly-occupied Mott insulator state in the 3D Bose–Hubbard model. It was reported that our semiclassical result agrees very well with the experimental one without any fitting parameter.

We also studied the density-density correlation spreading after a sudden quench in the 2D Bose–Hubbard model at a large filling factor. We numerically showed that when the system is initially prepared in the coherent state, then the mean propagation velocity of the correlation wave packet strongly depends on the final interaction strength reflecting the properties of the low-energy elementary excitation in the weakly interacting regime. In contrast, we found that when the initial quantum state is the Mott insulator state, then the mean propagation velocity is almost independent of the final interaction. We also provided a physical interpretation to such a result in terms of the property of the high-energy single-particle excitations.

# Chapter 6

## Conclusions and outlooks

In this thesis, we have focused on near- and far-from-equilibrium dynamics of ultracold Bose atoms in optical lattices. Especially, we have worked on theoretical analyses of several non-equilibrium quantum many-body problems motivated by experimental works using approaches in which effects of fluctuations are taken into account beyond the naive mean-field treatments. Hence, this thesis offers an important step towards deeper understanding of quantum many-body phenomena realized in real experiments of ultracold atoms.

In Chap. 4, we studied the Higgs mode of strongly-interacting superfluid Bose gases in the three-dimensional (3D) cubic optical lattice, especially, the visibility in the experimental systems. To excite the Higgs mode in the optical lattice, we have discussed two experimentally feasible protocols, i.e., the kinetic energy and onsite interaction modulations and formulated the corresponding response functions using the linear-response theory. We used the effective-model representation of the strongly-interacting Bose–Hubbard model and calculated the response functions combining it with the finite-temperature Green’s function theory. Our perturbative calculations provided quantum and thermal fluctuation corrections to the spectral properties of the Higgs mode. We showed that if the system is uniform, the Higgs mode is then sufficiently robust and can exist as a well-defined resonance peak even at typical temperatures of experiments. This should be contrasted with the two-dimensional case, in which the corresponding resonance becomes rather broad due to the fluctuations. Furthermore, we have analyzed the non-uniform trap effect on the uniform response functions at unit filling on the basis of the local-density approximation. We demonstrated that the resonance peak is significantly broadened due to the trapping potential when the modulations are applied globally to the entire system. In order to extract a sharp resonance peak from the smeared response, we discussed partial modulations around the trap center. The results with a modulation radius  $R_{\text{mod}} < 0.5R_{\text{TF}}$  showed that a well-defined resonance peak of the Higgs mode can survive at typical temperatures.

One of the promising directions associated with the visibility of the Higgs mode is to analyze

the same response functions of the 3D Bose–Hubbard model by performing quantum Monte-Carlo (QMC) simulations. Recently, a spectral function characterizing the response of the Higgs mode has been calculated using a QMC technique for a 3D quantum antiferromagnet [176], which has a quantum critical point described by the relativistic  $O(3)$  scalar model. The results of Ref. [176] remarkably show that there appears a sufficiently sharp resonance peak of the Higgs mode in the spectral function. It seems to be an intriguing problem that one applies the same method to the 3D Bose–Hubbard model with a non-uniform potential and validates our qualitative results through comparing them with more quantitative ones of QMC simulations. Furthermore, it is also interesting to employ the functional (or non-perturbative) renormalization group approach for computing the response functions of the 3D Bose–Hubbard model [40, 42, 177, 178].

In Chap. 5, we have investigated far-from-equilibrium dynamics after a sudden quantum quench in Bose gases trapped by optical lattices. First, applying the truncated-Wigner approximation (TWA), we analyzed the redistribution dynamics of the kinetic and interaction energies of the 3D Bose–Hubbard model after a quantum quench from a singly-occupied Mott-insulator state. Through a direct comparison with the experimental data, it was reported that our semiclassical results capture the characteristic behavior of redistribution and remarkably agree with the data with no fitting parameter. Furthermore, we also studied the spreading of the density-density correlation over space in the two-dimensional (2D) Bose–Hubbard model at a large filling factor. Especially, we focused on the initial state dependence of the spreading dynamics. We numerically showed that when the system is initially prepared in the coherent state, then the propagation velocity of the correlation wave packet strongly depends on the final interaction strength. We discussed that this feature can be understood from the properties of the low-energy elementary excitation in the weakly-interacting regime. In contrast, we demonstrated that when the initial quantum state is the Mott insulator state, then the propagation velocity of correlations is almost independent of the final interaction. We also provided a physical interpretation to such a result in terms of the property of the high-energy single-particle excitations, whose spectrum was explicitly obtained from the Hartree–Fock approximation.

The experiment of the quantum optics group at Kyoto University has also studied correlation-spreading dynamics in a 2D strongly-interacting Bose-gas system [36]. However, our semi-classical scheme is not feasible for simulating that dynamics accurately because the *quantum-to-classical correspondence* of dynamics in terms of the Gross–Pitaevskii equation is no longer valid in that parameter regime. Recently, a promising approach to strongly-interacting dynamics has been suggested by Davidson and Polkovnikov and referred to as the  $SU(3)$  truncated-Wigner approximation [119]. This technique, which is applied to a quantum spin system having a local Hilbert space of three dimensions, increases phase-space variables of the classical limit of the

quantum system in order to linearize the local interaction with respect to the spin variables. Applying the SU(3)TWA, we can characterize the wave-packet motion seen in the correlation function observed by the experiment [179]. A similar technique of increasing phase-space variables can also be developed for the case of fermions and successfully improves far-from-equilibrium dynamics of strongly-interacting fermions [180]. These results will be presented by publications sometime in 2019 (not included in this thesis).

# Appendix A

## Energy absorption due to the onsite-interaction strength modulations

In this appendix we derive the relation between the response function (4.3) and energy absorbed by the system for a finite-time period of the onsite-interaction strength modulation, according to the literatures about the hopping strength modulations [95, 152].

As seen in Sec. 4.1.2, the time-dependent Hamiltonian  $\mathcal{H}_{\text{BH}}(t) = \mathcal{H}_{\text{BH}} + \Delta_U(t)O$  describes the behavior of the system that is initially in a thermal equilibrium state and is driven by the small and periodic modulation  $U \rightarrow (1 + \Delta_U(t))U = (1 + \delta_U \cos(\omega t))U$  at a fixed  $\omega$ . If we assume that  $\rho(t)$  is the total density operator at  $t$ , which approaches the equilibrium one  $\rho_{\text{eq}}$  as  $t \rightarrow -\infty$ , then the total energy of the system at  $t$  is given by  $E(t) = \langle \mathcal{H}_{\text{BH}}(t) \rangle(t) = \text{Tr} \rho(t) \mathcal{H}_{\text{BH}}(t)$ . We can verify easily that its instantaneous change rate  $dE(t)/dt$  is proportional to only the instantaneous average of  $O$  with a oscillation factor:

$$\begin{aligned} \frac{dE}{dt} &= \dot{\Delta}_U(t) \langle O \rangle(t) \\ &= -\omega \delta_U \sin(\omega t) \langle O \rangle(t). \end{aligned} \quad (\text{A.1})$$

Using the basic result of the linear response theory [165], the response of  $O$  to the  $U$  modulation, it is defined by  $\Delta \langle O \rangle(t) \equiv \langle O \rangle(t) - \langle O \rangle_{\text{eq}}$ , is related to  $\Delta_U(t)$  such as

$$\Delta \langle O \rangle(t) = \int_{-\infty}^t D_{OO}^{\text{R}}(t-t') \Delta_U(t'), \quad (\text{A.2})$$

where  $D_{OO}^{\text{R}}(t-t')$  is the response function given by Eq. (4.3). Substituting  $\Delta_U(t) = \delta_U \cos(\omega t)$  into this equation (A.2), we obtain

$$\begin{aligned} \Delta \langle O \rangle(t) &= \delta_U \text{Re} \left\{ e^{i\omega t} \chi_{OO}^*(\omega) \right\} \\ &= \delta_U \left\{ \cos(\omega t) \text{Re} \chi_{OO}(\omega) + \sin(\omega t) \text{Im} \chi_{OO}(\omega) \right\}. \end{aligned} \quad (\text{A.3})$$

Averaging Eq. (A.1) over one period  $t_{\text{mod}} = 2\pi/\omega$  and using Eq. (A.3), we finally obtain the mean energy absorbed by the system for a period of  $t_{\text{mod}}$

$$\Delta E(\omega) = \frac{1}{t_{\text{mod}}} \int_0^{t_{\text{mod}}} dt \frac{dE}{dt} = \frac{(\delta_O)^2}{2} \omega S_{OO}(\omega), \quad (\text{A.4})$$

where  $S_{OO}(\omega) = -\text{Im}\chi_{OO}(\omega)$  is the spectral function. One can measure  $\Delta E(\omega)$  accurately by using the quantum-gas microscope technique. The relation (A.4) reveals that for the modulations of  $U$ , the experimental observable  $\Delta E(\omega)$  is related only to the  $O$ -to- $O$  response function  $D_{OO}^R(t-t')$ .

# Appendix B

## Coefficients in the effective model

In this appendix we give the coefficients in each partial Hamiltonian  $\mathcal{H}_{\text{eff}}^{(l)}$  for  $l = 0, 1, 2, 3, 4$ . To simplify our discussion, we define a formal representation of the pseudospin operators as follows:

$$\begin{aligned} S_i^+ &= t_i^\dagger T_1 t_i, & S_i^- &= t_i^\dagger T_2 t_i, & S_i^z &= t_i^\dagger T_3 t_i, \\ (S_i^z)^2 &= t_i^\dagger T_4 t_i, & S_i^z S_i^+ &= t_i^\dagger T_5 t_i, & S_i^- S_i^z &= t_i^\dagger T_6 t_i, \end{aligned} \quad (\text{B.1})$$

where  $t_i = (t_{1,i}, t_{0,i}, t_{-1,i})^\text{T}$ . We have introduced matrices  $T_1, T_2, \dots, T_6$  defined by

$$\begin{aligned} T_1 &= \begin{pmatrix} 0 & \sqrt{2} & 0 \\ 0 & 0 & \sqrt{2} \\ 0 & 0 & 0 \end{pmatrix}, & T_2 &= \begin{pmatrix} 0 & 0 & 0 \\ \sqrt{2} & 0 & 0 \\ 0 & \sqrt{2} & 0 \end{pmatrix}, \\ T_3 &= \begin{pmatrix} 1 & 0 & 0 \\ 0 & 0 & 0 \\ 0 & 0 & -1 \end{pmatrix}, & T_4 &= \begin{pmatrix} 1 & 0 & 0 \\ 0 & 0 & 0 \\ 0 & 0 & 1 \end{pmatrix}, \\ T_5 &= \begin{pmatrix} 0 & \sqrt{2} & 0 \\ 0 & 0 & 0 \\ 0 & 0 & 0 \end{pmatrix}, & T_6 &= \begin{pmatrix} 0 & 0 & 0 \\ \sqrt{2} & 0 & 0 \\ 0 & 0 & 0 \end{pmatrix}. \end{aligned} \quad (\text{B.2})$$

The canonical transformation (2.55) can be regarded as the linear transformation from the old basis  $t_i$  to the new one  $b_i = (b_{1,i}, b_{0,i}, b_{2,i})^\text{T}$ . After the transformation, the elements of the matrices

in the new basis are given by

$$\begin{aligned}
\tilde{T}_1 &= \begin{pmatrix} -\sqrt{2}s_1c_1(s_2+c_2) & \sqrt{2}(s_1^2c_2-c_1^2s_2) & -\sqrt{2}s_1s_2 \\ \sqrt{2}(s_1^2s_2-c_1^2c_2) & \sqrt{2}s_1c_1(s_2+c_2) & -\sqrt{2}c_1s_2 \\ \sqrt{2}s_1c_2 & \sqrt{2}c_1c_2 & 0 \end{pmatrix}, \\
\tilde{T}_2 &= \begin{pmatrix} -\sqrt{2}s_1c_1(s_2+c_2) & \sqrt{2}(s_1^2s_2-c_1^2c_2) & \sqrt{2}s_1c_2 \\ \sqrt{2}(s_1^2c_2-c_1^2s_2) & \sqrt{2}s_1c_1(s_2+c_2) & \sqrt{2}c_1c_2 \\ -\sqrt{2}s_1s_2 & -\sqrt{2}c_1s_2 & 0 \end{pmatrix}, \\
\tilde{T}_3 &= \begin{pmatrix} c_1^2(s_2^2-c_2^2) & s_1c_1(c_2^2-s_2^2) & -2c_1s_2c_2 \\ s_1c_1(c_2^2-s_2^2) & s_1^2(s_2^2-c_2^2) & 2s_1s_2c_2 \\ -2c_1s_2c_2 & 2s_1s_2c_2 & c_2^2-s_2^2 \end{pmatrix}, \\
\tilde{T}_4 &= \begin{pmatrix} c_1^2 & -s_1c_1 & 0 \\ -s_1c_1 & s_1^2 & 0 \\ 0 & 0 & 1 \end{pmatrix}, \\
\tilde{T}_5 &= \begin{pmatrix} -\sqrt{2}s_1c_1s_2 & -\sqrt{2}c_1^2s_2 & 0 \\ \sqrt{2}s_1^2s_2 & \sqrt{2}s_1c_1s_2 & 0 \\ \sqrt{2}s_1c_2 & \sqrt{2}c_1c_2 & 0 \end{pmatrix}, \\
\tilde{T}_6 &= \begin{pmatrix} -\sqrt{2}s_1c_1s_2 & \sqrt{2}s_1^2s_2 & \sqrt{2}s_1c_2 \\ -\sqrt{2}c_1^2s_2 & \sqrt{2}s_1c_1s_2 & \sqrt{2}c_1c_2 \\ 0 & 0 & 0 \end{pmatrix}. \tag{B.3}
\end{aligned}$$

In the following equations, we express the matrix elements of each matrix by

$$\tilde{T}_\mu = \begin{pmatrix} (\tilde{T}_\mu)_{11} & (\tilde{T}_\mu)_{10} & (\tilde{T}_\mu)_{12} \\ (\tilde{T}_\mu)_{01} & (\tilde{T}_\mu)_{00} & (\tilde{T}_\mu)_{02} \\ (\tilde{T}_\mu)_{21} & (\tilde{T}_\mu)_{20} & (\tilde{T}_\mu)_{22} \end{pmatrix}, \text{ for } \mu = 1, 2, \dots, 6.$$

In terms of the matrix elements, the coefficients in  $\mathcal{H}_{\text{eff}}^{(0)}$  are given by

$$A_0 = -\frac{Jn_0z}{2}\{(\tilde{T}_1)_{00} + \delta\nu(\tilde{T}_5)_{00}\}^2, \tag{B.4}$$

$$\tilde{A}_0 = \frac{U}{2}(\tilde{T}_4)_{00} - B(\tilde{T}_3)_{00}. \tag{B.5}$$

The coefficients in  $\mathcal{H}_{\text{eff}}^{(1)}$  are given by

$$\begin{aligned}
A_1 &= -\frac{Jn_0z}{2}\{(\tilde{T}_1)_{00} + \delta\nu(\tilde{T}_5)_{00}\} \\
&\quad \times \left[ (\tilde{T}_1)_{01} + (\tilde{T}_1)_{10} + \delta\nu(\tilde{T}_5)_{01} + \delta\nu(\tilde{T}_5)_{10} \right], \tag{B.6}
\end{aligned}$$

$$\begin{aligned}
B_1 &= -\frac{Jn_0z}{2}\{(\tilde{T}_1)_{00} + \delta\nu(\tilde{T}_5)_{00}\} \\
&\quad \times \left[ (\tilde{T}_1)_{02} + (\tilde{T}_1)_{20} + \delta\nu(\tilde{T}_5)_{20} \right], \tag{B.7}
\end{aligned}$$

$$\tilde{A}_1 = \frac{U}{2}(\tilde{T}_4)_{10} - B(\tilde{T}_3)_{10}, \tag{B.8}$$

$$\tilde{B}_1 = -B(\tilde{T}_3)_{20}. \tag{B.9}$$

The coefficients in  $\mathcal{H}_{\text{eff}}^{(2)}$  are given by

$$A_2 = -Jn_0z\{(\tilde{T}_1)_{00} + \delta\nu(\tilde{T}_5)_{00}\{(\tilde{T}_1)_{11} + \delta\nu(\tilde{T}_5)_{11}\}, \quad (\text{B.10})$$

$$B_2 = -\frac{Jn_0z}{2} \left[ \{(\tilde{T}_1)_{00} + \delta\nu(\tilde{T}_5)_{00}\{(\tilde{T}_1)_{21} + \delta\nu(\tilde{T}_5)_{21}\} + (\tilde{T}_1)_{12}\{(\tilde{T}_1)_{00} + \delta\nu(\tilde{T}_5)_{00}\} \right], \quad (\text{B.11})$$

$$D_2 = -\frac{Jn_0z}{2} \{(\tilde{T}_1)_{10} + \delta\nu(\tilde{T}_5)_{10}\{(\tilde{T}_1)_{01} + \delta\nu(\tilde{T}_5)_{01}\}, \quad (\text{B.12})$$

$$E_2 = -\frac{Jn_0z}{2} \left[ \{(\tilde{T}_1)_{10} + \delta\nu(\tilde{T}_5)_{10}\}^2 + \{(\tilde{T}_1)_{01} + \delta\nu(\tilde{T}_5)_{01}\}^2 \right], \quad (\text{B.13})$$

$$F_2 = -\frac{Jn_0z}{2} \left[ \{(\tilde{T}_1)_{20} + \delta\nu(\tilde{T}_5)_{20}\{(\tilde{T}_1)_{10} + \delta\nu(\tilde{T}_5)_{10}\} + (\tilde{T}_1)_{02}\{(\tilde{T}_1)_{01} + \delta\nu(\tilde{T}_5)_{01}\} \right], \quad (\text{B.14})$$

$$G_2 = -\frac{Jn_0z}{2} \left[ \{(\tilde{T}_1)_{20} + \delta\nu(\tilde{T}_5)_{20}\{(\tilde{T}_1)_{01} + \delta\nu(\tilde{T}_5)_{01}\} + (\tilde{T}_1)_{02}\{(\tilde{T}_1)_{10} + \delta\nu(\tilde{T}_5)_{10}\} \right], \quad (\text{B.15})$$

$$H_2 = -\frac{Jn_0z}{2} (\tilde{T}_1)_{02}\{(\tilde{T}_1)_{20} + \delta\nu(\tilde{T}_5)_{20}\}, \quad (\text{B.16})$$

$$I_2 = -\frac{Jn_0z}{2} \left[ \{(\tilde{T}_1)_{20} + \delta\nu(\tilde{T}_5)_{20}\}^2 + (\tilde{T}_1)_{02}^2 \right], \quad (\text{B.17})$$

$$\tilde{A}_2 = \frac{U}{2} (\tilde{T}_4)_{11} - B(\tilde{T}_3)_{11}, \quad (\text{B.18})$$

$$\tilde{B}_2 = -B(\tilde{T}_3)_{12}, \quad (\text{B.19})$$

$$\tilde{C}_2 = \frac{U}{2} (\tilde{T}_4)_{22} - B(\tilde{T}_3)_{22}. \quad (\text{B.20})$$

The coefficients in  $\mathcal{H}_{\text{eff}}^{(3)}$  are given by

$$A_3 = -\frac{Jn_0z}{2} \{(\tilde{T}_1)_{11} + \delta\nu(\tilde{T}_5)_{11}\{(\tilde{T}_1)_{10} + (\tilde{T}_1)_{01} + \delta\nu(\tilde{T}_5)_{10} + \delta\nu(\tilde{T}_5)_{01}\}, \quad (\text{B.21})$$

$$B_3 = -\frac{Jn_0z}{2} \{(\tilde{T}_1)_{11} + \delta\nu(\tilde{T}_5)_{11}\{(\tilde{T}_1)_{20} + (\tilde{T}_1)_{02} + \delta\nu(\tilde{T}_5)_{20}\}, \quad (\text{B.22})$$

$$C_3 = -\frac{Jn_0z}{2} \left[ \{(\tilde{T}_1)_{10} + \delta\nu(\tilde{T}_5)_{10}\}(\tilde{T}_1)_{12} + \{(\tilde{T}_1)_{21} + \delta\nu(\tilde{T}_5)_{21}\}\{(\tilde{T}_1)_{01} + \delta\nu(\tilde{T}_5)_{01}\} \right], \quad (\text{B.23})$$

$$D_3 = -\frac{Jn_0z}{2} \left[ \{(\tilde{T}_1)_{10} + \delta\nu(\tilde{T}_5)_{10}\{(\tilde{T}_1)_{21} + \delta\nu(\tilde{T}_5)_{21}\} + \{(\tilde{T}_1)_{12}\{(\tilde{T}_1)_{01} + \delta\nu(\tilde{T}_5)_{01}\} \right], \quad (\text{B.24})$$

$$E_3 = -\frac{Jn_0z}{2} \left[ \{(\tilde{T}_1)_{21} + \delta\nu(\tilde{T}_5)_{21}\{(\tilde{T}_1)_{20} + \delta\nu(\tilde{T}_5)_{20}\} + (\tilde{T}_1)_{02}(\tilde{T}_1)_{12} \right], \quad (\text{B.25})$$

$$F_3 = -\frac{Jn_0z}{2} \left[ (\tilde{T}_1)_{02}\{(\tilde{T}_1)_{21} + \delta\nu(\tilde{T}_5)_{21}\} + (\tilde{T}_1)_{12}\{(\tilde{T}_1)_{20} + \delta\nu(\tilde{T}_5)_{20}\} \right], \quad (\text{B.26})$$

Finally, the coefficients in  $\mathcal{H}_{\text{eff}}^{(4)}$  are given by

$$A_4 = -\frac{Jn_0z}{2}\{(\tilde{T}_1)_{11} + \delta\nu(\tilde{T}_5)_{11}\}^2, \quad (\text{B.27})$$

$$B_4 = -\frac{Jn_0z}{2}(\tilde{T}_1)_{12}\{(\tilde{T}_1)_{21} + \delta\nu(\tilde{T}_5)_{21}\}, \quad (\text{B.28})$$

$$C_4 = -\frac{Jn_0z}{2}\{(\tilde{T}_1)_{11} + \delta\nu(\tilde{T}_5)_{11}\}[(\tilde{T}_1)_{12} + (\tilde{T}_1)_{21} + \delta\nu(\tilde{T}_5)_{21}], \quad (\text{B.29})$$

$$D_4 = -\frac{Jn_0z}{2}\left[\{(\tilde{T}_1)_{21} + \delta\nu(\tilde{T}_5)_{21}\}^2 + (\tilde{T}_1)_{12}^2\right]. \quad (\text{B.30})$$

# Bibliography

- [1] D. Jaksch, C. Bruder, J. I. Cirac, C. W. Gardiner, and P. Zoller, *Phys. Rev. Lett.* **81**, 3108 (1998).
- [2] M. Greiner, O. Mandel, T. Esslinger, T. W. Hänsch, and I. Bloch, *Nature* **415**, 39 (2002).
- [3] D. Jaksch and P. Zoller, *Ann. Phys.* **315**, 52 (2005).
- [4] I. Bloch, J. Dalibard, and W. Zwerger, *Rev. Mod. Phys.* **80**, 885 (2008).
- [5] M. Lewenstein, A. Sanpera, and V. Ahufinger, *Ultracold Atoms in Optical Lattices: Simulating Quantum Many-Body Systems* (Oxford University Press, Oxford, 2012).
- [6] C. Gross and I. Bloch, *Science* **357**, 995 (2017).
- [7] W. Hofstetter and T. Qin, *J. Phys. B: At. Mol. Opt. Phys.* **51**, 082001 (2018).
- [8] C. Chin, R. Grimm, P. Julienne, and E. Tiesinga, *Rev. Mod. Phys.* **82**, 1225 (2010).
- [9] S. Trotzky, L. Pollet, F. Gerbier, U. Schnorrberger, I. Bloch, N. V. Prokof'ev, B. Svistunov, and M. Troyer, *Nat. Phys.* **6**, 998 (2010).
- [10] M. Endres, M. Cheneau, T. Fukuhara, C. Weitenberg, P. Schauß, C. Gross, L. Mazza, M. C. Bañuls, I. Bloch, and S. Kuhr, *Science* **334**, 200 (2011).
- [11] S. Trotzky, Y-A. Chen, A. Flesch, I. P. McCulloch, U. Schollwöck, J. Eisert, and I. Bloch, *Nat. Phys.* **8**, 325 (2012).
- [12] M. Cheneau, P. Barmettler, D. Poletti, M. Endres, P. Schauß, T. Fukuhara, C. Gross, I. Bloch, C. Kollath, and S. Kuhr, *Nature* **481**, 484 (2012).
- [13] A. Mazurenko, C. S. Chiu, G. Ji, M. F. Parsons, M. Kanász-Nagy, R. Schmidt, F. Grusdt, E. Demler, D. Greif, and M. Greiner, *Nature* **545**, 462 (2017).

- 
- [14] D. Greif, M. F. Parsons, A. Mazurenko, C. S. Chiu, S. Blatt, F. Huber, G. Ji, and M. Greiner, *Science* **351**, 953 (2016).
- [15] J. T. Stewart, J. P. Gaebler, and D. S. Jin, *Nature* **454**, 744 (2008).
- [16] T. Stöferle, H. Moritz, C. Schori, M. Köhl, and T. Esslinger, *Phys. Rev. Lett.* **92**, 130403 (2004).
- [17] C. Schori, T. Stöferle, H. Moritz, M. Köhl, and T. Esslinger, *Phys. Rev. Lett.* **93**, 240402 (2004).
- [18] U. Bissbort, S. Götze, Y. Li, J. Heinze, J. S. Krauser, M. Weinberg, C. Becker, K. Sengstock, and W. Hofstetter, *Phys. Rev. Lett.* **106**, 205303 (2011).
- [19] M. Endres, T. Fukuhara, D. Pekker, M. Cheneau, P. Schauß, C. Gross, E. Demler, S. Kuhr, and I. Bloch, *Nature* **487**, 454 (2012).
- [20] E. Altman, arXiv:1512.0870 [cond-mat.quant-gas].
- [21] A. Polkovnikov, K. Sengupta, A. Silva, and M. Vengalattore, *Rev. Mod. Phys.* **83**, 863 (2011).
- [22] J. Eisert, M. Friesdorf, and C. Gogolin, *Nat. Phys.* **11**, 124 (2015).
- [23] C. D. White, M. Zaletel, R. S. K. Mong, and G. Refael, *Phys. Rev. B* **97**, 035127 (2018).
- [24] S. Goto and I. Danshita, arXiv:1809.01400.
- [25] M. Greiner, O. Mandel, T. W. Hänsch, and I. Bloch, *Nature* **419**, 51 (2002).
- [26] E. Altman and A. Auerbach, *Phys. Rev. Lett.* **89**, 250404 (2002).
- [27] A. K. Tuchman, C. Orzel, A. Polkovnikov, and M. A. Kasevich, *Phys. Rev. A* **74**, 051601(R) (2006).
- [28] R. Schützhold, M. Uhlmann, Y. Xu, and U. R. Fischer, *Phys. Rev. Lett.* **97**, 200601 (2006).
- [29] C. Kollath, A. M. Läuchli, and E. Altman, *Phys. Rev. Lett.* **98**, 180601 (2007).
- [30] U. R. Fischer, R. Schützhold, and M. Uhlmann, *Phys. Rev. A* **77**, 043615 (2008).
- [31] J. Dziarmaga, M. Tylutki, and W. H. Zurek, *Phys. Rev. B* **86**, 144521 (2012).

- [32] F. Meinert, M. J. Mark, E. Kirilov, K. Lauber, P. Weinmann, A. J. Daley, H.-C. Nägerl, *Phys. Rev. Lett.* **111**, 053003 (2013).
- [33] S. Braun, M. Friesdorf, S. S. Hodgman, M. Schreiber, J. P. Ronzheimer, A. Riera, M. del Rey, I. Bloch, J. Eisert, and U. Schneider, *PNAS* **112**, 3641 (2015).
- [34] S. Braun, *Negative temperature and the dynamics of quantum phase transitions*, (Ph. D. Thesis, Ludwig-Maximilians-Universität München, 2014).
- [35] H. Asaka, Y. Takasu, and Y. Takahashi, 2016 Autumn Meeting, The Physical Society of Japan, 15aKJ-6 (2016).
- [36] Y. Takasu, T. Yagami, H. Asaka, Y. Fukushima, K. Nagao, S. Goto, and I. Danshita, Y. Takahashi, in preparation.
- [37] D. Podolsky, A. Auerbach, and D. P. Arovas, *Phys. Rev. B* **84**, 174522 (2011).
- [38] D. Podolsky and S. Sachdev, *Phys. Rev. B* **86**, 054508 (2012).
- [39] S. Gazit, D. Podolsky, A. Auerbach, *Phys. Rev. Lett.* **110**, 140401 (2013); *Phys. Rev. B* **88**, 235108 (2013).
- [40] A. Raçon and N. Dupuis, *Phys. Rev. B* **89**, 180501(R) (2014).
- [41] Y. T. Katan and D. Podolsky, *Phys. Rev. B* **91**, 075132 (2015).
- [42] F. Rose, F. Léonard, and N. Dupuis, *Phys. Rev. B* **91**, 224501 (2015).
- [43] L. Pollet and N. Prokof'ev, *Phys. Rev. Lett.* **109**, 010401 (2012).
- [44] L. Liu, K. Chen, Y. Deng, M. Endres, L. Pollet, and N. Prokof'ev, *Phys. Rev. B* **92**, 174521 (2015).
- [45] K. Chen, L. Liu, Y. Deng, L. Pollet, and N. Prokof'ev, *Phys. Rev. Lett.* **110**, 170403 (2013).
- [46] K. Nagao and I. Danshita, *Prog. Theor. Exp. Phys.* **2016**, 063I01 (2016).
- [47] D. Walls and G. Milburn, *Quantum Optics* (Springer-Verlag, Berlin, 1994).
- [48] P. B. Blakie, A. S. Bradley, M. J. Davis, R. J. Ballagh, and C. W. Gardiner, *Adv. Phys.* **57**, 363 (2008).
- [49] A. Polkovnikov, *Ann. Phys.* **325**, 1790 (2010).

- [50] A. Polkovnikov, S. Sachdev, and S. M. Girvin, *Phys. Rev. A* **66**, 053607 (2002).
- [51] A. Polkovnikov, *Phys. Rev. A* **68**, 033609 (2003).
- [52] J. Jünemann, A. Cadarso, D. Pérez-García, A. Bermudez, and J. J. García-Ripoll, *Phys. Rev. Lett.* **111**, 230404 (2013).
- [53] P. Hauke and L. Tagliacozzo, *Phys. Rev. Lett.* **111**, 207202 (2013).
- [54] J. Schachenmayer, B. P. Lanyon, C. F. Roos, and A. J. Daley, *Phys. Rev. X* **3**, 031015 (2013).
- [55] P. Richerme, Z.-X. Gong, A. Lee, C. Senko, J. Smith, M. Foss-Feig, S. Michalakis, A. V. Gorshkov, and C. Monroe, *Nature* **511**, 198 (2014).
- [56] P. Jurcevic, B. P. Lanyon, P. Hauke, C. Hempel, P. Zoller, R. Blatt, and C. F. Roos, *Nature* **511**, 202 (2014).
- [57] L. Bonnes, F. H. L. Essler, and A. M. Läuchli, *Phys. Rev. Lett.* **113**, 187203 (2014).
- [58] A. M. Läuchli and C. Kollath, *J. Stat. Mech.* P05018 (2008).
- [59] P. Barmettler, D. Poletti, M. Cheneau, and C. Kollath, *Phys. Rev. A* **85**, 053625 (2012).
- [60] E. H. Lieb and D. W. Robinson, *Commun. Math. Phys.* **28**, 251 (1972).
- [61] G. Carleo, F. Becca, L. Sanchez-Palencia, S. Sorella, and M. Fabrizio, *Phys. Rev. A* **89**, 031602(R) (2014).
- [62] K. V. Krutitsky, P. Navez, F. Queisser, and R. Schützhold, *EPJ Quantum Technol.* **1**, 1 (2014).
- [63] J. Schachenmayer, A. Pikovski, and A. M. Rey, *New. J. Phys.* **17**, 065009 (2015).
- [64] K. Nagao, Y. Takahashi, and I. Danshita, *Phys. Rev. A* **97**, 043628 (2018).
- [65] K. Nagao, M. Kunimi, Y. Takasu, Y. Takahashi, and I. Danshita, arXiv:1810.04347.
- [66] M. Greiner, *Ultracold quantum gases in three-dimensional optical lattice potentials*, Ph. D. thesis, Ludwig-Maximilians-Universität München (2003).
- [67] R. Grimm, M. Weidemüller, and Y. B. Ovchinnikov, *Adv. At., Mol., Opt. Phys.* **42**, 95 (2000).
- [68] C. J. Pethick and H. Smith, *Bose-Einstein Condensation in Dilute Gases* (Cambridge University Press, Cambridge, UK, 2008).

- [69] J. Sebby-Strabley, M. Anderlini, P. S. Jessen, and J. V. Porto, *Phys. Rev. A* **73**, 033605 (2006).
- [70] G. Wirth, M. Olschlager, and A. Hemmerich, *Nat. Phys.* **7**, 147 (2010).
- [71] P. Soltan-Panahi, J. Struck, P. Hauke, A. Bick, W. Plenkers, G. Meineke, C. Becker, P. Windpassinger, M. Lewenstein, and K. Sengstock, *Nat. Phys.* **7**, 434 (2011).
- [72] C. Becker, P. Soltan-Panahi, J. Kronjäger, S. Dörscher, K. Bongs, and K. Sengstock, *New Jour. Phys.* **12**, 065025 (2010).
- [73] J. Struck, C. Ölschläger, R. L. Targat, P. Soltan-Panahi, A. Eckardt, M. Lewenstein, P. Windpassinger, K. Sengstock, *Science* **333**, 996 (2011).
- [74] G.-B. Jo, J. Guzman, C. K. Thomas, P. Hosur, A. Vishwanath, and D. M. Stamper-Kurn, *Phys. Rev. Lett.* **108**, 045305 (2012).
- [75] S. Taie, H. Ozawa, T. Ichinose, T. Nishio, S. Nakajima, and Y. Takahashi, *Sci. Adv.* **1**, e1500854 (2015).
- [76] M. Ueda, *Fundamentals and New frontiers of Bose-Einstein Condensation* (World Scientific, 2010).
- [77] M. P. A. Fisher, P. B. Weichman, G. Grinstein, D. S. Fisher, *Phys. Rev. B* **40**, 546 (1989).
- [78] N. Teichmann, D. Hinrichs, M. Holthaus, and A. Eckardt, *Phys. Rev. B* **79**, 100503(R) (2009).
- [79] D. van Oosten, P. van der Straten, and H. T. C. Stoof, *Phys. Rev. A* **63**, 053601 (2001).
- [80] S. Sachdev, *Quantum Phase Transition* (Cambridge University Press, Cambridge, UK, 2011), 2nd ed.
- [81] B. Capogrosso-Sansone, N. V. Prokof'ev, and B. V. Svistunov, *Phys. Rev. B* **75**, 134302 (2007).
- [82] B. Capogrosso-Sansone, Ş. G. Söyler, N. Prokof'ev, and Boris Svistunov, *Phys. Rev. A* **77**, 015602 (2008).
- [83] N. D. Mermin and H. Wanger, *Phys. Rev. Lett.* **17**, 1133 (1966).
- [84] S. Coleman, *Commun. Math. Phys.* **31**, 259 (1973).

- [85] V. L. Berezinskii, Sov. Phys. JETP **32**, 493 (1970).
- [86] V. L. Berezinskii, Sov. Phys. JETP **34**, 601 (1971).
- [87] J. M. Kosterlitz and D. J. Thouless, J. Phys. C: Solid State Phys. **6**, 1181 (1973).
- [88] J. M. Kosterlitz and D. J. Thouless, J. Phys. C: Solid State Phys. **6**, 1046 (1974).
- [89] T. Giamarchi, *Quantum Physics in One Dimension*, (Oxford University Press, New York, 2003).
- [90] D. S. Rokhsar, B. G. Kotliar, Phys. Rev. B **44**, 10328 (1991)
- [91] W. Krauth, M. Caffarel, and J. Bouchaud, Phys. Rev B **45**, 3137 (1992).
- [92] S. D. Huber, E. Altman, H. P. Büchler, and G. Blatter, Phys. Rev. B **75**, 085106 (2007).
- [93] T. D. Kühner, S. R. White, H. Monien, Phys. Rev. B **61**, 12474 (2000).
- [94] T. Nakayama, I. Danshita, T. Nikuni, and S. Tsuchiya, Phys. Rev. A **92**, 043610 (2015).
- [95] D. Pekker and C. M. Varma, Annu. Rev. Condens. Matter Phys. **6**, 269 (2015).
- [96] G. E. Volovik and M. A. Zubkov, J. Low Temp. Phys. **175**, 486 (2014).
- [97] R. Sooryakumar and M. V. Klein, Phys. Rev. Lett. **45**, 660 (1980).
- [98] R. Sooryakumar and M. V. Klein, Phys. Rev. B **23**, 3213 (1981).
- [99] P. B. Littlewood and C. M. Varma, Phys. Rev. Lett. **47**, 811 (1981).
- [100] P. B. Littlewood and C. M. Varma, Phys. Rev. B **26**, 4883 (1982).
- [101] M.-A. Méasson, Y. Gallais, M. Cazayous, B. Clair, P. Rodière, L. Cario, and A. Sacuto, Phys. Rev. B **89**, 060503 (2014).
- [102] R. Matsunaga, Y. I. Hamada, K. Makise, Y. Uzawa, H. Terai, Z. Wang, and R. Shimano, Phys. Rev. Lett. **111**, 057002 (2013).
- [103] R. Matsunaga, N. Tsuji, H. Fujita, A. Sugioka, K. Makise, Y. Uzawa, H. Terai, Z. Wang, H. Aoki, and R. Shimano, Science **345**, 6201 (2014).
- [104] D. Sherman, U. S. Pracht, B. Gorshunov, S. Poran, J. Jesudasan, M. Chand, P. Raychaudhuri, M. Swanson, N. Trivedi, A. Auerbach, M. Scheffler, A. Frydman, and M. Dressel, Nat. Phys. **11**, 188 (2015).

- [105] R. Matsunaga, N. Tsuji, K. Makise, H. Terai, H. Aoki, and R. Shimano, arXiv:1703.02815 [cond-mat.supr-con].
- [106] Ch. Rüegg, B. Normand, M. Matsumoto, A. Furrer, D. F. McMorrow, K.W. Kramer, H. U. Gudel, S. N. Gvasaliya, H. Mutka, and M. Boehm, *Phys. Rev. Lett.* **100**, 205701 (2008).
- [107] P. Merchant, B. Normand, K. W. Krämer, M. Boehm, D. F. McMorrow, and Ch. Rüegg, *Nat. Phys.* **10**, 373 (2014).
- [108] H. Kuroe, N. Takami, N. Niwa, T. Sekine, M. Matsumoto, F. Yamada, H. Tanaka, and K. Takemura, *J. Phys.: Conf. Series* **400**, 032042 (2012).
- [109] J. Demsar, K. Biljaković, and D. Mihailovic, *Phys. Rev. Lett.* **83**, 800 (1999).
- [110] H. Schaefer, V. V. Kabanov, and J. Demsar, *Phys. Rev. B* **89**, 045106 (2014).
- [111] R. Yusupov, T. Mertelj, V. V. Kabanov, S. Brazovskii, P. Kusar, J.-H. Chu, I. R. Fisher, and D. Mihailovic, *Nat. Phys.* **6**, 681 (2010).
- [112] T. Mertelj, P. Kusar, V. V. Kabanov, P. Giraldo-Gallo, I. R. Fisher, and D. Mihailovic, *Phys. Rev. Lett.* **110**, 156401 (2013).
- [113] O. Avenel, E. Varoquaux, and H. Ebisawa, *Phys. Rev. Lett.* **45**, 1952 (1980).
- [114] C. A. Collett, J. Pollanen, J. I. A. Li, W. J. Gannon, and W. P. Halperin, *J. Low Temp. Phys.* **171**, 214 (2013).
- [115] A. Behrle, T. Harrison, J. Kombe, K. Gao, M. Link, J.-S. Bernier, C. Kollath, and M. Köhl, *Nat. Phys.* **14**, 781 (2018).
- [116] P. W. Higgs, *Phys. Rev. Lett.* **13**, 508 (1964).
- [117] A. Auerbach, *Interacting Electrons and Quantum Magnetism*, (Springer, New York, 1994).
- [118] A. Polkovnikov, *Phys. Rev. B* **72**, 161201(R) (2005).
- [119] S. M. Davidson and A. Polkovnikov, *Phys. Rev. Lett.* **114**, 045701 (2015).
- [120] T. Holstein and H. Primakoff, *Phys. Rev.* **58**, 1908 (1940).
- [121] L. Pitaevskii and S. Stringari, *Bose–Einstein Condensation* (Oxford University Press, New York, 2003).

- [122] E. P. Wigner, Phys. Rev. **40**, 749 (1932).
- [123] M. Hillery, R. F. O'Connell, M. O. Scully, and E. P. Wigner, Physics Reports **106**, 121 (1984).
- [124] C. W. Gardiner and P. Zoller, *Quantum noise: a handbook of Markovian and non-Markovian quantum stochastic methods with applications to quantum optics*, (Springer, 2004).
- [125] H. Weyl, Z. Phys. **46**, 1 (1927).
- [126] J. Moyal, Proc. Camb. Philos. Soc. **45**, 99 (1949).
- [127] R. J. Glauber, Phys. Rev. Lett. **10**, 84 (1963).
- [128] L. Isella and J. Ruostekoski, Phys. Rev. A **72**, 011601(R) (2005).
- [129] A. Polkovnikov, Phys. Rev. A **68**, 053604 (2003).
- [130] A. Polkovnikov, D.-W. Wang, Phys. Rev. Lett. **93**, 070401 (2004).
- [131] L. Mathey and A. Polkovnikov, Phys. Rev. A **80**, 041601(R) (2009).
- [132] L. Mathey and A. Polkovnikov, Phys. Rev. A **81**, 033605 (2010).
- [133] L. Mathey, K. J. Günter, J. Dalibard, and A. Polkovnikov, Phys. Rev. A **95**, 053630 (2017).
- [134] I. S. Landea and N. Nessi, Phys. Rev. A **91**, 063601 (2015).
- [135] K. Fujimoto, R. Hamazaki, and M. Ueda, Phys. Rev. Lett. **120**, 073002 (2018).
- [136] J. G. Cosme, Phys. Rev. A **97**, 043610 (2018).
- [137] M. Kunimi and I. Danshita, to appear.
- [138] J. Schachenmayer, A. Pikovski, and A. M. Rey, Phys. Rev. X **5**, 011022 (2015).
- [139] J. Wurtz, A. Polkovnikov, and D. Sels, Ann. Phys. **395**, 341 (2018).
- [140] A. M. Rey, A. V. Gorshkov, C. V. Kraus, M. J. Martin, M. Bishof, M. D. Swallows, X. Zhang, C. Benko, J. Ye, N. D. Lemke, and A. D. Ludlow, Ann. Phys. **340**, 311 (2014).
- [141] G. Kordas, D. Witthaut, and S. Wimberger, Ann. Phys. (Berlin) **527**, 619 (2015).
- [142] A. Johnson, S. S. Szigeti, M. Schemmer, and I. Bouchoule, Phys. Rev. A **96**, 013623 (2017).

- [143] F. Vicentini, F. Minganti, R. Rota, G. Orso, and C. Ciuti, *Phys. Rev. A* **97**, 013853 (2018).
- [144] J. G. Cosme, C. Georges, A. Hemmerich, and L. Mathey, *Phys. Rev. Lett.* **121**, 153001 (2018).
- [145] A. Altland, V. Gurarie, T. Kriecherbauer, and A. Polkovnikov, *Phys. Rev. A* **79**, 042703 (2009).
- [146] A. Piñeiro Orioli, A. Safavi-Naini, M. L. Wall, and A. M. Rey, *Phys. Rev. A* **96**, 033607 (2017).
- [147] D. Raventós, T. Graß, B. Juliá-Díaz, and M. Lewenstein, *Phys. Rev. A* **97**, 052310 (2018).
- [148] S. M. Davidson, D. Sels, and A. Polkovnikov, *Ann. Phys.* **384**, 128 (2017).
- [149] T. Scaffidi and E. Altman, arXiv:1711.04768.
- [150] M. Schmitt, D. Sels, S. Kehrein, and A. Polkovnikov, arXiv:1802.06796.
- [151] B. Berg, L. I. Plimak, A. Polkovnikov, M. K. Olsen, M. Fleischhauer, and W. P. Schleich, *Phys. Rev. A* **80**, 033624 (2009).
- [152] M. Endres, *Probing correlated quantum many-body systems at the single-particle level*, Ph. D. thesis, Ludwig-Maximilians-Universität München (2013).
- [153] P. O. Fedichev, Y. Kagan, G. V. Shlyapnikov, and J. T. M. Walraven, *Phys. Rev. Lett.* **77**, 2913 (1996).
- [154] M. Theis, G. Thalhammer, K. Winkler, M. Hellwig, G. Ruff, R. Grimm, and J. H. Denschlag, *Phys. Rev. Lett.* **93**, 123001 (2004).
- [155] R. Yamazaki, S. Taie, S. Sugawa, and Y. Takahashi, *Phys. Rev. Lett.* **105**, 050405 (2010).
- [156] D. M. Bauer, M. Lettner, C. Vo, G. Rempe, and S. Dürr, *Nat. Phys.* **5**, 339 (2009).
- [157] L. W. Clark, L.-C. Ha, C.-Y. Xu, and C. Chin, *Phys. Rev. Lett.* **115**, 155301 (2015).
- [158] A. L. Chernyshev and M. E. Zhitomirsky, *Phys. Rev. B* **79**, 144416 (2009).
- [159] T. Kita, *J. Phys. Soc. Jpn.* **75**, 044603 (2006).
- [160] V. I. Yukalov and H. Kleinert, *Phys. Rev. A* **73**, 063612 (2006).
- [161] A. Griffin, *Phys. Rev. B* **53**, 9341 (1996).

- [162] N. Shohno, *Prog. Theor. Phys.* **31**, 553 (1964).
- [163] A. A. Abrikosov, L. P. Gorkov, and I. E. Dzyaloshinski, *Methods of Quantum Field Theory in Statistical Physics* (Dover Publications, New York, 1975).
- [164] E. M. Lifshitz and L. Pitaevskii, *Statistical Physics, Part 2* (Pergamon, Oxford, UK, 1980).
- [165] A. Altland and B. D. Simons, *Condensed Matter Field Theory* (Cambridge University Press, Cambridge, UK, 2010), 2nd ed.
- [166] N. Dupuis, *Phys. Rev. E* **83**, 031120 (2011).
- [167] I. Affleck and G. F. Wellman, *Phys. Rev. B* **46**, 8934 (1992).
- [168] Y. Takasu, Y. Nakamura, J. Kobayashi, H. Asaka, Y. Fukushima, Y. Takahashi, K. Inaba, and M. Yamashita, arXiv:1808.04599.
- [169] C. W. Gardiner, J. R. Anglin, and T. I. A. Fudge, *J. Phys. B: At. Mol. Opt. Phys.* **35**, 1555 (2002).
- [170] M. K. Olsen, A. S. Bradley, and S. B. Cavalcanti, *Phys. Rev. A* **70**, 033611 (2004).
- [171] E. Altman, E. Demler, and M. D. Lukin, *Phys. Rev. A* **70**, 013603 (2004).
- [172] S. Fölling, F. Gerbier, A. Widera, O. Mandel, T. Gericke, and I. Bloch, *Nature* **434**, 481 (2005).
- [173] I. Danshita and P. Naidon, *Phys. Rev. A* **79**, 043601 (2009).
- [174] E. F. Krause, *Taxicab Geometry* (Courier Dover Publications, New York, 1986).
- [175] L. P. Kadanoff and G. Baym, *Quantum Statistical Mechanics* (Benjamin, New York, 1962).
- [176] Y. Q. Qin, B. Normand, A. W. Sandvik, and Z. Y. Meng, *Phys. Rev. Lett.* **118**, 147207 (2017).
- [177] A. Rançon and N. Dupuis, *Phys. Rev. B* **83**, 172501 (2011).
- [178] A. Rançon and N. Dupuis, *Phys. Rev. B* **84**, 174513 (2011).
- [179] K. Nagao, Y. Takasu, Y. Takahashi, and I. Danshita, in preparation.
- [180] K. Nagao and A. Polkovnikov, in preparation.